RAPID CLIMATE CHANGES IN THE ARCTIC REGION OF SVALBARD: PROCESSES, IMPLICATIONS AND REPRESENTATIVENESS FOR THE BROADER ARCTIC

Dissertation Thesis with the aim of achieving the academic degree "doctor rerum naturalium" (Dr. rer. nat.)

in the science discipline "Climate Physics"

submitted to the Faculty of Science and Institute of Physics and Astronomy at Potsdam University

conducted at the Alfred Wegener Institute, Helmholtz Centre for Polar and Marine Research, Potsdam

by

SANDRO DAHLKE

defended in Potsdam on February 21, 2020

Supervisors:
Prof. Dr. Klaus Dethloff
Dr. Marion Maturilli

Reviewers:
Prof. Dr. Klaus Dethloff
Prof. Dr. Manfred Wendisch
Dr. habil. Tymon Zieliński

Published online at the
Institutional Repository of the University of Potsdam:
https://doi.org/10.25932/publishup-44554
https://nbn-resolving.org/urn:nbn:de:kobv:517-opus4-445542

Cover photography by S. Dahlke: Kronebreen Glacier from Kongsfjorden, 24.05.2017, 9:36 am.

Thesis typesetting using the classicthesis template developed by André Miede, available at: https://bitbucket.org/amiede/classicthesis/

ABSTRACT

Over the last decades, the Arctic regions of the earth have warmed at a rate 2–3 times faster than the global average– a phenomenon called *Arctic Amplification*. A complex, non-linear interplay of physical processes and unique pecularities in the Arctic climate system is responsible for this, but the relative role of individual processes remains to be debated. This thesis focuses on the climate change and related processes on Svalbard, an archipelago in the North Atlantic sector of the Arctic, which is shown to be a "hotspot" for the amplified recent warming during winter. In this highly dynamical region, both oceanic and atmospheric large-scale transports of heat and moisture interfere with spatially inhomogenous surface conditions, and the corresponding energy exchange strongly shapes the atmospheric boundary layer. In the first part, Pan-Svalbard gradients in the surface air temperature (SAT) and sea ice extent (SIE) in the fjords are quantified and characterized. This analysis is based on observational data from meteorological stations, operational sea ice charts, and hydrographic observations from the adjacent ocean, which cover the 1980–2016 period. It is revealed that typical estimates of SIE during late winter range from 40–50% (80–90%) in the western (eastern) parts of Svalbard. However, strong SAT warming during winter of the order of 2–3 K per decade dictates excessive ice loss, leaving fjords in the western parts essentially ice-free in recent winters. It is further demostrated that warm water currents on the west coast of Svalbard, as well as meridional winds contribute to regional differences in the SIE evolution. In particular, the proximity to warm water masses of the West Spitsbergen Current can explain 20–37% of SIE variability in fjords on west Svalbard, while meridional winds and associated ice drift may regionally explain 20–50% of SIE variability in the north and northeast. Strong SAT warming has overruled these impacts in recent years, though.
In the next part of the analysis, the contribution of large-scale atmospheric circulation changes to the Svalbard temperature development over the last 20 years is investigated. A study employing kinematic air-back trajectories for Ny-Ålesund reveals a shift in the source regions of lower-troposheric air over time for both the winter and the summer season. In winter, air in the recent decade is more often of lower-latitude Atlantic origin, and less frequent of Arctic origin. This affects heat- and moisture advection towards Svalbard, potentially manipulating clouds and longwave downward radiation in that region. A closer investigation indicates that this shift during winter is associated with a strengthened Ural blocking high and Icelandic low, and contributes about 25% to the observed winter warming on

Svalbard over the last 20 years. Conversely, circulation changes during summer include a strengthened Greenland blocking high which leads to more frequent cold air advection from the central Arctic towards Svalbard, and less frequent air mass origins in the lower latitudes of the North Atlantic. Hence, circulation changes during winter are shown to have an amplifying effect on the recent warming on Svalbard, while summer circulation changes tend to mask warming.
An observational case study using upper air soundings from the AWIPEV research station in Ny-Ålesund during May–June 2017 underlines that such circulation changes during summer are associated with tropospheric anomalies in temperature, humidity and boundary layer height.
In the last part of the analysis, the regional representativeness of the above described changes around Svalbard for the broader Arctic is investigated. Therefore, the terms in the diagnostic temperature equation in the Arctic-wide lower troposphere are examined for the Era-Interim atmospheric reanalysis product. Significant positive trends in diabatic heating rates, consistent with latent heat transfer to the atmosphere over regions of increasing ice melt, are found for all seasons over the Barents/Kara Seas, and in individual months in the vicinity of Svalbard. The above introduced warm (cold) advection trends during winter (summer) on Svalbard are successfully reproduced. Regarding winter, they are regionally confined to the Barents Sea and Fram Strait, between 70°–80°N, resembling a unique feature in the whole Arctic. Summer cold advection trends are confined to the area between eastern Greenland and Franz Josef Land, enclosing Svalbard.

KURZFASSUNG

Die Arktis hast sich über die letzten Jahrzehnte etwa 2–3 mal so schnell erwärmt wie die globale Mitteltemperatur der Erde, wofür der Begriff *Arktische Verstärkung* geprägt wurde. Eine komplexe Kaskade nichtlinear miteinander interagierender Prozesse und lokaler Bedingungen ist für das Auftreten dieses Phänomens verantwortlich, jedoch bleibt ein wissenschaftlicher Konsens zur Quantifizierung einzelner beteiligter Prozesse noch aus. Diese Arbeit befasst sich mit den Klimaänderungen und assoziierten Prozessen in der Svalbard-Region, einem arktischen Archipel im Nordatlantik. Svalbard kann als Brennpunkt der arktischen Veränderungen bezeichnet werden, vor allem während des Winters. In dieser ausgesprochen dynamischen Region interagieren die Energieflüsse durch großskalige atmosphärische und ozeanische Wärme- und Feuchtetransporte mit der heteorogenen Oberfläche, die sich aus Eis-, Wasser-, oder Landflächen zusammensetzt. Die daraus

resultierenden horizontalen und vertikalen Energieflüsse stehen in engem Zusammenhang mit der Beschaffenheit der atmosphärischen Grenzschicht.
Im ersten Teil dieser Arbeit werden laterale Unterschiede in der Oberflächentemperatur (SAT), sowie der Meereisbedeckung (SIE) in den Fjorden und Sunden des Archipels quantifiziert und klassifiziert. Dies geschieht auf der Grundlage von meteorologischen Stationsmessdaten und operationellen Eisbedeckungskarten der Jahe 1980–2016. Es zeigt sich, dass prozentuale Eisbedeckungen im Osten des Studiengebietes typischerweise 80–90% im Winter erreichen, während diese Werte in Fjorden der Westküste mit 40–50% deutlich niedriger liegen. Allerdings bedingt eine starke, winterliche SAT Erwärmung von 2–3 K pro Jahrzehnt signifikante SIE Abwärtstrends, sodass die Fjorde im Westen von Svalbard in den jüngeren Wintern üblicherweise eisfrei waren. Im Weiteren wird gezeigt dass die warmen Ozeanströmungen nahe der Westküste, sowie spezielle Windkonstellationen, einen signifikanten regionalen Einfluss auf die langzeitliche Entwicklung der Meereisbedeckung ausüben. So kann Variabilität in der Temperatur des Westspitzbergenstroms etwa 20–37% der zwischenjährlichen SIE Variabilität in den Fjorden der Westküste erklären. Die meridionale Atmosphärenströmung nordwestlich von Spitzbergen, die hochkorelliert mit Eisdrift ist, kann andererseits –regional abhängig– etwa 20–50% der SIE-Variablität in den nördlichen und nordöstlichen Fjorden erklären. Durch den starken temperaturbedingten Eisrückgang in der gesamten Region sind diese Einflüsse zuletzt jedoch stark abgeschwächt.
Im Folgenden wird der Beitrag von Zirkulationsänderungen zur Temperaturentwicklung Svalbards während der letzten 20 Jahre untersucht. Die Analyse basiert auf den Quellregionen troposphärischer Luftmassen, die sich aus kinematischen FLEXTRA-Rückwärtstrajektorien ergeben. Für den Winter zeigt sich, dass sich diese zuletzt immer häufiger in sub-arktische Gebiete über dem Nordatlantik verlagert hatten, und seltener in der hohen Arktis lagen. Dies moduliert Warmluft-, und Feuchtetransporte in Richtung Spitzbergen, und beeinflusst potentiell Wolkencharakteristiken und assoziierte Strahlungsprozesse. Nähere Untersuchen zeigen dass ein zuletzt stärker ausgeprägtes Uralhoch und Islandtief dafür verantwortlich sind, und dass dies einen Beitrag von etwa 25% zur jüngsten Wintererwärmung auf Spitzbergen hat. Sommertrajektorien offenbaren eine gegensätzliche Entwicklung, mit häufigerer Anströmung aus der Zentralarktis, welche mit Kaltluftadvektion einhergeht, auf Kosten von seltenerer Anströmung aus dem Süden. Dies liegt in einem während der letzten 10 Jahre stark ausgeprägten Grönlandhoch begründet. Eine Fallstudie anhand von Radiosondendaten vom Frühsommer 2017 untermauert die Ergebnisse und zeigt darüber hinaus, dass derartige Zirkulationsänderungen mit ausgeprägten Anomalien von troposphärischen Temperaturen,

Feuchtigkeit, und der Grenzschichthöhe in Ny-Ålesund einher geht. Interessanterweise tragen Zirkulationsänderungen im Winter also verstärkend zur Erwärmung auf Svalbard bei, während jene im Sommer einer stärkeren Erwärmung entgegenwirken.
In einem letzten Analyseschritt wird die regionale Repräsentativität der Region für die weitere Arktis erörtert. Die Analyse von Era-Interim Reanalysedaten untermauert hierbei zunächst die advektiven Temperaturänderungen in Sommer und Winter in der Region um Svalbard. Der Trend zu verstärkt positiver winterlicher Temperaturadvektion ist einzigartig in der Arktis und beschränkt sich auf die Regionen zwischen Barentssee, Spitzbergen und der nördlichen Framstraße. Die sommerliche erhöhte Kaltluftadvektion findet sich in einem weiten Gebiet zwischen der Ostküste Grönlands und Franz-Josef-Land, welches Svalbard einschließt. Ein diabatischer Erwärmungstrend, der mit aufwärts gerichteten latenten Energieflüssen und Eisrückgang konsistent ist, findet sich in allen Jahreszeiten über der Barents/Karasee wieder, und erstreckt sich in einzelnen Monaten bis nach Svalbard.

PUBLICATIONS ASSOCIATED WITH THIS DISSERTATION

Knudsen, E. M., B. Heinold, **S. Dahlke**, H. Bozem, S. Crewell, I. V. Gorodetskaya, G. Heygster, D. Kunkel, M. Maturilli, M. Mech, C. Viceto, A. Rinke, H. Schmithüsen, A. Ehrlich, A. Macke, C. Lüpkes, and M. Wendisch (2018). "Meteorological conditions during the ACLOUD/PASCAL field campaign near Svalbard in early summer 2017." In: *Atmospheric Chemistry and Physics* 18.24, pp. 17995–18022. DOI: 10.5194/acp-18-17995-2018.

Dahlke, S. and M. Maturilli (2017). "Contribution of Atmospheric Advection to the Amplified Winter Warming in the Arctic North Atlantic Region." In: *Advances in Meteorology* 2017, Article ID 4928620, 8 pages. DOI: 10.1155/2017/4928620.

CONTENTS

LIST OF FIGURES

LIST OF TABLES

ACRONYMS

AA	Arctic Amplification
ATL	the region bounded by 50°N–71°N, 45°W–20°E
ATR	Annual Temperature Range
CA	the area north of 85°N
DJF	December-January–February mean
EOF	Empirical Orthogonal Function, see von Storch and Zwiers (2001)
IWV	Integrated Water Vapor Content
JJA	June–July–August mean
MAM	March–April–May mean
PBL	Planetary boundary layer
SAT	Surface Air Temperature
SAR	Synthetic Aperture Radar
SIE	Sea Ice Extent
SLP	Sea level pressure
SON	September–October–November mean
SST	Sea Surface Temperature
TOA	Top of Atmosphere
WSC	West Spitsbegen Current

1 INTRODUCTION

1.1 CONTEXT: A RAPIDLY CHANGING ARCTIC

1.1.1 *Documentation of recent changes in the Arctic*

One of the most striking observations regarding the climate of the world during the last century and particularly during the last decades, is the emergence of global warming. However, global warming is not evenly distributed over the globe. Surface air temperature (SAT) warming in the Arctic is progressing particularly fast and exceeds the global mean warming over the last 3–4 decades by a factor of 2–3. This phenomenon is referred to as Arctic Amplification (AA, e. g. Serreze et al., 2009; Serreze and Barry, 2011; Jaiser et al., 2016; Wendisch et al., 2017; Dethloff et al., 2019), and is also highlighted by the 5th IPCC assessment report on Climate Change (Kirtman et al., 2013). The severity of Arctic (i.e. north of 60°N) warming compared to the rest of the world is illustrated in Figure 1.1, where the annual mean, zonal mean SAT anomaly with respect to the reference period 1951–1980 is plotted. Since the early 2000s, AA becomes strikingly evident by warm anomalies between +2 to +4 K in the area north of 60°N, while the rest of the globe has warmed at a more moderate rate.

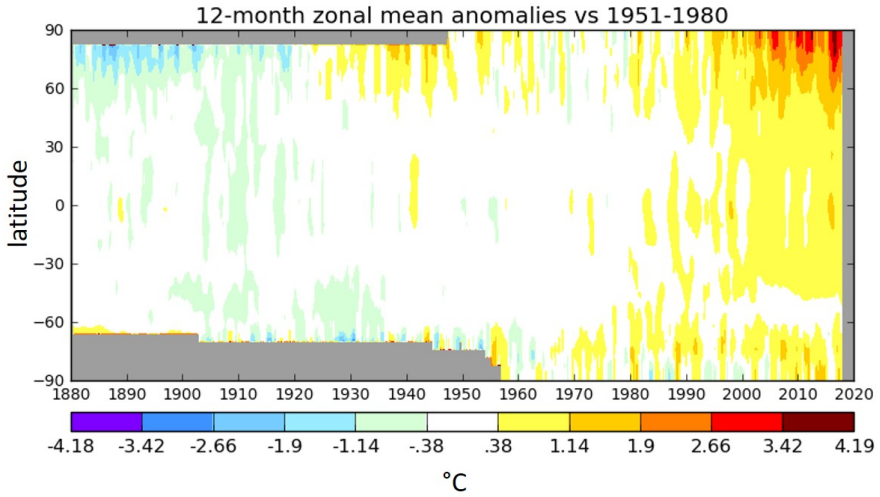

Figure 1.1: Progression of zonal mean, annual mean surface air temperature anomalies with respect to the 1951–1980 average, as from the Land-Ocean-Temperature index (LOTI)+ ERSSTv5. Data and picture are provided by the NASA Goddard Institute for Space Studies, and are available at `https://data.giss.nasa.gov/gistemp/`.

The drastic changes in SAT are accompanied by Arctic sea ice retreat in terms of areal extent, thickness and ice age (Stroeve et al., 2007; Stroeve et al., 2012b; Kwok, 2018; Onarheim et al., 2018). Kwok (2018) found that the Arctic has lost about 50% of its multiyear ice over the 1999–2017 period, and Onarheim et al. (2018) estimated that the Arctic shelf seas would become seasonally ice-free by the 2020s.

Drawing a comprehensive picture of the changing Arctic remains challenging, as a cascade of different processes is involved in driving the changes, and these exhibit a distinct seasonality and regionality. As an example, Arctic warming is most strongly expressed at the surface (Serreze et al., 2009) and in the winter season. In particular, Bintanja and Van der Linden (2013) conclude that Arctic winter warming exceeds the warming during summer by a factor of 4. Figures 1.2 and 1.3 show the decadal trends of the 2-meter air temperature and sea ice concentration for the 1979–2016 period. They serve as illustrations for the seasonality of the recent evolutions in these parameters across the Arctic. In all seasons, significant warming signals appear in the Arctic, and the above mentioned seasonal asymmetry is also evident. The dominant feature during spring and autumn is a warming of 1–2 K/decade that spans the Arctic ocean in the eastern hemisphere. Warming signals are weakest in summer (<1 K/decade), while in winter, significant warming is evident in the central Arctic and particularly in the North Atlantic sector, where it exceeds 3 K/decade in the northern Barents/Kara Seas, between Svalbard and Novaya Zemlya. It should be noted though that while Arctic warming is most strongly expressed at the surface, significant warming also affects the entire troposphere. For instance, warming signals are evident at the 500 hPa level in the mid-troposphere, and the corresponding maps are presented in Figure B.1 in the Appendix Section.

Atmospheric warming is paralleled by marked reductions in the sea ice concentration along the edge of the Arctic ocean (Figure 1.3). Winter and spring are characterized by maximum sea ice extents in the central Arctic, and downward trends then appear solely in the North Atlantic sector around the position of the climatological sea ice edge, which translates to a northward shift of the latter. Conversely, summer and autumn are the seasons of melting and represent the time of minimum sea ice extent, as indicated by the northward displaced sea ice edge. In summer and autumn, strong sea ice reductions have occurred in the shelf seas along the entire rim of the Arctic basin, including the Barents/Kara Seas, Laptev Sea, East Siberian Sea and Chukchi Sea. Maximum regional losses exceed 15 % per decade in all seasons in the affected areas. These regional and seasonal aspects are in good agreement with Onarheim et al. (2018).

It should be noted that AA is also associated with changes in the atmospheric large-scale circulation, which will be discussed in more

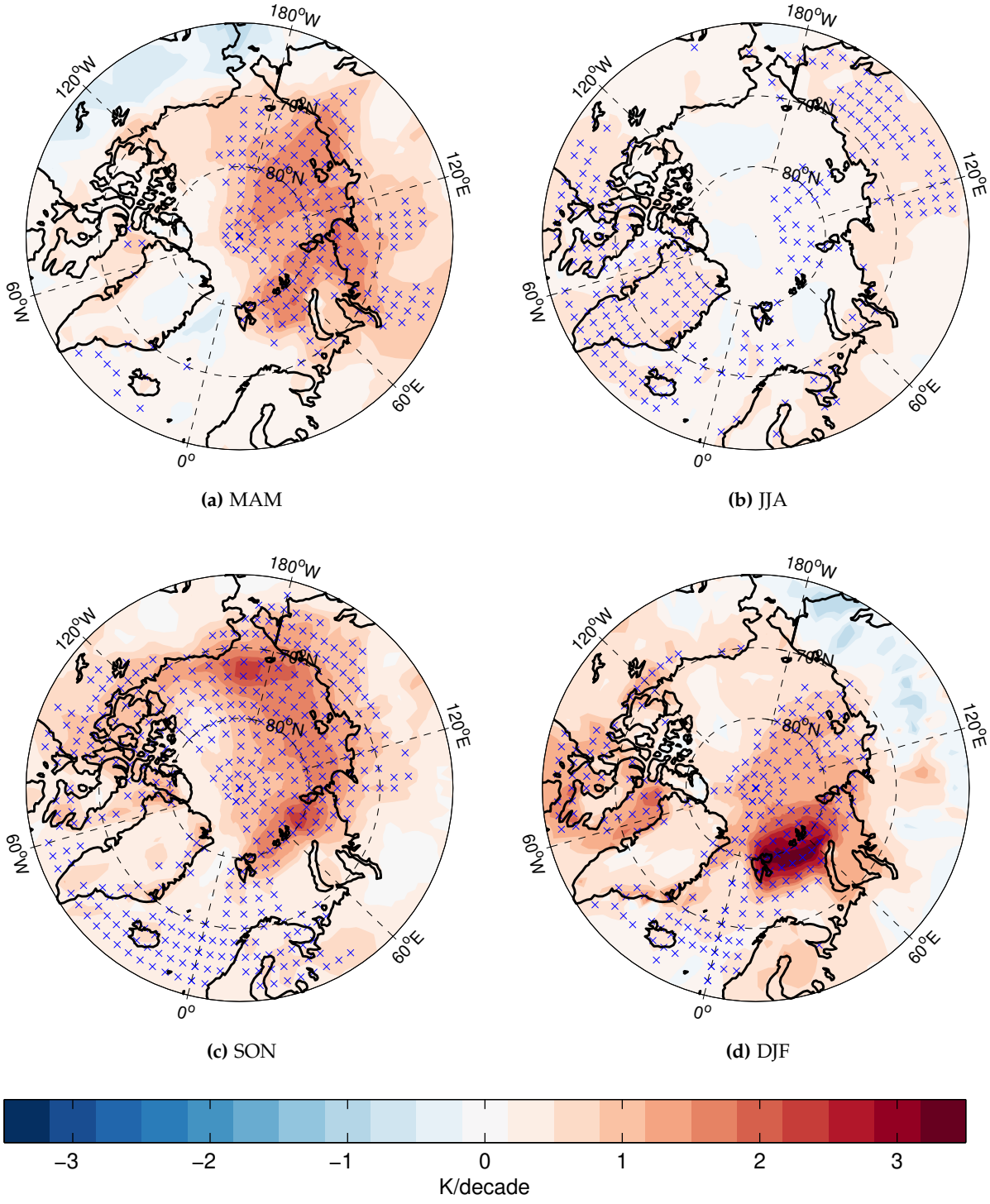

(a) MAM **(b)** JJA

(c) SON **(d)** DJF

Figure 1.2: 1979–2016 Decadal trends in the Era-Interim 2 meter temperature, for: **(a)**: spring (March–April–May, MAM), **(b:)**: summer (June–July–August, JJA), **(c)**: autumn (September–October–November, SON), **(d)**: winter (December, January, February, DJF). Crossed areas indicate trends significantly (α<0.01) different from zero.

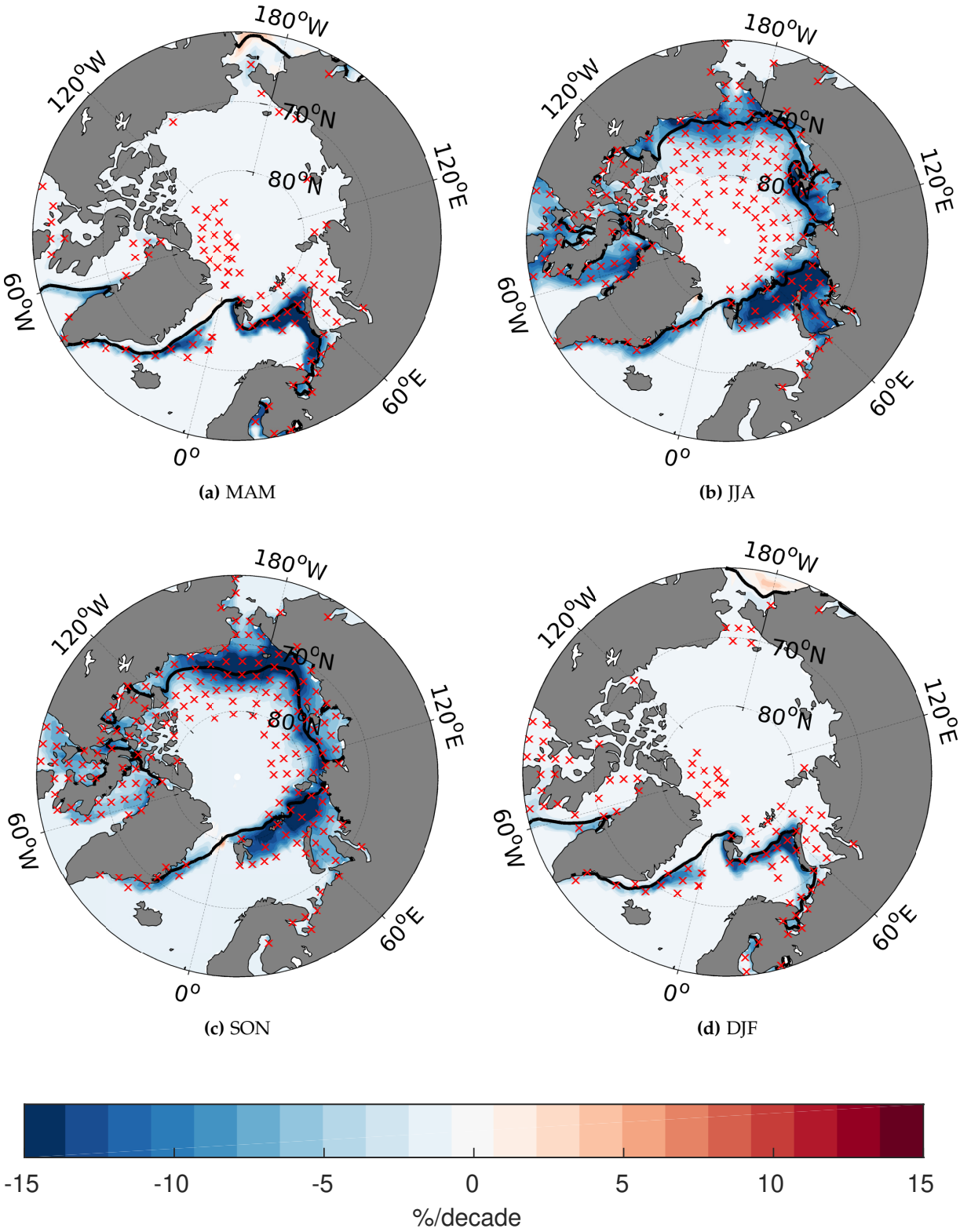

(a) MAM

(b) JJA

(c) SON

(d) DJF

Figure 1.3: 1979–2016 Decadal trends in the HadISST seasonal mean sea ice concentration, : **(a)**: spring (MAM), **(b:)**: summer (JJA), **(c)**: autumn (SON), **(d)**: winter (DJF). Crossed areas indicate trends significantly (α<0.01) different from zero. Black line indicates the seasonal mean position of the sea ice edge.

detail later in this study.

A broad range of literature has emerged about mechanisms and feedbacks potentially contributing to AA, however an exact quantification of the involved contributions remains difficult. The most widely discussed feedbacks include changes in sea ice cover via its effect on albedo and insulation effects (Serreze et al., 2009; Screen and Simmonds, 2010; Serreze and Barry, 2011; Burt et al., 2016; Taylor et al., 2018; Kim et al., 2019), the radiative effects of moist intrusions from lower latitudes into the Arctic (Woods et al., 2013; Woods and Caballero, 2016), as well as oceanic (Chylek et al., 2009) and atmospheric energy transport (Yang et al., 2010; Mewes and Jacobi, 2019). On the other hand, a number of studies have identified the important role of local effects in the Arctic lower atmosphere, such as the lapse rate feedback as the main driving force for AA (Bintanja et al., 2011; Pithan and Mauritsen, 2014; Stuecker et al., 2018; Taylor, 2018). Given their power in manipulating the surface radiative budget, Arctic clouds presumably play a central role in AA (Curry et al., 1996; Shupe and Intrieri, 2004; Verlinde et al., 2007; Wendisch et al., 2017; Wendisch et al., 2018).

Enhanced research activities targeting these poorly understood, interconnected processes are vital for an increased understanding, such as the efforts that are undertaken within the German "ArctiC Amplification: Climate Relevant Atmospheric and SurfaCe Processes, and Feedback Mechanisms $(AC)^3$" project. The above described regional changes in the Arctic provide the baseline of this thesis, which I have conducted within the $(AC)^3$ project. By capitalizing on observational data from the North Atlantic sector of the Arctic, it contributes to climatological characterisations of the Svalbard region and processes that drive the ongoing changes there.

1.1.2 *Research relevance*

Changes in the components of Arctic climate are discussed from politically to scientifically steered platforms, together with their association to increasing manmade greenhouse gas emissions. Detailed assessments of climate change and its implications are given by regularly updated assessment reports of the Intergovernmental Panel on Climate Change (IPCC). The Arctic is a key region for the understanding of the global changes, since Arctic warming significantly contributes to the globally averaged warming (Huang et al., 2017). Hence, a strong research interest regarding AA and the involved processes has developed given its profound impacts on the climate, ecosystems, economy and society. To provide some examples, discussions have emerged regarding the immediate link of Arctic warming and anomalous weather conditions in mid-latitudes (Francis and Vavrus, 2012; Cohen et al., 2014; Handorf et al., 2015; Overland et al., 2016; Shepherd, 2016). In

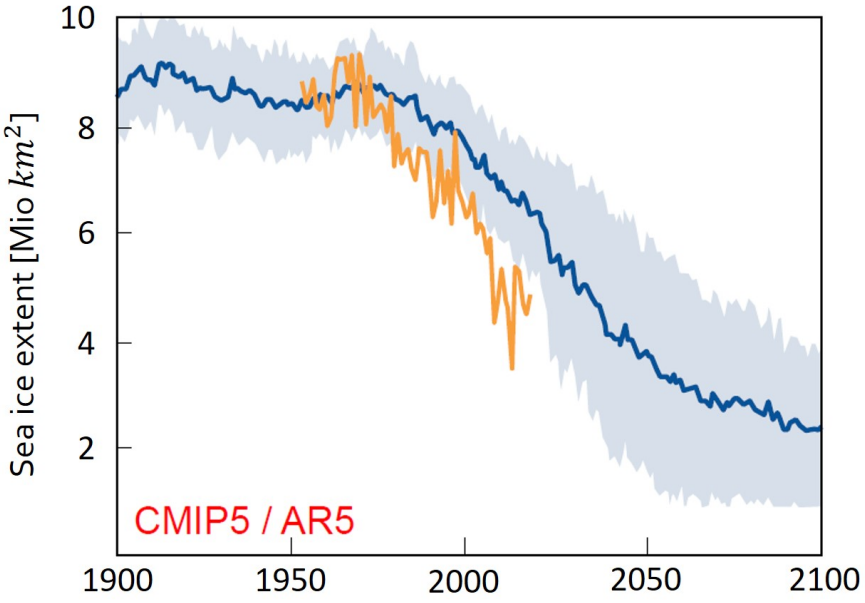

Figure 1.4: Comparison of CMIP5 multi model ensemble mean of Arctic september sea ice cover as modelled under the RCP4.5 emission scenario (blue line) with ± 1 standard deviation (light blue shading) and observed sea ice cover (red line). Figure is updated from Stroeve et al., 2012a

the near future perspective, prediction skill for Arctic sea ice development is desired, as it opens the door for Arctic tourism, new shipping routes, resource exploration and related aspects. However, state of the art coupled climate models have shortcomings in the Arctic, and tend to underestimate the observed recent Arctic sea ice retreat (Stroeve et al., 2012a; Stroeve et al., 2007) and the winter warming at the surface (Bintanja and Van der Linden, 2013). The lack of performance of state of the art coupled climate models in simulating observed sea ice variability is illustrated in Figure 1.4, where modelled Arctic sea ice cover is compared to the observed one. It is obvious that the observed ice losses outclass the modelled estimates, which raises concerns about the future projections towards the end of the century. Atmospheric reanalysis products are also shown to performe comparably poor in the Arctic, since they rely on a mixture of outputs from numerical model simulations and assimilated observations, but the latter are scarcely provided over the Arctic which limits assimilation capability (Lindsay et al., 2014; Graham et al., 2019).

AA is also a key element for far future assessments of the climate. There is evidence that, due to the non-linear, chaotic character of the climate, critical temperature thresholds may exist that could, if crossed, push the earth system into a runaway feedback loop that may lead it to a stabilized state that is very different from the current climate conditions, with unforeseeable consequences for humanity (Schellnhu-

ber et al., 2016; Steffen et al., 2018). Hence, progress in monitoring, modeling, understanding and synthesizing individual pieces of physical contributions to AA is currently an important objective in climate sciences.

1.1.3 *Objective: Svalbard as a hotspot for climate change*

Faegri's law (Faegri, 1950) states that the duration of periods of climate change is proportional to the area that becomes affected by the changes. This implies that for climate changes over thousands of years, the entire earth may be affected, while for climate changes over some decades - consistent with those described above - more regional impacts are expected. In fact, Figures 1.2 and 1.3 promote the view that the changes regarding near surface temperature and sea ice in the Arctic have a strong regional expression. My study is dedicated to the North Atlantic sector of the Arctic, and more precisely to meteorological, cryospheric and oceanographic observations from the Svalbard archipelago. Figures 1.2 and 1.3 provide evidence that Svalbard is a "hotspot" of both winter warming and year-round sea ice decreases in the high Arctic. Moreover, the climatological sea ice edge passes through the Svalbard region, introducing sharp north–south and east–west gradients in the atmospheric background conditions around the archipelago. In that context, already the third assessment report of the IPCC has suggested that the Svalbard region is particularly sensitive to changes in the atmospheric circulation (Houghton et al., 2001). For a landmass in those high Arctic latitudes, Svalbard is comparably easy to access and there exists a substantial variety of observed climate data (see Chapter 2), such that it may be viewed as a natural observatory of the ongoing changes. My thesis contributes to the investigations of the changing climate in the Svalbard region, with the specific aim in addressing the following research questions (RQ's):

RQ1 How can Pan-Svalbard differences in the surface meteorology and sea ice development be quantified and classified, and what are the responsible oceanic and atmospheric processes in driving those regional differences?

RQ2 Svalbard is located in the transition zone between cold polar air and warm airmasses from lower latitudes, impacted by both depending on the atmospheric circulation. To what degree are large scale circulation changes contributing to the observed warming over the last decades?

RQ3 On the background of the observational super-site Ny-Ålesund located on Svalbard's west coast, how representative are the recent changes in the Svalbard region with regard to the broader Arctic and regional differences in Arctic warming trends?

The setup of the thesis is as follows. In the next Chapter, fundamental physical concepts about radiation and circulation in the atmosphere, as well as unique features of the Arctic climate system will be introduced. A geographical, meteorologigal, cryospheric and oceanographic characterisation of the Svalbard archipelago follows up on that. Utilized data sets and statistical methods are introduced in Chapter 2. In Chapter 3 an analysis of regional climate parameters with focus on climatologies, trends and drivers of variability is conducted. In Chapter 4, a more large-scale perspective is applied by analysing air transport pathways and circulation changes in the free troposphere while discussing their ability to drive temperature anomalies in the Svalbard region. An assessment of the changing physical contributors to the near surface temperature budget of the Arctic follows in Chapter 5. The thesis closes with a summary and outlook in Chapter 6.

1.2 PHYSICAL BACKGROUND

The climate system of the earth is determined by a complex interplay of processes, ranging from the solid earth over the oceans, atmosphere and cryosphere. Of particular interest for my studies is the atmosphere, which is the gaseous fluid layer surrounding the planet. Motions in the atmosphere are associated with transport of energy and momentum, as well as the redistribution of chemical or physical constituents and tracers. To understand the drivers of motions in the atmosphere and of the changing Arctic energy budget, some preliminaries regarding the earth's radiation budget must be considered.

1.2.1 *Radiation and surface energy balance*

1.2.1.1 *Thermal radiation: foundations*

According to the Stefan–Boltzmann law, each body whose temperature is above total zero, emits thermal radiation in proportion to its temperature:

$$\Phi = \sigma \epsilon T^4 \tag{1.1}$$

where

Φ	emitted energy [Wm^{-2}]
σ	Stefan–Boltzmann constant: $5.67051 \cdot 10^{-8} [Wm^{-2}K^{-4}]$
ϵ	emissivity: $0 \leq \epsilon \leq 1$
T	surface temperature [K]

Planck's law further describes how the energy is then emitted over a spectrum of wavelengths that is also dependent on the temperature of the body:

$$B(\lambda, T) = \frac{2hc^2}{\lambda^5} \frac{1}{exp\left(\frac{hc}{k_B \lambda T}\right) - 1} \tag{1.2}$$

where

B	emitted energy $[Wm^{-3}sr^{-1}]$
h	Planck constant: $6.62607015 \cdot 10^{-34}$ [Js]
c	speed of light: $299792458\,ms^{-1}$
k_B	Boltzmann constant $1.38064852 \cdot 10^{-23}[JK^{-1}]$

Derivative of equation (1.2) by λ yields the wavelength λ_{max}, at which maximum radiation is emitted, and this relation is called Wien's displacement law:

$$\lambda_{max} = \frac{2897.8\,[\mu mK]}{T} \tag{1.3}$$

Combining equations (1.1) and (1.3), it becomes obvious that the higher the temperature of a body, the more energy can be emitted by it, and the more does its emission spectrum shift to the shorter wavelengths. As an example, the earth, assuming an average temperature of 288 K, emits at $390\,Wm^{-2}$ and the maximum emission occurs at $\lambda_{max} \approx 10\,\mu m$, which is in the infrared range of the spectrum. The sun, on the other hand, at an average temperature of 5778 K, emits $63\,MWm^{-2}$ at $\lambda_{max} \approx 0.5\,\mu m$, which is in the range of visible light. It is important to note that the entire solar emission spectrum decribed by (1.2) also covers parts of the ultraviolet (UV) wavelength range, down to $0.25\,\mu m$. In climate sciences, solar radiation is hence considered as "shortwave radiation", while terrestrial radiation is regarded as "longwave". This separation is of major importance, because scattering, absoption, emission and transmission of radiation by any kind of constituents in the atmosphere is dependent on the wavelength.

1.2.1.2 *Radiative key processes in the atmosphere*

The availability of molecules, particles and water droplets in the atmosphere complicates radiative processes, as they interact with both solar and terrestrial radiation. While a body can emit energy according to equation (1.1) itself, there are three kinds of possible interactions with incident radiation (see Figure 1.5). Part of the incident radiation can be reflected in backward direction, without the exchange of energy between the body and the radiation. If a body is not entirely opaque, but at least partially optically transparent, it will transmit a part of the radiation, thereby keeping the direction of the radiation. Finally, absorption of electromagnetic radiation refers to the conversion of the

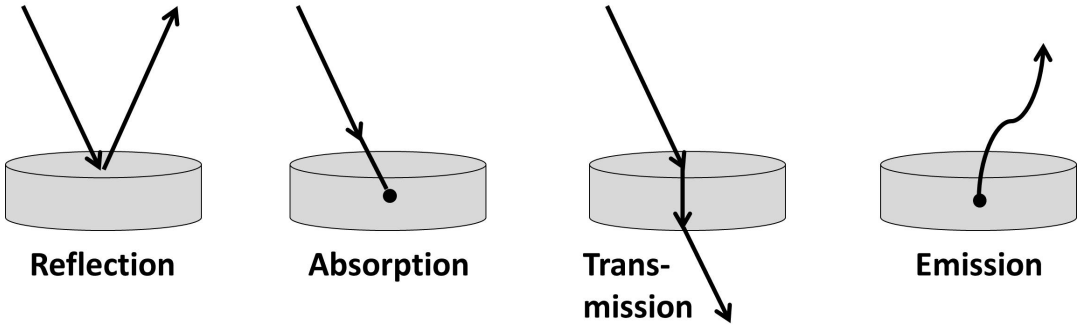

Figure 1.5: Schematic of radiation interactions of a body with incident electromagnetic radiation.

energy of photons into thermal energy of the absorbing body. The effectiveness of these processes can be expressed by introducing reflectivity (ρ_{Rad}, also called albedo), absorptivity (α_{Rad}) and transmissivity (θ_{Rad}), each of which can take values between 0 and 1:

$$\rho_{\mathrm{Rad}} + \alpha_{\mathrm{Rad}} + \theta_{\mathrm{Rad}} = 1 \tag{1.4}$$

Radiative interactions of chemical compounds in the atmosphere are very complex, however the most prominent and important players shall be introduced briefly. The most prominent greenhouse gases are carbon dioxide, methane and also water vapour. They are effective absorbers and emitters of terrestrial radiation in the infrared range of the spectrum, and their effect of emitting downward (i.e. back to the earth surface) longwave radiation drives surface warming, and is commonly referred as greenhouse effect.
Ozone is an important absorber of solar shortwave (UV) radiation, and the ozone maximum at 20–30 km height in the stratosphere leads to effective absorption of UV radiation at these elevated levels. Ozone, clouds and highly reflective bright surfaces on the earth together are causing 52% of incoming shortwave radiation to become absorbed in the atmosphere or reflected back to space, while only 48% gets absorbed by the earth surface. The role of clouds, however, is diverse and must be considered more carefully, as clouds interact with both longwave and shortwave radiation. The radiative effect of clouds is strongly dependent on a variety of cloud parameters, including cloud base height, temperature, optical and geometric thickness, liquid water content, cloud phase, droplet size and interaction with aerosols. Some major aspects of the particular role of clouds in the Arctic climate system will be presented in section 1.2.2.

1.2.1.3 *Surface energy balance*

Radiative energy transfer, together with turbulent heat fluxes, plays a substantial role in the surface energy budget, and the net upward flux F_S of energy at the earth surface is given by:

$$F_S = \underbrace{F_{SW\downarrow} + F_{SW\uparrow}}_{\substack{\text{shortwave}\\ \text{flux}}} + \underbrace{F_{LW\downarrow} + F_{LW\uparrow}}_{\substack{\text{longwave}\\ \text{flux}}} + \underbrace{F_{LAT} + F_{SENS}}_{\substack{\text{turbulent}\\ \text{flux}}} \tag{1.5}$$

The turbulent fluxes include the latent and sensible energy fluxes F_{LAT} and F_{SENS} between the surface and the atmospheric layer aloft. These can be calculated from bulk formula using:

$$F_{LAT} = \rho L_v c_L u_{atm}(q_{surf} - q_{atm}) \tag{1.6}$$

$$F_{SENS} = \rho c_p c_h u_{atm}(T_{surf} - T_{atm}) \tag{1.7}$$

Where ρ is the density of the air, $L_v = 2260\,\mathrm{kJkg^{-1}}$ is the enthalpy of vaporization, T is temperature, q is the specific humidity with the subscripts "surf" and "atm" indicating "at the surface" and "in the atmospheric layer aloft", respectively. $c_p \approx 1\,\mathrm{kJkg^{-1}K^{-1}}$ is the specific heat capacity of air, and c_L and c_h are aerodynamic bulk coefficients depending on a number of surface- and atmospheric boundary layer conditions. Sensible heat fluxes refer to the conductive fluxes of heat from the surface to the atmosphere, with a direct impact on temperature. The flux of latent heat accounts for the energy that is gained/lost through enthalpy changes during the phase transition of water. It is apparent from equations (1.6) and (1.7) that turbulent fluxes will become more important the stronger the wind and the larger the vertical gradients of humidity and temperature between the lower atmosphere and the surface.
The surface energy balance equation (1.5) can be useful to understand the warming in the Arctic and the associated local, vertical feedbacks. Whenever $F_S \neq 0$, there is a net energy exchange between the surface and the atmosphere, that will lead to changes in temperature or phase transitions of water (melting/freezing of snow and ice, condensation/evaporation) at the surface. Hence, Taylor et al. (2018) postulated that radiative and turbulent energy exchange between the surface and the atmosphere will play an increasingly important role in the Arctic, where strong contrasts in the surface characteristics exist between open water surfaces and sea ice/snow cover.

1.2.2 *Peculiarities of the Arctic climate system*

There are several characteristics unique to the Arctic climate system that are not present at lower latitudes. These special circumstances strongly shape the seasonal course of energy fluxes and temperature in the Arctic. They enable effective feedback loops that cause AA,

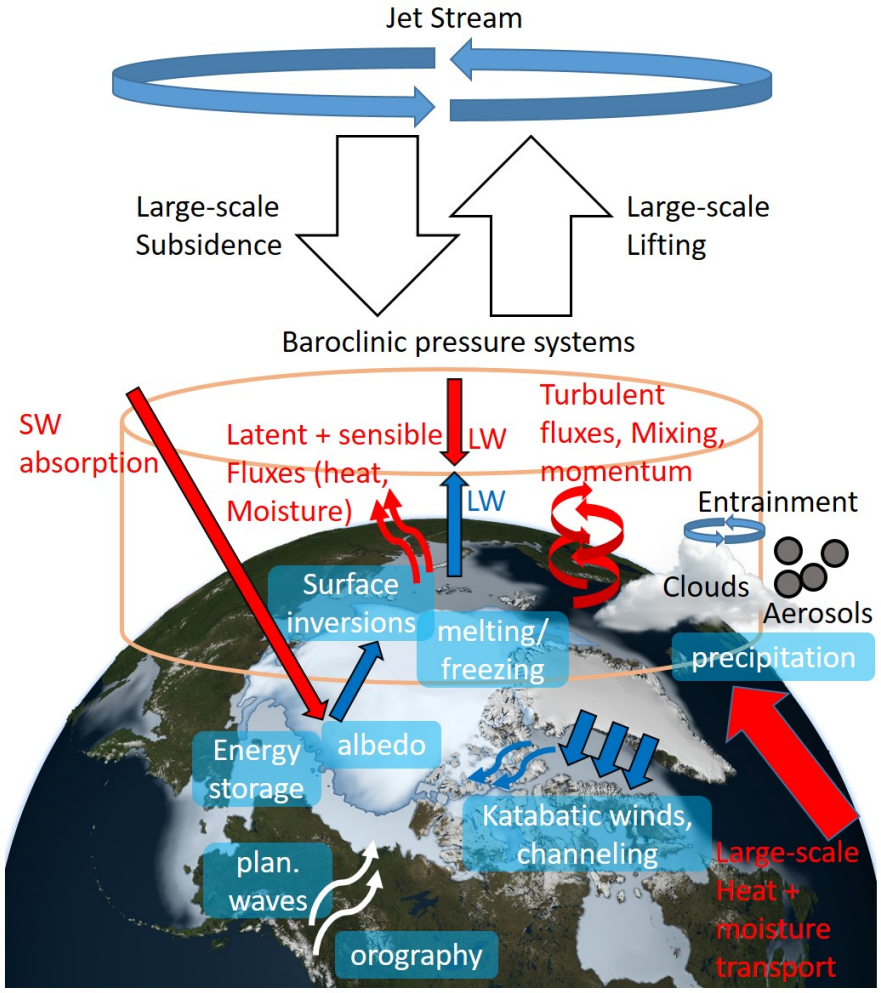

Figure 1.6: Shematic diagram illustrating the complexity of coupled dynamical and thermodynamical processes, and (near) surface conditions of the Arctic atmosphere, which are associated with fluxes of thermal and latent energy and momentum, and strongly shape local climate and weather conditions. Processes that are typically associated with warming in the lower atmosphere are indicated red, while processes renowned for a cooling contribution are indicated blue. White arrows and black text corresponds to processes/parameters, whose temperature effect on the lower atmosphere is either not clear or is of regional or seasonal nature. Schematic is adapted and expanded from Dethloff et al. (2019). Background map: NASA/Goddard Scientific Visualization Studio.

and interfere with each other on an intra-seasonal scale. The most important and prominent ones of these characteristics and processes are summarized in Figure 1.6, and the associated feedbacks will be introduced in the following, however the list is by no means to be viewed as complete.

ANNUAL COURSE OF SOLAR RADIATION At Arctic latitudes, solar radiation is entirely absent during polar night, while the sun does not set during polar day, although at low angles. This seasonal asymetry of shortwave radiative forcing has profound impacts on the Arctic climate and feedbacks. During winter, for instance, the first two terms on the right hand side in equation (1.5) vanish, and longwave radiative fluxes dominate. In summer conversely, incoming shortwave radiation can be used to melt snow and ice, and the energy can readily be absorbed by the ocean to increase the heat content of the upper ocean layer.

SNOW AND ICE SURFACES Snow and ice surfaces are very common in the Arctic regions. They are an essential ingredient for Arctic-specific feedbacks to work, mainly for two reasons. Firstly, they present highly reflective surfaces with albedos of 0.5–0.9, while the albedo of open water surfaces is much lower at 0.1–0.2, depending on the angle of incoming radiation. This opens the stage for feedback processes to set in, and the most prominent one is the "ice-albedo feedback", which is schematically illustrated in Figure 1.7 (a). Solar radiation during the melt season drives enhanced melting of ice, such that larger open water areas get exposed. These can effectively absorb solar radiation,

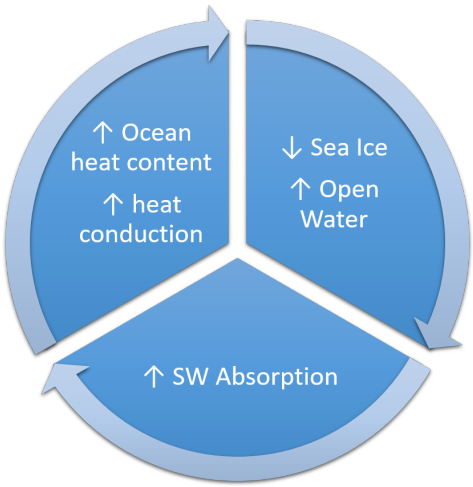

(a) Summer: Sea ice–albedo feedback

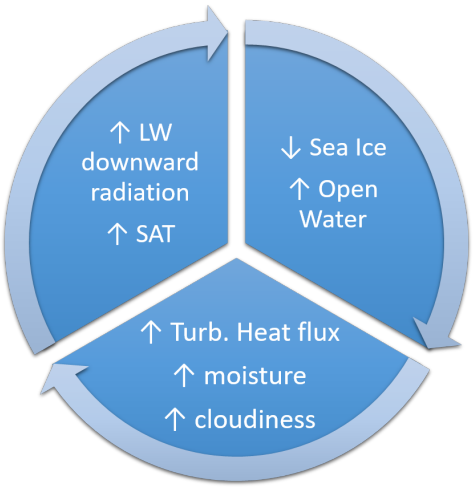

(b) Winter: Sea ice–insulation feedback

Figure 1.7: Schematic illustration of two powerful feedbacks in association with Arctic sea ice coverage. **(a):** Solar radiation during late spring and summer is used to melt ice surfaces, which leaves more open water. These readily absorb heat, driving further sea ice melt and reinforce albedo reduction. **(b):** Sea ice reduction, mainly during winter, exposes warm water surfaces, driving anomalous turbulent heat flux, moisture flux and perhaps cloudiness. These in turn lead to enhanced downward longwave radiation, surface warming and further melt.

and the oceanic heat content in the upper waters is increased, as well as the local SAT. This in turn drives additional ice melting, reinforcing the initial anomaly.
The second important characteristic of sea ice is its insulation power. Particularly in winter and spring, sea ice cover can separate a comparably warm ocean from an atmosphere that may be up to 30 K colder. Accordingly, retreating sea ice during winter has the potential to affect turbulent fluxes, and the sea ice–insulation feedback has gained attention in that respect (Burt et al., 2016). The sea ice–insulation feedback is shown in Figure 1.7 (b). Wintertime sea ice reduction drives excessive turbulent (latent and sensible) heat fluxes from the ocean to the –ideally– much colder atmosphere. This results in atmospheric warming, moisture increase and eventually enhanced cloudiness, all of which provide additional longwave downward radiation to melt further sea ice. Although the sea ice–albedo feedback and sea ice–isulation feedback may occur at the same time and both contribute to further ice reduction, it is crucially important to note that they project on different physical processes. The sea ice–albedo feedback requires available solar irradiance, and by definition no tubulent fluxes, which is only the case from late spring to summer. The sea ice–insulation feedback on the other hand requires no solar irradiance, but involves turbulent heat fluxes via pronounced vertical temperature and moisture gradients (cf. equation (1.6),(1.7)), which happen to occur mainly in winter. An inter-seasonal link between these two feedbacks has been put forward, implying that the additional energy that gets absorbed by the ocean during summer, gets released to the atmosphere in winter, leading to the winter–amplified nature of AA (Bintanja and Van der Linden, 2013; Taylor et al., 2018). However, an actual quantification of these cross–seasonal energy exchanges in the Arctic still stands out (Screen and Simmonds, 2010).

STABLE BOUNDARY LAYER AND SURFACE-BASED INVERSIONS

The planetary boundary layer (PBL) is the lowermost layer of the atmosphere that is connected to the surface and associated surface forcings, such as terrestrial radiation and frictional forces from interactions with topography, that typically drive vertical wind shear within the PBL (Stull, 2012). These processes can induce turbulence, depending on the PBL stability. The existence of small scale turbulence is a fundamental difference between the PBL and the free atmosphere aloft, that is to a good degree in geostrophic balance. PBL stability can be analyzed by the non-dimensional Reynolds number, which compares the inertial forces to the viscous forces:

$$\mathrm{Re} = \mathrm{vL}/\nu \tag{1.8}$$

Where v is the wind velocity, L is a characteristic length scale and ν is the kinematic viscosity of the air. When $\mathrm{Re} > 1$, inertial forces exceed

the viscosity, and flow instabilities can be produced.
A turbulent flow regime can also be accomplished dynamically by vertical wind shear. The non-dimensional Richardson number compares buoyant forces with the vertical gradient of the wind shear:

$$\mathrm{Ri} = \mathrm{N}^2/(\mathrm{du}/\mathrm{dz})^2 \tag{1.9}$$

$$\mathrm{N} = \sqrt{-\mathrm{g}/\rho_0 \cdot \partial\rho/\partial\mathrm{z}} \tag{1.10}$$

Where N is the Brunt-Väisälä frequency. N corresponds to buoyant motions of an air parcel and can be thought of as the oscillation frequency of a parcel that is displaced vertically around its neutral density surface ρ_0 in a stratified fluid. Small Richardson numbers indicate that the vertical shear dominates buoyant forces, and theoretical considerations yield that at $\mathrm{Ri} < 0.25$, the flow becomes turbulent.
A way to define the height of the PBL is the surface-based Bulk Richardson approach, that is outlined in Hanna (1969), Zhang et al. (2014), and is applied in Kayser et al. (2017). An expression for the Richardson number as function of height is given by:

$$\mathrm{Ri}(\mathrm{z}) = \frac{\mathrm{g}}{\Theta_0} \frac{(\Theta(\mathrm{z}) - \Theta_0) \cdot \mathrm{z}}{\mathrm{u}(\mathrm{z})^2 + \mathrm{v}(\mathrm{z})^2} \tag{1.11}$$

$$\Theta(z) = \mathrm{T}(\mathrm{z}) \left(\frac{\mathrm{p}_0}{\mathrm{p}(\mathrm{z})} \right)^{\kappa} \tag{1.12}$$

Thereby, $\Theta(\mathrm{z})$ is the potential temperature at height z, $\Theta_0 = \Theta(\mathrm{z} = 0)$ is the potential temperature at the surface, κ=0.286, and u, v are the horizontal velocity components. Iterating the equation upwards from the surface, the first height where critical Richardson numbers $\mathrm{Ri}_{\mathrm{crit}} = 0.25$ are reached, is referred as the PBL height.
The Arctic PBL during winter over sea ice is typically very stable, shallow, exhibits a marked surface-based temperature inversion and is hence rather decoupled from the free troposphere. This results from the combination of the absence of solar radiation, longwave emission at the surface and the insulating effect of sea ice. Temperature inversions and strong stability in the Arctic PBL are thought of as an important feature for AA to work. The concept of the lapse rate feedback is schematically illustrated in Figure 1.8 and outlined in the following. In the tropics, where pronounced convection takes place and atmospheric stability is generally low, an initial warming anomaly at the surface is likely to drive buoyant uplift, such that the warming is distributed over the vertical with a maximum at height. In the Arctic winter PBL in contrast, strong stability forces the surface warming anomaly to stay confined close to the surface. This surface warming has very limited ability to reach elevated altitudes in the Arctic, both because stable conditions prohibit vertical mixing, and the still cold, dry air at the surface has much lower emissivity than the atmospheric layers aloft. As a result of the lapse rate feedback, changes in SAT in

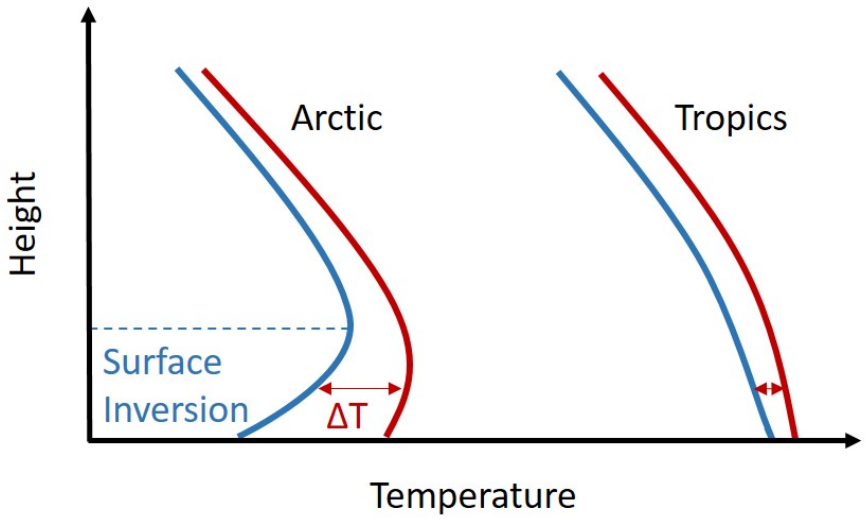

Figure 1.8: Idealized representative temperature profiles for the Arctic and the tropics (blue), and the corresponding changes in the profiles after a warming anomaly has been placed at the surface in each case. Note that in the Arctic, the warming stays confined to the surface layers because of the stable conditions via the surface temperature inversion, while in the tropics, stratification is weaker and surface heating may lead to buoyant uplift, distributing the warming signal vertically over the column.

the Arctic hardly contribute to the TOA radiative budget, such that much higher SAT changes are required to balance TOA radiative imbalances – a positive feedback (Bintanja et al., 2011; Pithan and Mauritsen, 2014). In the tropics, smaller SAT changes are sufficient to counteract TOA imbalances, representive for a negative lapse rate feedback in the tropics.

Other than in mid-latitudes, where the diurnal cycle forces fast changes in PBL characteristics, Stable Arctic PBL can persistent up to several days. Changes are then only induced when the synoptic situation shifts, for example when southerly winds advect warmer air and moisture (Woods et al., 2013; Woods and Caballero, 2016; Knudsen et al., 2018), which is often observed in conjunction with northward moving cyclones. When that is the case, stability may change towards neutral or instable conditions, and the surface-based inversion diminishes. Additionally, low level convective clouds can form in the region of warm and moist air advection, driving downward longwave radiation that warms the surface. There is observation-based evidence for the effectiveness of these processes in the wintertime Arctic PBL (Stramler et al., 2011; Kayser et al., 2017). These studies have also highlighted that the state of wintertime Arctic PBL can readily be described by two regimes, a "clear" state with low cloudiness, strong stability and strong surface temperature inversions, and an "opaque" state with enhanced low-level clouds, low stability and warmer SAT through a

weaker temperature inversion. The transition between these two states occurs due to advection via a changing synoptic flow, and happens approximately instantaneous. In conclusion, it must be understood that the Arctic PBL, particularly during winter, exhibits unique features and processes, that are important for the coupling of the free troposphere and the surface layers, where strongest climate changes are observed.

ARCTIC CLOUDS AND WATER VAPOR As motivated above, Arctic clouds are a key element in the framework of AA, because they are coupled to the PBL and surface processes via radiative and turbulent fluxes. Clouds in the Arctic, and their interactions with the surface are different from what is typical for lower latitudes. Surface heterogeneities with respect to sea ice and open ocean areas, in conjunction with strong temperature inversions and weak solar heating produce very persistent, low level clouds. The much colder temperatures of the Arctic atmosphere compared to lower latitudes allow mixtures of ice crystals and supercooled liquid droplets in these clouds, such that low-level mixed-phase clouds are a frequent phenomenon in the Arctic (Curry et al., 1996; Verlinde et al., 2007; Wendisch et al., 2017). Wendisch et al. (2018) provide an illustrative example for the temperature dependence on the occurrence of mixed phase clouds. They compared the fraction of mixed phase clouds observed at Ny-Ålesund on Svalbard, and at the location of a research vessel in the pack ice 400 km north of Svalbard, where temperatures are much lower, during a campaign in early summer 2017. They found strikingly higher fractions of mixed phase clouds above the pack ice compared to Ny-Ålesund, at the cost of less frequent liquid phase clouds. Cloud phase is particularly relevant, because it determines–together with surface and further cloud microphysical parameters– the cloud radiative effect (Curry et al., 1996; Serreze and Barry, 2011). Cloud interaction with aerosols, ice-nucleation processes, ice and water content in the clouds, particle size and surface albedo determine life cycle and radiative effects of clouds (Curry et al., 1996). This significantly exalts the complexity of cloud effects in the Arctic and has motivated phrasings such as the “Arctic Cloud Puzzle" (Wendisch et al., 2018). Observations of these parameters are generally sparse, hence climate models and atmospheric reanalyses exhibit remarkable biases in cloud-related radiative fluxes (Lindsay et al., 2014).
Throughout my study I am focusing my considerations regarding clouds on their ability to reflect solar radiation back to space, while the low level clouds during winter damp surface cooling via anomalous downward longwave radiation, within the framework of the "clear" and "opaque" atmospheric state, as discussed above. In very much condensed words, Arctic clouds have a warming effect on the surface, with the exception of a short period during summer, when

their effect of reflecting solar radiation back to space has a cooling effect at the surface (Intrieri et al., 2002; Serreze and Barry, 2011; Shupe and Intrieri, 2004). Early climate reports for Svalbard meteorological stations found that daily temperatures between January–March were more than 10 K higher on overcast days compared to clear sky days, while through June–August, clear sky days were slightly warmer than overcast days (Hanssen-Bauer et al., 1990), which confirms the above concept in the vicinity of the archipelago. Using data from a Micro-Pulse Lidar in Ny-Ålesund, Yeo et al. (2018) provide recent evidence that low level clouds during winter significantly enhance the downward longwave radiation, with the highest efficiency for the lowest cloud base heights, and also showed that the occurrence of those clouds is strongly coupled to the large scale atmospheric flow around Svalbard.

1.2.3 *Role of atmospheric circulation*

1.2.3.1 *Preliminary considerations*

Atmospheric motion on the planetary scale is driven by the differential heating rates from incoming solar radition between the equator and the poles. On average, the tropical regions receive more radiative energy from incoming solar shortwave radiation than the polar regions. This results from the inclination of the earth's rotational axis and its spherical shape. On the other hand the earth loses energy by emitting longwave radiation into the atmosphere. The net effect of the solar shortwave and terrestrial longwave radiative contributions is that at the top of the atmosphere (TOA), the tropics are regions of average warming due to an energy surplus, while there is an average energy deficit in the polar regions that implies cooling (see Figure 1.9 (a)). Atmospheric, but also oceanic heat transports from the tropics towards the poles are responsible to balance this disparity (e.g. Trenberth and Caron, 2001), and thus have a crucial role in sustaining the climate around the globe. As indicated in Figure 1.9 (b), outside the tropics the closure is dominated by atmospheric transports, with a peak of 5 PW in the midlatitudes, while oceanic heat transport dominates the tropics. The atmospheric transport maximum in mid-latitudes results from the heat and moisture advection driven by northward propagating cyclones along the Atlantic and Pacific storm tracks, that act to reduce the meridional temperature gradients.

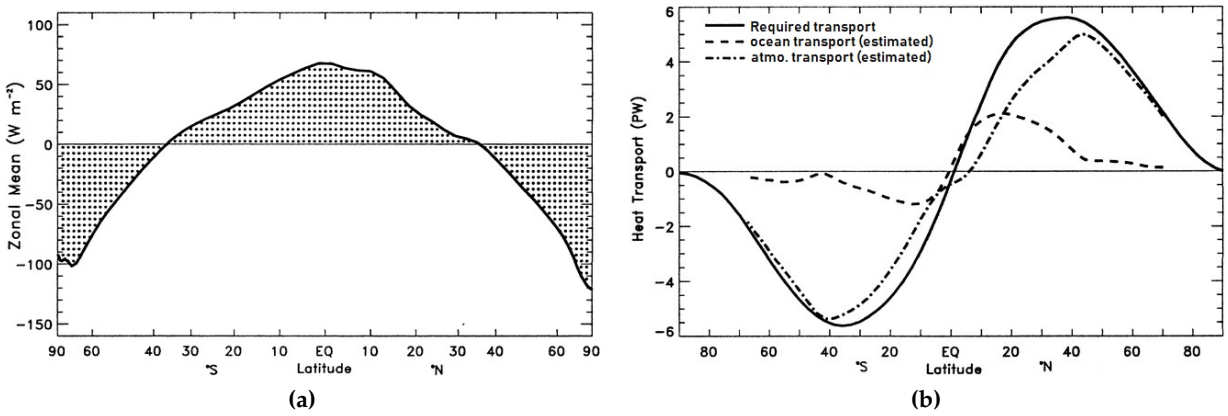

Figure 1.9: **(a):** Top of atmosphere (TOA) zonal mean net radiation during February 1985 - April 1989. Note the surplus in the tropics and the deficit at the poles. **(b):** Required poleward heat transport (solid line) to offset the energy fluxes in (a), estimated atmospheric (dash-dotted), and oceanic (dashed) poleward heat transport during February 1985 - April 1989. Note that atmospheric heat tansport outclasses the oceanic one in mid-latitudes. Graphics are adapted from Trenberth and Caron (2001).

1.2.3.2 *Governing equations*

In fluid dynamics, threedimensional motions can be expressed by the Eulerian equations of motion:

$$\underbrace{\frac{\partial \mathbf{v}}{\partial t}}_{\text{I}} + \underbrace{(\mathbf{v}\cdot\nabla)\mathbf{v}}_{\text{II}} + \underbrace{2\Omega\times\mathbf{v}}_{\text{III}} = \underbrace{-\nabla\Phi}_{\text{IV}} \underbrace{-\frac{1}{\rho}\nabla p}_{\text{V}} \tag{1.13}$$

The individual terms in equation (1.13) correspond to the local rate of change (I), advection (II), Coriolis force (III), gravitational acceleration (IV) and pressure gradient force (V). Thereby, $\mathbf{v}$ is the threedimensional wind vector, Ω is the rotational frequency of the earth, Φ is the gravitational potential, ρ is density and p is pressure. Term III is usually rewritten by introducing the Coriolis parameter $f = 2\Omega\sin\phi$, with ϕ as the geographical latitude. f changes nonlinearly with latitude, but it changes slowly over the spatial scales of synoptic systems. Hence, meridional variation of f is often linearly approximated as $f = f_0 + \beta y$, with f_0 as the Coriolis parameter at a reference latitude ϕ_0, $\beta = \frac{\partial f(\phi_0)}{\partial y}$, and y as the distance to ϕ_0. This concept is called the beta-plane approximation, and typical values of β are of the order of $10^{-11}\,\mathrm{s}^{-1}\mathrm{m}^{-1}$ in mid-latitudes. It should be noted that the Eulerian equations of motion neglect molecular friction, which is a valid approximation for large scale circulation. The continuity equation further requires:

$$\frac{\partial \rho}{\partial t} + \nabla\cdot(\rho\mathbf{v}) = 0 \tag{1.14}$$

In the case of incompressible flows, equation (1.14) reduces to

$$\nabla \cdot \mathbf{v} = \frac{\partial u}{\partial x} + \frac{\partial v}{\partial y} + \frac{\partial w}{\partial z} = 0 \tag{1.15}$$

These concepts are required for understanding the concept of vorticity and planetary wave propagation.
The thermodynamic energy equation follows from the first law of thermodynamics and reads (in pressure coordinates):

$$\frac{\partial T}{\partial t} = -\mathbf{v}_h \cdot \nabla_h T + \left(\frac{\kappa T}{p} - \frac{\partial T}{\partial p} \right) \omega + \frac{J}{c_p} \tag{1.16}$$

Thereby, the subscript “h" refers to “horizontal", $\kappa = R/c_p = 0.286$ with R as the gas constant and c_p as the specific heat capacity of the atmosphere at constant pressure, $\omega = dp/dt$ as the vertical velocity in pressure coordinates and J as diabatic heating term. Similarly, the law for the conservation of moisture reads:

$$\frac{\partial q}{\partial t} = -\mathbf{v}_h \cdot \nabla_h q - \omega \frac{\partial q}{\partial p} - \frac{(C - E)}{L} \tag{1.17}$$

Where q is specific humidity, $C - E$ is condensation minus evaporation, and $L = 2.5 \cdot 10^6\,\mathrm{J kg^{-1}}$ is the latent heat of condensation.

1.2.3.3 *Vorticity and planetary waves*

The relative vorticity of a two-dimensional flow is a measure for its rotational sense, and given by $\zeta = \nabla_h \times \mathbf{v}_h = \partial v/\partial x - \partial u/\partial y$. Vorticity is a useful concept for weather prediction, because the two-dimensinal flow field can be directly infered from it. The absolute vorticity η additionally accounts for planetary rotation by adding the planetary vorticity f: $\eta = \zeta + f$. It can be shown that

$$\frac{d\zeta}{dt} = -\beta v \tag{1.18}$$

With d/dt as the material derivative. Equation (1.18) implies that whenever the velocity field contains a meridional component (i.e. when an air volume is moved towards a region of different planetary vorticity), cyclonicity of the flow will be produced in order to counteract the changes–the so called beta–effect. Extending this concept for three-dimensional flows ($w \neq 0$), the expression for equation (1.18) becomes more complex. However, applying a scale analysis for practical applications of large-scale atmospheric motions, it can be shown that the dominant term in driving $\frac{d\eta}{dt}$ then becomes (Etling, 2002):

$$\frac{d\eta}{dt} = -\eta \nabla_h \cdot \mathbf{v}_h \tag{1.19}$$

This implies that a flow will become more cyclonic (anticyclonic) when there is horizontal divergence (convergence) in the flow, respectively.

For a purely zonal flow with zero initial vorticity, a meridional velocity component would be induced. This meridional velocity component would trigger the beta–effect from equation (1.18), that would act to zonalize the flow again via the induction of vorticity of the respectively other polarity, forcing the air volume back towards its initial latitude. Assuming a zonal mean background flow, as is provided for instance by the hemispheric jet streams in the mid-latitudes, the interplay of a diverging flow field and the beta–effect force a particle on a meridionally meandering path around its initial latitude. These planetary waves are called Rossby waves and can easily be detected as circumglobal anomalies in maps of sea level pressure (SLP) and geopotential height fields. A divergent flow field is required for their generation, and atmospheric divergence is usually generated by the pronounced topography of large mountains or by spatial gradients in diabatic heating profiles, that are typically due to land–sea or ice–sea contrast of the surface. Since both of these are quasi–stationary features, the associated wave patterns tend to project on preferred regional patterns, and they are called quasi-stationary waves.

The winter mean (DJF) circulation at the surface in the Arctic is shown in Figure 1.10 (a), and for summer JJA in (b), respectively. In the winter season, low SLP governs the North Atlantic region. This is an indication that this region represents the preferred pathway of low pressure systems (cyclones) in relation to the North Atlantic storm track. Otherwise the Siberian high can be identified, as well as a central Arctic anticylone. During summer, the circulation is much more sluggish, as the spatial gradients of the climatological SLP field are weaker. However, there are indications for a weak central Arctic low and the Greenland high.
While these represent the climatological circulation at surface levels, the cyclonic and anticyclonic ciculation anomalies that are associated with planetary wave propagation can have major impacts on the regional weather and climate conditions. This is because they also affect the propagation pathways of synoptic-scale weather systems and temperature- as well as moisture advection pathways. These are particularly important in the entrance region to the Arctic, where a comparably cold and dry atmosphere in the north is separated from a comparably warm and moist atmosphere at lower latitudes. Meridional exchanges in both directions across this gradient can have large impacts. An illustrative example for that is given in Figure 1.10 (c) an (d). The qualitative SLP patterns shown in these panels have been calculated with an Empirical Orthogonal Function (EOF) analysis as the two most dominant modes of interannual variability during winter in the domain north of 20°N, with 32.6% and 18.2% explained variability, respectively. EOF analysis, also called principal component analysis, is a popular mathematical method for reducing the dimensionality in large

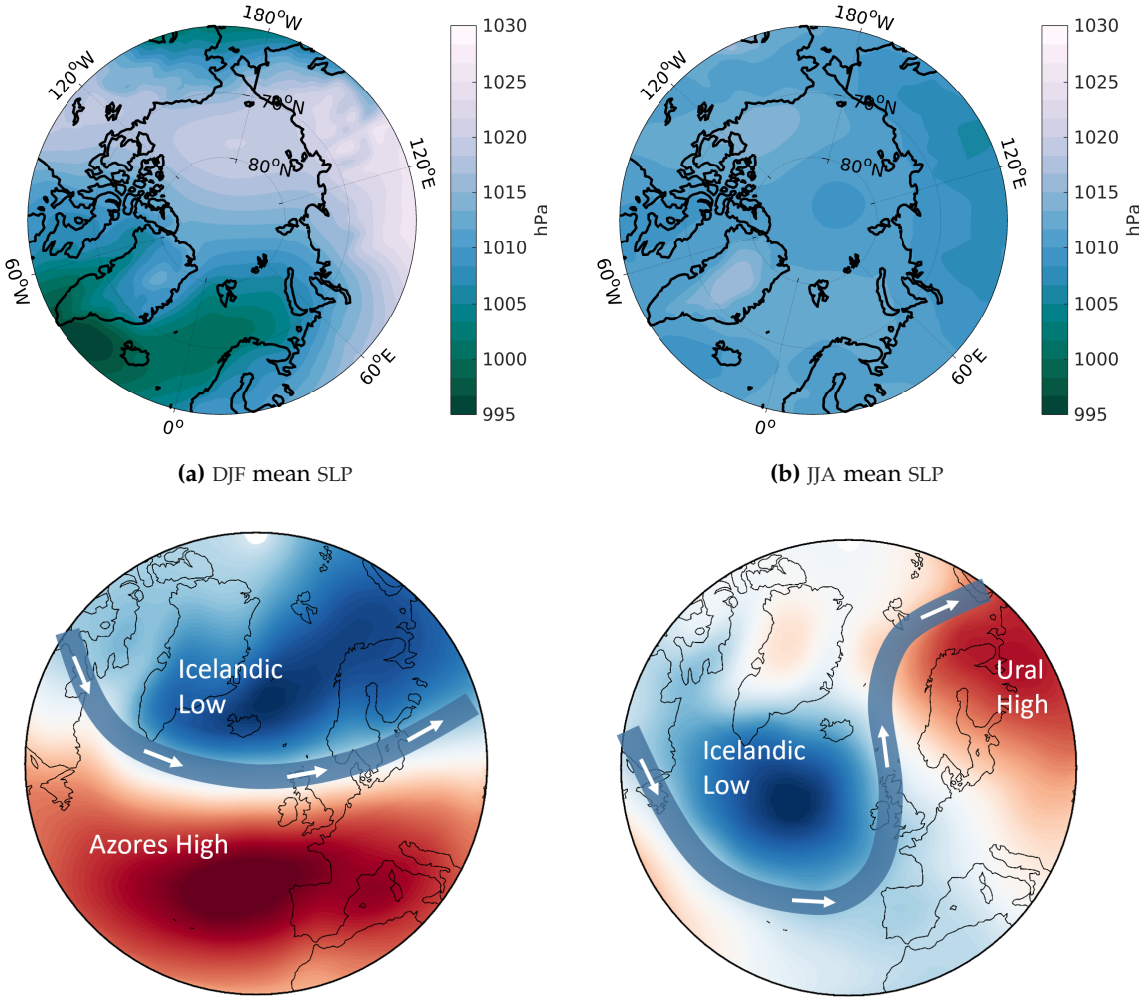

(a) DJF mean SLP

(b) JJA mean SLP

(c) DJF EOF1 (32.6%)

(d) DJF EOF2 (18.2%)

Figure 1.10: **(a):** DJF climatology of SLP from Era-Interim during 1979–2016. **(b):** Same as (a), but for summer (JJA). **(c):** Pattern of the first EOF mode of SLP during DJF from 1997–2016 in Era-Interim, calculated over the domain north of 20°N. Values are arbitrary, and blue (red) denotes anomalous low (high) SLP, respectively. Belts and arrows schematically indicate the associated circulation to the SLP patterns. Explained variability is given in the Figure label. **(d):** Same as (c), but for the second EOF mode.

data sets. In short, it seeks to find linear combinations of variables with the aim of maximizing variance, and with the additional constraint of orthogonality between all the combinations. These combinations are called principal components, and the loading vectors of these are called the EOFs. For climate data, the largest fraction of variability is typically captured within the first few modes. A detailed introduction to EOF analysis in climate science is given in von Storch and Zwiers (2001). The pattern in Figure 1.10 (c) resembles a dipole in SLP between

the Icelandic Low and the Azores High in mid-latitudes. This pattern is commonly referred to as the North Atlantic Oscillation, which strongly determines European winter climate through its association with the advection of warm and moist air from the North Atlantic by a westerly wind drift. The constellation in Figure 1.10 (d), on the other hand side, corresponds to a more southward shifted Icelandic Low and variability within the Ural blocking high, and is associated with a meridionally meandering jet stream. Such a circulation favours northward flow over the North Atlantic by a zonal pressure gradient, highly suggestive for northward heat and moisture transport and associated effects outlined in the previous section. These heat transport mechanisms around the jet stream in mid-latitudes are consistent with the atmospheric heat transport maximum in Figure 1.9, which highlights the role of atmospheric circulation for the large-scale distribution of energy.

1.3 THE REGIONAL SETUP ON SVALBARD

GEOGRAPHICAL SETTING Svalbard is an archipelago located between 10°E–30°E, 76°N–81°N, at the oceanic and atmospheric entrance to the Arctic in the North Atlantic ocean. Svalbard consists of a main island, Spitsbergen, and several smaller islands in the adjacent seas, including Bjornøya, approximately 300 km to the south of Spitsbergen. Mountains with elevations of up to 1700 meters, and several fjords on the west and north coast of the archipelago shape the local topography (see Figure 1.11). Approximately 60% of Svalbard is covered by glaciers, and elevated locations experience year-round ice/snow cover. With respect to its high latitude, Svalbard has a comparably warm climate, given its proximity to warm ocean surfaces and currents of the North Atlantic. According to Köppens climate classification, the climate on Svalbard is "Polar Tundra (ET)", because some summer and autumn months exhibit temperatures above the freezing point (Hanssen-Bauer et al., 1990; Førland et al., 1997).

METEOROLOGY Meteorological observations on Svalbard have a long history, starting from the documentations of trappers from the late 19th century. Over the course of the 20th and 21st century, a network of manned and automated observational sites has been established by the Norwegian Meteorological Institute (MET Norway), allowing for comprehensive monitoring across the archipelago (see stations in Figure 1.11). In early studies the large temperature variability was noted, particularly during winter (Hanssen-Bauer et al., 1990). Among Svalbard stations, SAT typically ranges from -16 to -12 °C in winter to +4 to +6 °C during the warmest summer months (Hanssen-Bauer et al., 1990; Førland et al., 1997), but the recent warming in the region strongly affects these estimates.
Precipitation on Svalbard is generally low, because of the stable and

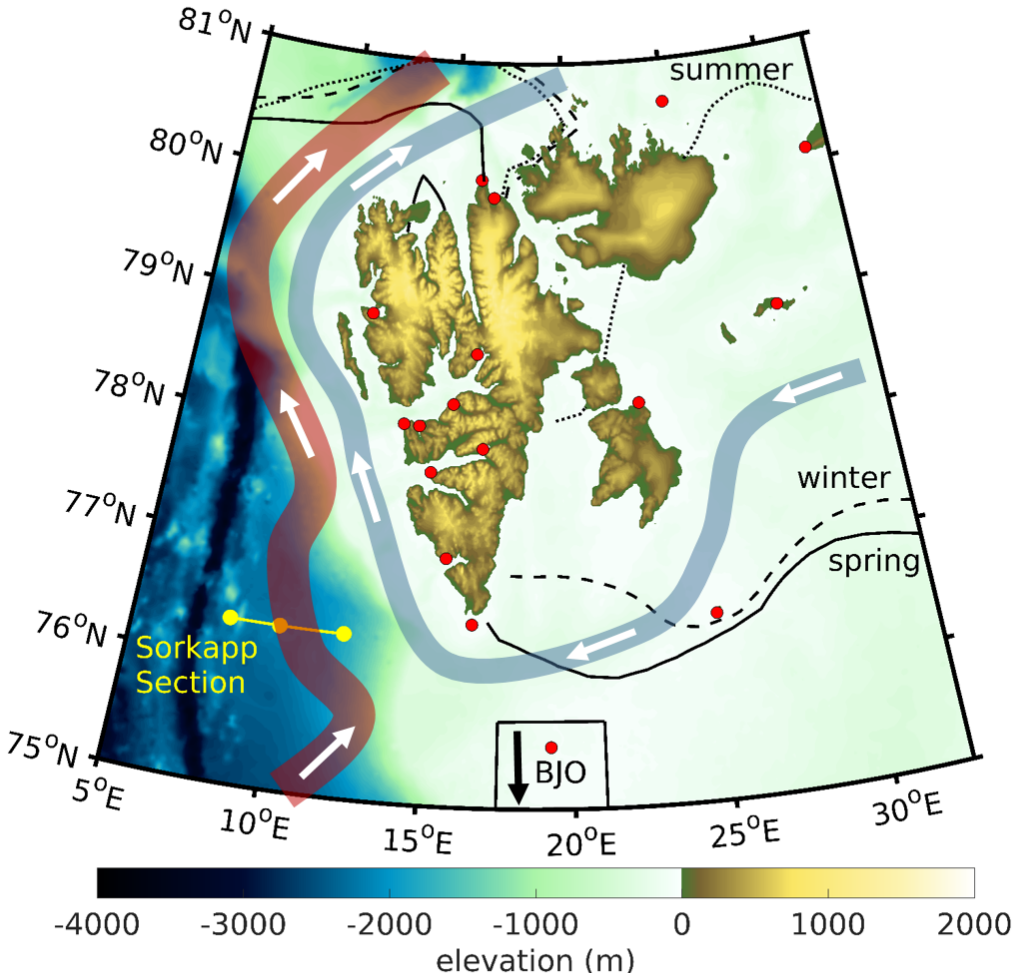

Figure 1.11: Topographic map of the Svalbard area with indicated ocean currents (West Spitsbergen Current [WSC, red], East Spitsbergen Current [ESC, blue]), seasonal sea ice edge locations adapted from Figure 1.3 and meteorological (red dots) and oceanographic (yellow transect) stations. Note that Bjornøya is situated around 300 km south of Spitsbergen. A map giving more detailed information about meteorological stations and sea-ice boxes in the Svalbard fjords and straits is provided later in Figure 3.2.

dry conditions. Based on the 1961–1990 normal period, Førland et al. (1997) estimated annual precipitation ranging from 190–525 mm among the Svalbard stations, with highest values during autumn and winter - consistent with the enhanced cyclone activity at that time of the year. They also showed that both liquid and frozen precipitation may occur over the whole year. However, recent studies indicate that Arctic warming has the potential to manipulate the hydrological cycle, such that precipitation amount and phase are subject to changes (Bintanja, 2018).

The occurrence of cloudiness on Svalbard is broadly determined by the atmospheric flow (Yeo et al., 2018). For five stations on Svalbard

with respect to their historical data records, most frequent overcast situations were observed during June–August, consistently at 50–60% of the time, and less frequent overcast was observed in December and April at consistently 25–30% of the time (Hanssen-Bauer et al., 1990). On the other hand, Cloudnet data based on recent cloud observations from Ny-Ålesund during June 2016–July 2017 reveal an average cloud occurrence of 81% during that time, and in each individual month, cloud occurrences exceeded 50% (Nomokonova et al., 2019). This may be an indication that the recent climate changes also imprint on cloud statistics on Svalbard.

SEA ICE COVER Svalbard is nowadays characterized by predominantly seasonal sea ice coverage, although there is some evidence that prior to the 20th century, the ice edge went further south between Jan Mayen and Bjornøya, making it more likely for Svalbard to experience year round ice cover (Koch, 1945; Isaksson et al., 2005; Divine and Dick, 2006). The 1979–2016 average position of the sea ice edge, computed from the HadISST data set, is shown in Figure 1.11, indicating that Svalbard is situated in the vicinity of the seasonal sea ice edges during winter, spring and summer nowadays. The autumn sea ice edge follows a path slightly north of the archipelago, and is not captured in Figure 1.11. It must be noted that the spatial resolution of the HadISST data set does not account for sea ice in the small fjords of Svalbard, hence a different product will be employed for my investigations of these regions in chapter 3.3.

The West Spitsbergen Current (WSC) acts as a heat source for the western coastal regions of Svalbard. Historically, this has lead to comparably low sea ice conditions and strong seasonality in that region, while in the eastern fjords freezup typically governs the time from November on around Nordaustlandet and then spreads southward towards Storfjorden around January, such that sea ice cover is fully developed in the eastern part of Svalbard around April.

The comparably easy to access fjords in the west have been subject to the majority of sea ice monitoring in the region. For instance, sea ice coverage in Isfjord and Hornsund were studied by Muckenhuber et al. (2016), sea ice thickness was investigated by Gerland and Hall (2006) for Kongsfjord, van Mijenfjord and Isfjord, Kongsfjord additionally by Gerland and Renner (2007) and Wang et al. (2015). Van Mijenfjord sea ice dynamics were subject of Høyland (2009), while sea ice in Storfjord to the east of Spitsbergen was studied by Hendricks et al. (2011) and earlier by Skogseth et al. (2004), who identified the role of the wind in driving the amount of sea ice cover. More generally, in studies regarding the broader Svalbard region it was shown that the combined effect of surface air temperature and the wind can at times yield a reasonable skill in predicting sea ice cover around Svalbard (Onarheim et al., 2015; Isaksen et al., 2016. Like the Barents- and Kara

Seas and the regions around the climatological sea ice edge in the North Atlantic, sea ice cover in Svalbard fjords has seen excessive downward trends in recent years, particularly during the freezup and melting season, which will be investigated in chapter 3.3.

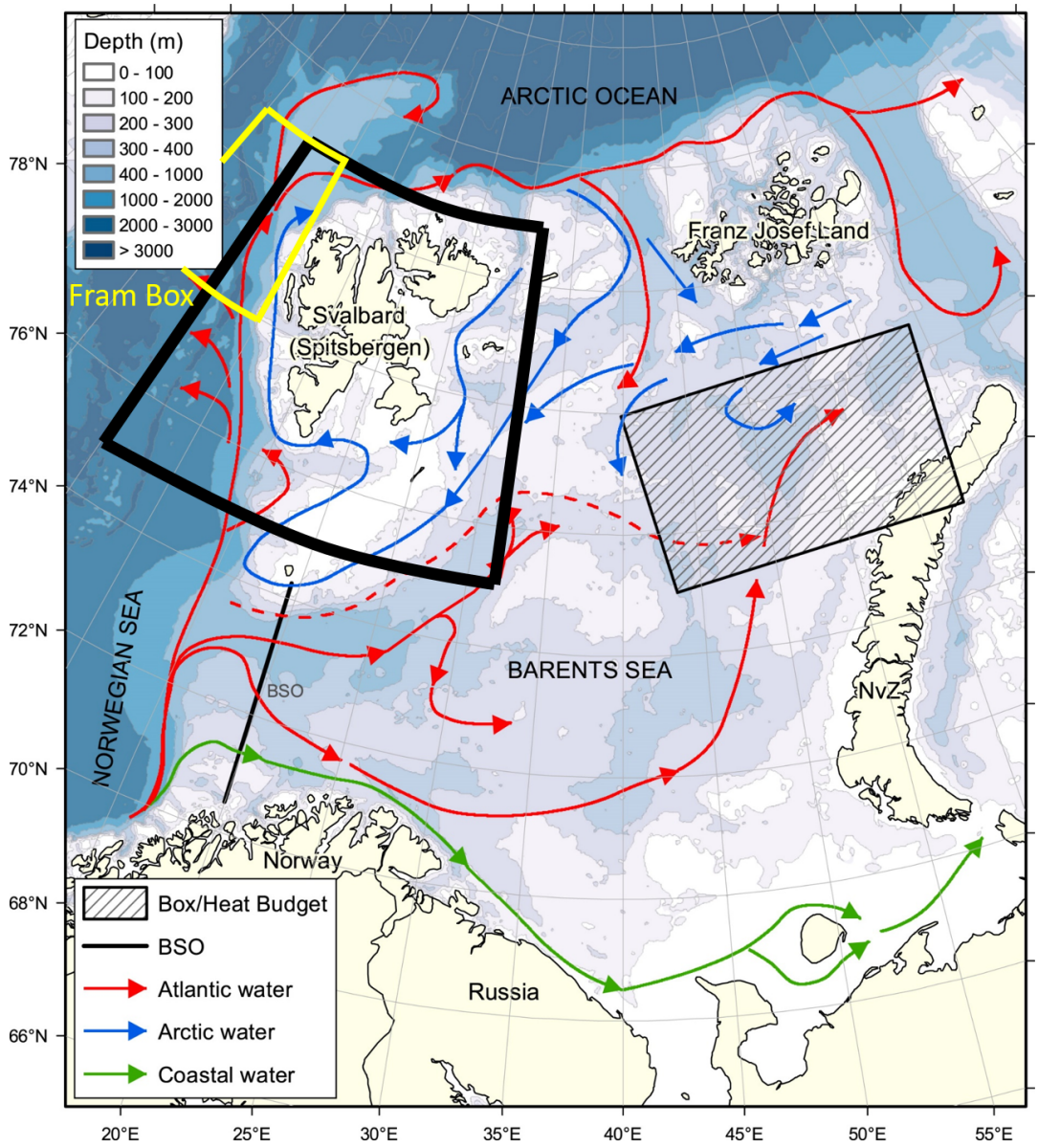

Figure 1.12: Schematic of ocean currents in the broader Svalbard region and in the Barents Sea. Atlantic, Arctic and Coastal waters are indicated by red, blue and green arrows. The Barents Strait Opening (BSO) is indicated by a black line, and the study area from Figure 1.11 by the black box around Svalbard. The Fram Box (yellow) is used in Section 3.3 Figure is adapted and expanded from Lien et al. (2017).

OCEAN The most pronounced oceanographic feature in the Svalbard region is the West Spitsbergen Current (WSC). It originates as a northward extension of the North Atlantic Current, and its strength and variability is controlled by the North Atlantic Subpolar Gyre circulation. The WSC is associated with warm and salty hydrographic anomalies, that propagate northwards along the western coast of Svalbard at about 10 cms^{-1}, while being strongly steered by bathymetry of the continental slope. Strongest hydrographic anomalies within the WSC occur at depth levels between 50 and some 200 m, as surface waters experience excessive cooling along the WSC path. Hence, the WSC provides a remarkable heat source for the local climate on Svalbard (Walczowski and Piechura, 2007; Walczowski and Piechura, 2011; Hanssen-Bauer et al., 2019), and based on measurements during summer and autumn respectively, a total WSC heat transport of about 70 TW (Walczowski and Piechura, 2007) and surface fluxes of 520 Wm^{-2} (Cokelet et al., 2008) were estimated in accordance with the WSC.

Depending on the wind field, pulses of Atlantic water within the WSC can penetrate the western fjords on Svalbard, where typically colder and fresher conditions prevail. It has been proposed that the western fjords can switch between an "Arctic-dominated" state in winter and an "Atlantic-dominated" state in summer (Cottier et al., 2005; Hanssen-Bauer et al., 2019). These hydrographic anomalies have a strong impact on glaciers and sea ice conditions within the fjords (Pavlov et al., 2013; Muckenhuber et al., 2016; Hanssen-Bauer et al., 2019). In particular, the waters of the WSC have had a warming tendency over the last decades (Beszczynska-Möller et al., 2012; Onarheim et al., 2014, with a particular warm anomaly in the winter 2005/2006 (Cottier et al., 2007) and part of the observed sea ice losses in the western fjords may be associated with such events (Muckenhuber et al., 2016).

On eastern Svalbard, the East Spitsbergen current (ESC) transports ice and cold water masses southward, thus contributing to the establishement of sea ice coverage east of Spitsbergen (Hanssen-Bauer et al., 2019). It then continues its path as a shallow surface current and steered by the topography, finally paralleling the WSC in the west. Both WSC and ESC are indicated in Figure 1.11.

Figure 1.12 provides a broader view over major current systems around Svalbard and in the Barents Sea. It is meant to illustrate that the currents are by no means stationary features, but consist of a series of branches and recirculation gyres. It is indicated that the Atlantic water masses of the WSC, after passing Svalbard over the Yermak Plateau, continue spreading eastwards, hence providing heat to the central Arctic Ocean and Franz Josef Land. Moreover, branches of Atlantic Water enter the Barents Sea via the Barents Sea Opening (BSO) and propagate northward towards the ice edge. It has been argumented that these pulses of warm water play a substantial role in

driving interannual and even intraseasonal variations in the sea ice cover variability in the northern Barents/Kara Seas (Smedsrud et al., 2013; Sandø et al., 2014; Lien et al., 2017). The oceanic heat transports in the Arctic North Atlantic ocean must hence be considered as a contributing factor for ongoing climate changes in that region.

2 DATA AND METHODS

2.1 DATA DESCRIPTION

2.1.1 *Era-Interim atmospheric reanalysis*

Over the course of the 20th and 21st century, a tremendous amount of high quality observations of atmospheric parameters have emerged. These include surface data from meteorological stations on land, upper air soundings, ship cruises as well as remote sensing data from satellites. These data are merged alltogehter in so called atmospheric reanalyses products. Thereby, state of the art numerical weather prediction models are used for computations of the past climate. Based on dynamical and thermodynamical physical laws, they integrate the state of the atmosphere forward in time. The nowadays available observations from these past time steps are then assimilated into the model, which increases the quality and consistency of the model outputs compared to the original weather forecast from that time in the past. The advantage of reanalysis products is that they merge scattered observations of various kinds into a gridded, physically consistent data set, that can give insigths into physical processes in the atmosphere. It must be considered however, that the quality of the reanalysis strongly depends on the number of available observations per region, such that larger uncertainties exist in the barely sampled Arctic region compared to the lower latitudes and more populated places.
For my study, specific humidity, wind and temperature at pressure levels, as well as the 2-meter air temperature and SLP are are taken from the reanalysis product of the European Centre for Medium-range weather forecast (ECMWF) [Era-Interim, (Dee et al., 2011)]. Era-Interim performance in the region around Svalbard has been evaluated recently (Graham et al., 2019).

2.1.2 *Svalbard Station Meteorology*

I use monthly mean and 6-hourly surface air temperature (SAT) from 17 meteorological stations across Svalbard. The data are operated by the Norwegian Meteorological Institute (MET Norway), the Polish Academy of Sciences (PAN) and the Arctic and Antarctic Research Intitute (AARI). Details for each station can be found in Table 2.1.2, and a map is provided in Figure 3.2. The MET Norway stations comprise both manned long-term stations that have been in operation for

Table 2.1: Svalbard meteorological stations used in this study and corresponding data availability (from 01/1970 until 12/2016) of daily 2 m air temperature. Periods of data gaps with a length of at least one month are considered *marked gaps*. Geographical location of the stations is shown in Fig. 3.2

.

Station	lat	lon	elev [m]	data	marked gaps	data provider
(1) Akseløya	77.68	14.78	20	08/2008 -	-	MET Norway
(2) Barentsburg	78.06	14.23	40	01/1970 -	-	AARI
(3) Bjornøya	74.53	19.01	16	01/1970 -	-	MET Norway
(4) Crozierpynten	79.92	16.84	22	07/2010 -	07/2010 - 07/2012	MET Norway
(5) Edgeøya	78.25	22.82	14	03/2006 -	04/2006 - 08/2006 02/2009 - 08/2010	MET Norway
(6) Hopen	76.51	25.01	6	01/1970 -	-	MET Norway
(7) Hornsund	77.00	15.54	10	01/1979 - 12/2014	-	PAN
(8) Isfjord Radio	78.06	13.62	7	01/1970 -	07/1976 - 08/1996 01/2005 - 08/2015	MET Norway
(9) Karl XII-Øya	80.66	25.01	5	03/2016 -	01/2008 - 06/2010, 12/2011 02/2012 - 03/2013, 12/2012, 02/2014 - 03/2014	MET Norway
(10) Kongsøya	78.91	28.89	20	09/2010 -	12/2010 - 07/2011	MET Norway
(11) Kvitøya	80.10	31.46	10	08/2011 -	-	MET Norway
(12) Svalbard Lufthavn	78.25	15.50	10	08/1975 -	-	MET Norway
(13) Ny–Ålesund	78.92	11.93	8	08/1974 -	-	MET Norway
(14) Pyramiden	78.66	16.36	20	11/2012 -	-	MET Norway
(15) Sørkappøya	76.48	16.55	10	10/2010 -	-	MET Norway
(16) Sveagruva	77.90	16.72	9	05/1978 -	07/1979 08,09,11/2003, 08/2004	MET Norway
(17) Verlegenhuken	80.06	16.25	8	02/2006 -	almost no data before 10/2010 11,12/2013, 01 - 03/2015, 04 - 07/2016	MET Norway

several decades, as well as autonomously operated weather stations that provide data only during the more recent years. Regarding the four long-term MET Norway stations (Bjornøya, Ny-Ålesund, Hopen, Svalbard Lufthavn), Nordli et al. (2014) have constructed homogenized timeseries, and I use these homogenized data for the pupose of trend calculation and correlations.

2.1.3 *Sea Ice Extent*

Data for the areal sea ice extent (SIE) is taken from daily sea ice charts provided by the Norwegian Ice Service (NIS), which is part of MET Norway. NIS has been producing sea ice charts since 1969, but the quality and spatial and temporal coverage increased significantly with the birth of remote sensing via satellites in the late 1970s. TIROS and NOAA images were used in the early years, and with the availability of improved sensors these were extended over the years. Before 1997, ice charts were printed out every week, and these maps have been digitized later on (ACSYS, 2003). After 1997 however, ice charts have been digitally produced on every week day, and linear interpolation between available charts was used regarding weekends and holidays. Satellite data regarding sea ice extent have continuously added passive microwave imagers such as SSM/I, SSMIS, AMSR-E and AMSR2, while AVHRR, MODIS and VIIRS further enlarged the imaging capability. The biggest breaktrough with respect to regional sea ice charting came with the availability of optical imaging from Synthetic Aperture Radar (SAR). This technique enables high resolution imaging (50–100m), and it is independent of the weather conditions. SAR data became accessible with the initiation of the Canadian RADARSAT-1 and RADARSAT-2 missions in 2005 and 2008, respectively (Scheuchl et al., 2004), and is continuing with Sentinel-1 by the European Copernicus Programme (Torres et al., 2012). Further applications of the historical ice charts can be found in Vinje (2001) and Divine and Dick (2006). Throughout my study, I am applying the catalogue of sea ice charts for 29 extracted fjords and straits in and around Svalbard during the 1980–2016 period. The individual regions are drawn in Figure 3.2. The six differents NIS classifications used to describe SIE are shown in Table 2.2.
Additionally, gridded sea ice concentration data from the HadISST data set (Rayner et al., 2003) has been used for composing Figures 1.3 and 1.11. HadISST data are available at 1° degree spatial resolution and were utilized for the 1979–2016 period. Divine and Dick, 2006 define the ice edge as the separation line between close pack ice and loose drift ice. In an attempt to build on that, I choose the 70% sea ice concentration isoline as ice edge in my study.

Table 2.2: Sea Ice Concentration (SIC) classes used for the operational NIS ice charts.

Ice type	**Concentration**
fast ice	100% last fast ice
very close drift ice	90–100%
close drift ice	70–90%
open drift ice	40–70%
very open drift ice	10–40%
open water	0–10%

2.1.4 *Ocean data products*

Ocean temperature and salinity at the Sørkapp section at the western coast of Spitsbergen have been monitored for decades (Blindheim and Loeng, 1981). Data are provided by the Norwegian Institute for Marine Research (IMR), and they can be retrieved from the online repository of the International Council for the Exploration of the Sea (ICES), where they are provided within the frame of the ICES Report on Ocean Climate (IROC, `https://www.ices.dk/iroc`, see also Larsen et al. (2016)). The section consists of a zonal transect at the southern tip of Spitsbergen, ranging from 8.3°W–12.2°E at 76.3°N. Temperature and salinity are measured by conductivity-temperature-depth (CTD) profiling during ship cruises that take place annually in the summer-autumn season (Lind and Ingvaldsen, 2012). The data hence reflect summer-autumn conditions, however "annual" means are then averaged over three stations along this transect, covering the depth range of 50–200m. Hydrographic anomalies in that transect and depth range are associated with variability of the West Spitsbergen Current (WSC), a comparably warm and salty northward flowing ocean current that shapes the climate of Svalbard (Walczowski and Piechura, 2011) and had a warming tendency over the last decades (Beszczynska-Möller et al., 2012).

2.1.5 *FLEXTRA Trajectories*

The trajectory study outlined in chapter 4 is based on FLEXTRA 3-dimensinal kinematic air back-trajectories. For a documentation of the dataset, see Stohl et al. (1995), Stohl and Seibert (1998) and Stohl (1998). FLEXTRA trajectories are based on the 6-hourly ECMWF analysis fields with 60 levels in the vertical (top level at 0.1 hPa) and a T106 resolution, which translates to 1.125° x 1.125° spatial resolution. An atmospheric analysis is a combination of calculations from a numerical weather model and observations that are assimilated into

the model. This represents the best estimate of the atmospheric state at a given time for the purpose of weather forecasting. Comparison with other kinematic air back trajectory products such as TRAJKS and LAGRANTO shows that FLEXTRA yields very similar outputs (Stohl et al., 2001), with less than 4 % difference between the products regarding the location of the trajectory starting point, relative to the traveled distance after 48 hours. The specific methodology of how the trajectory study is conducted, follows in Section 4.1.

2.2 STATISTICAL METHODS

2.2.1 *Trend estimation*

Throughout the course of my investigations, trends and their corresponding confidence intervals are analyzed using the Theil-Sen trend estimator (Theil, 1950; Sen, 1968). Other than ordinary least-squares approaches, the Theil-Sen trend estimator is an non-parametric estimator, which means that it does not require any assumptions about the statistical parental distribution of the sample data. The trend is based on the median of slopes of all possible combinations of data pairs in the test data, yielding:

$$s = \underset{1\leq i<j\leq n}{\tilde{x}} \left((Y(t_j) - Y(t_i))/(t_j - t_i) \right) \tag{2.1}$$

Here, n is the length of a (time) series, $Y(t_{i/j})$ are observations taken at the time $t_{i/j}$ and $\tilde{x}$ is the statistical median operator. As a result, s is less affected from outliers in the data. Since statistical distributions of sampled climate data are often subject to outliers, as well as non-normalities or non-stationarities, the Theil-Sen trend approach finds broad applications in the field of climate sciences.

TRENDS AND AUTOCORRELATION Another prominent feature of meteorogical and climate data is their tendency to be autocorrelated in time. For trend evaluation this is an issue, because significant autocorrelation impacts the degrees of freedom in the sample data and hence the estimated significance (Yue et al., 2002; Steig et al., 2009). I hence apply a methodology outlined in Yue et al. (2002), called trend-free prewhitening: After s has been calculated, the trend component is linearly removed from the sample data, leaving an anomaly time series Y':

$$Y'(t) = Y(t) - s \cdot t \tag{2.2}$$

In a next step, I computed the lag 1 autocorrelation coefficient r_1 from the detrended sample data $Y(t)'$, and removed it as well from the sample data:

$$Y''(t) = Y'(t) - r_1 Y(t-1) \tag{2.3}$$

Next, the trend component and the pre-whitened anomaly series are blended by defining

$$Y^*(t) = Y''(t) + s \cdot t \tag{2.4}$$

It is obvious that Y^* is no longer affected by the effect of autocorrelation, while it still preserves the original trend. In a last step, the non-parametric Mann-Kendall test for trend detection is applied to the blended series $Y^*(t)$ to estimate whether the trend is significant after all.

2.2.2 *Correlation*

Shared covariability between two time series X and Y can be quantified by the the Pearson correlation coefficient:

$$r = \frac{C(X,Y)}{\sqrt{(\mathrm{var}(X)\mathrm{var}(Y))}} \qquad \text{, where} \tag{2.5}$$

$$C(X,Y) = \langle (X - \overline{X})(Y - \overline{Y}) \rangle \tag{2.6}$$

is the covariance of the two variables X and Y, overbars indicate the mean of a variable and $\langle\rangle$ is the expectation value. Statistical significance of correlations is tested by a two-sided t-test against the null hypothesis that the true correlation is zero. All time series have been linearly detrended before calculating correlations.

2.2.3 *Coefficient of Determination*

In the framework of a linear regression, the observations Y are predicted from a predictand X by letting $Y = \hat{Y} + \epsilon$, where $\hat{Y} = a \cdot X + b$ is a linear combination of the predictand and the predictor, and ϵ is the error of the model. The fraction of variance within the sample data, than can be explained with this linear model can be expressed as the sum of the squared deviations of the regression values to the observed mean:

$$SS_{REG} = \sum_i (\hat{Y}_i - \overline{Y})^2 \tag{2.7}$$

The total sum of squared errors in Y is given by:

$$SS_{TOT} = n \cdot \mathrm{var}(Y) = \sum_i (Y_i - \overline{Y})^2 \tag{2.8}$$

The quotient of Equation (2.7) and (2.8) is referred to as the coefficient of determination. It can then be interpreted as the fraction of explained variance of Y by the linear model. It can be shown that this quotient equals the squared Pearson correlation coefficient (equation (2.5)), such that $r^2 = \frac{SS_{REG}}{SS_{TOT}}$ and the derivation of this relation can be found in the Appendix section A.2.

3

STATE OF SURFACE CLIMATE PARAMETERS: PAN-SVALBARD DIFFERENCES

3.1 MOTIVATION

When it comes to the investigation of processes that are relevant to the Arctic climate, it is essential to be able to build on high quality, long-term data with a sufficiently high temporal resolution. However, such observations are rare in the Arctic. Due to the tough climatic conditions, sparse population density and the extreme logistical difficulties of operating an observational network, only few supersites have been established that are continuously monitoring the climatic conditions and serve as point measurements in the high Arctic. Some of those will be introduced later, and are indicated in Figure 4.1. One exception is the Svalbard archipelago, where historical, as well as recent meteorological and cryospheric conditions are comparably well documented (Hanssen-Bauer et al., 1990; Førland et al., 1997; Nordli et al., 2014; Gjelten et al., 2016). The most rapid sea ice retreat during winter and spring is found in the Barents/Kara Seas further in the east of Svalbard (Comiso and Hall, 2014; Kim et al., 2016; Kim and Kim, 2017) and Figure 1.3, there is also some evidence that the areas of seasonal ice cover surrounding Svalbard are undergoing rapid changes (Onarheim et al., 2015; Isaksen et al., 2016). Likewise, Svalbard happens to be located in the region of strongest winter warming both

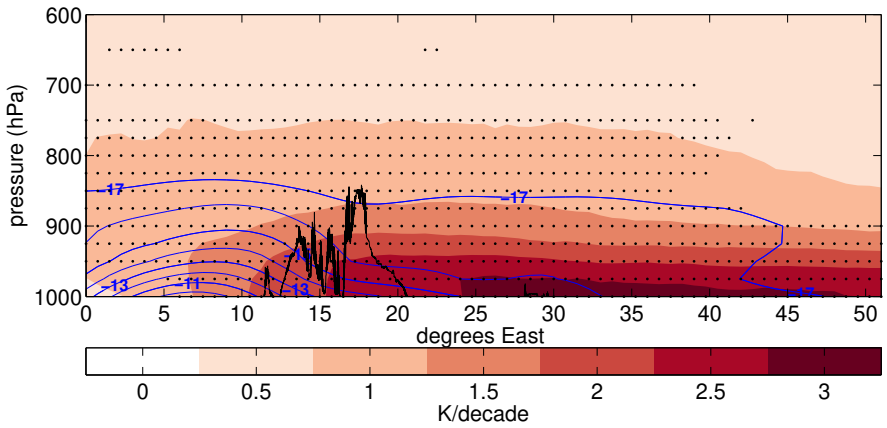

Figure 3.1: Longitude - height section of 1980-2016 DJF warming trend from Era-Interim between 0°E -50°E at 79°N. Spitsbergen topography is schematically shown as black contour. Black dots indicate significant trends (99%). Blue contours show climatological temperatures during the same period in °C.

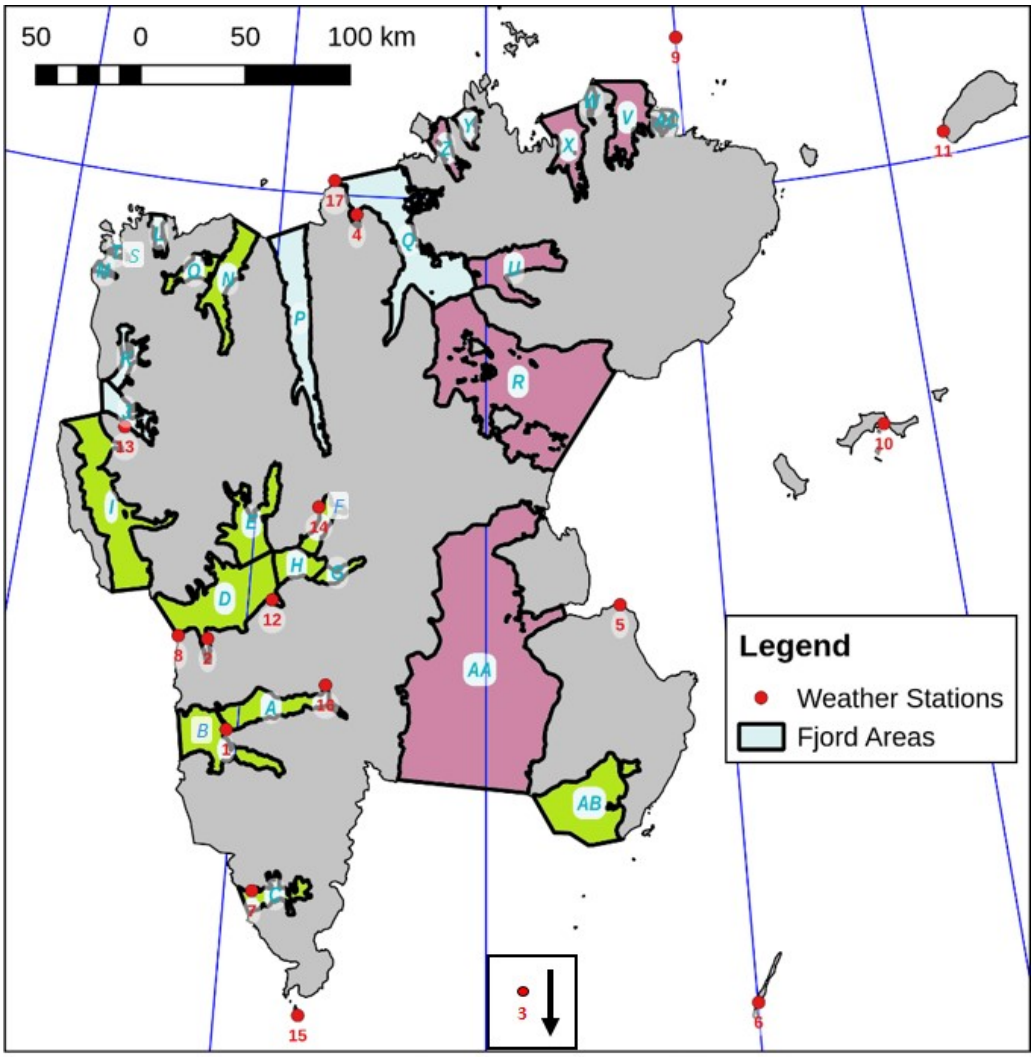

Letter	Name
A	Van Mijenfjord
B	Bellsund
C	Hornsund
D	Isfjorden
E	Ekmanfjorden
F	Billefjorden
G	Tempelfjorden
H	Sassenfjorden
I	Forlandsundet
J	Kongsfjorden
K	Krossfjorden
L	Raudfjorden
M	Magdalenefjorden
N	Woodfjorden

Letter	Name
O	Liefdefjorden
P	Wijdefjorden
Q	Hinlopenstret N
R	Hinlopenstret S
S	Bjørnfjorden
T	Smeerenburgfjorden
U	Wahlenbergfjorden
V	Duvefjorden
W	Zordragerfjorden
X	Rijpfjorden
Y	Brennevinsfjorden
Z	Lady Franklinfjorden
AA	Storfjorden
AB	Tjuvfjorden
AC	Finn Malmgrenfjorden

id	Station
1	Akseløya
2	Barentsburg
3	Bjornøya
4	Crozierpynten
5	Edgeøya
6	Hopen
7	Hornsund
8	Isfjord Radio
9	Karl XII-øya
10	Kongsøya
11	Kvitøya
12	Svalbard Lufthavn
13	Ny-Ålesund
14	Pyramiden
15	Sørkappøya
16	Sveagruva
17	Verlegenhuken

Figure 3.2: (a) Svalbard terrain map with meteorological stations (red dots, corresponding to the stations listed in Table 2.1.2). Operational sea ice coverage data are utilized in the shaded fjord regions. Coloring corresponds to regions of different characteristics regarding the long-term sea ice development, see section 3.3. Note that Bjornøya, due to its southerly geographical location is not included in the map.

near to the surface (see Figure 1.2) and in the free troposphere (Dahlke and Maturilli, 2017). The longitude-height section across Svalbard provided in Figure 3.1 further indicates interesting strong temperature gradients that span across the archipelago. The pronounced warming over the Barents/Kara Seas appears to spread westward, with a declining amplitude towards the west. This impies that the eastern part of Svalbard is more strongly affected by the recent warming than the west coast, where most of the long term measurements are conducted. At the same time, climatological (near) surface temperatures are several degrees warmer in the western part compared to the eastern part, because the West Spitsbergen Current (WSC, see Figure 1.11) is a significant source of heat that affects the atmospheric conditions at the western coast. Given these strong spatial differences across Svalbard, regarding both climatological fields and long-term trends, I here investigate the representativeness of individual regions of the archipelago, and adress the implications for the local sea ice cover within the fjords on the basis of observational data. This has so far only been done on the basis of a limited number of months during campaigns (Przybylak et al., 2014), or with a focus on the Svalbard western coastal region, where most of the observations are focused. The more remote northern and eastern regions are barely sampled. In fact, a recent report of the Norwegian Environmental Agency explicitely states that "the climate of Spitsbergen interior and the surrounding islands is still rather unknown" (Hanssen-Bauer et al., 2019). In an effort to also adress this issue, my analysis combines meteorological data from the Polish Acedemy of Sciences (PAN), the Arctic and Antarctic Research Institute (AARI), the Norwegian Meteorological Institute (MET Norway) and operational sea ice charts (MET Norway) from the whole Svalbard region.

3.2 SURFACE AIR TEMPERATURE

3.2.1 *Annual cycle*

Using data from the 17 stations detailed in Table 2.1.2 and Figure 3.2 I analyze how the annual cycle in SAT differs across Svalbard. The comparison is however complicated by different operational periods between the individual stations, particularly with a long-term warming trend on top. Therefore, I have restricted the comparison of seasonal cycles to those years with available data for both compared stations, respectively. An example of four stations, and how they differ with respect to the other stations, is presented in Figure 3.3. The supersite Ny-Ålesund (Figure 3.3 (a)) may be considered as rather representative for Svalbard, since the SAT cycle differences of the other stations are clustered around zero within the -4 K to +2 K range. An exception is the station on Bjornøya, where due to the

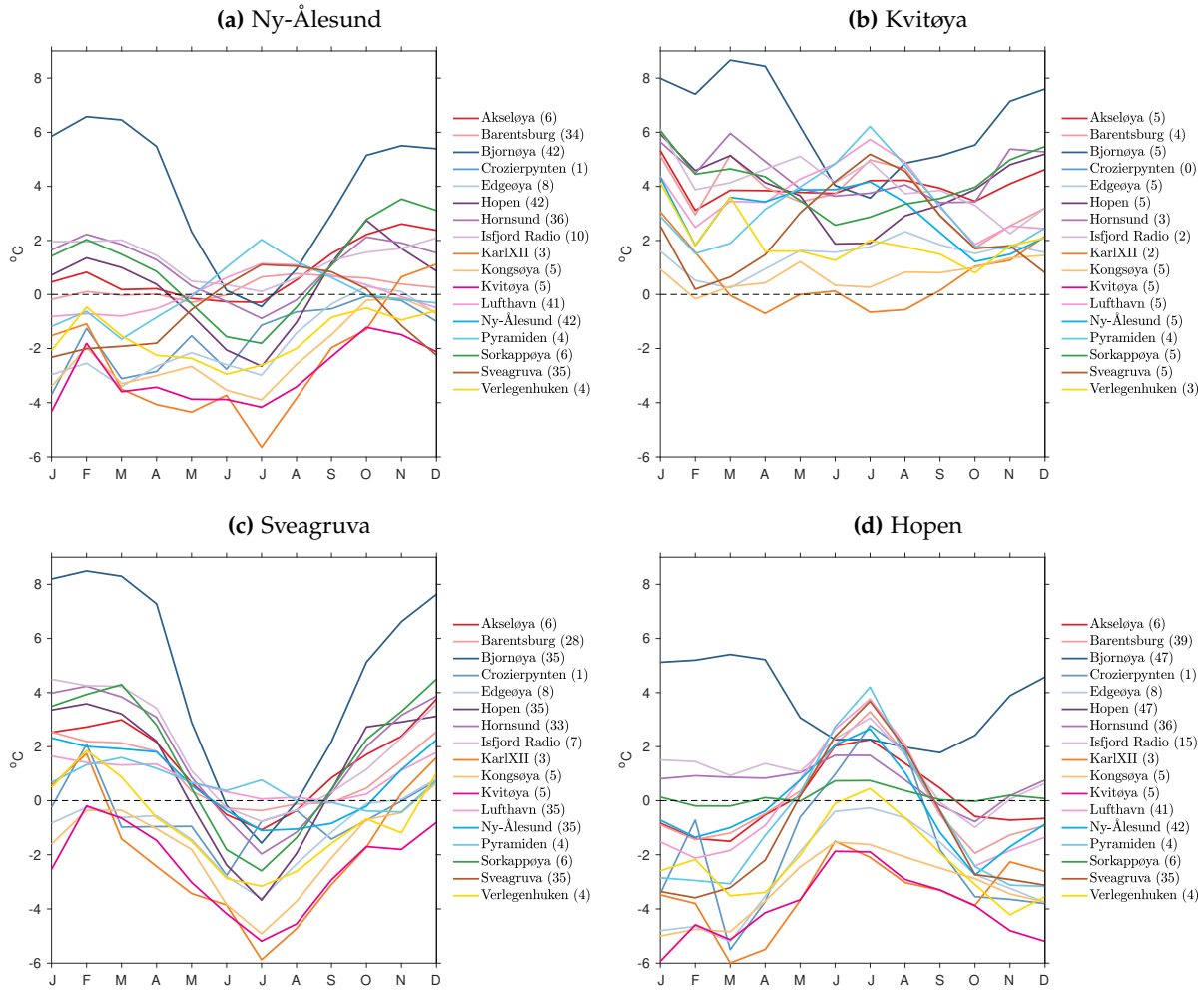

Figure 3.3: Differences in the seasonal cycles of SAT for the period 1970–2016 for the selected stations **(a):** Ny-Ålesund, **(b):** Kvitøya, **(c):** Sveagruva, with respect to all other stations. Each curve represents the difference between the Station in the legend minus the Station in the title of the figure. For the calculation, only years are counted when both compared stations have simultaneous data. Therefore, numbers in the legend indicate the number of years with overlapping measurements with each station.

exposed geographical location south of Svalbard there prevail distinctively warmer temperatures, particularly during the winter months (up to 6 K). However, it is interesting that Svalbard, given its rather small spatial extent of some hundreds of km only, comprises regions that differ this much in the climatic conditions. This clearly reflects the difference of stations of rather maritime conditions in the west and south, that are in close proximity to the warm water masses of the WSC, and those further in the north and east, where a colder continental climate and more persistent sea ice cover can be expected. The station Kvitøya (Figure 3.3 (b)) serves as an example for the latter

group. Regarding SAT, throughout the entire year Kvitøya is among the coldest stations of the entire ensemble, with differences ranging between 0–6 K (with the exception of Bjornøya). This also implies - and will be picked up later - that the northeastern portion of the archipelago is governed by freezing conditions for a longer period of the year than, for instance, the highly sampled fjords on the west coast. It should be noted however that due to the operational periods of the station, these statements are based on only a few years of data. The station Sveagruva (Figure 3.3 (c)) is located in the center of Spitsbergen, at the end of van Mijenfjord and enclosed by high mountains. It reveals a systematic seasonality in its SAT anomalies with respect to the other sites. While SAT at Sveagruva during winter is by $\approx$ 1–4 K colder than the majority of the other stations, during summer it is by 0.5–5 K warmer than the majority of the other stations. This is indicative for a more continental climate, as was proposed by Hanssen-Bauer et al., 1990 and Førland et al., 1997. Conversely, the station on the island of Hopen (Figure 3.3 (d)) experiences warmer (colder) temperatures during winter (summer), hence projecting on a weaker annual temperature range and a more maritime climate.
My results support the view that Svalbard comprises regions of marked spatial gradients in the climatological SAT background conditions. The regionally varying impact of oceanic and atmospheric circulation contribute to shaping these spatial differences across the archipelago. This has to be understood not only in terms of absolute SAT values, but also in its associated seasonality and amplitude of the seasonal cycle. In the next section, I hence investigate the annual temperature range across Svalbard, as a proxy for continentality, and its temporal evolution.

3.2.2 *Annual temperature range*

Following Ewert (1972), the annual temperature range (ATR) - that is the SAT difference between the warmest and the coldest month at one location - reflects the continentality of the climate. Thereby, large values apply to a continental climate, while a maritime climate yields small values. Continentality of Svalbard has been investigated, but mostly the analyses were focused around the prominent long-term stations on the west coast (Gjelten et al., 2016), or in a higher spatial resolution only on the basis of one single year of measurements (Przybylak et al., 2014). In Figure 3.4 estimates of ATR are presented for each station, respectively. Along with a marked interannual variability, a general reduction of the ATR can be identified at the long-term stations Sveagruva, Ny-Ålesund, Svalbard Lufthavn, Hornsund, Hopen, Bjornøya and Barentsburg. This ATR downward trend appears to be related to the winter-heavy warming around Svalbard, while the summer experiences only modest warming, which is also evident in the

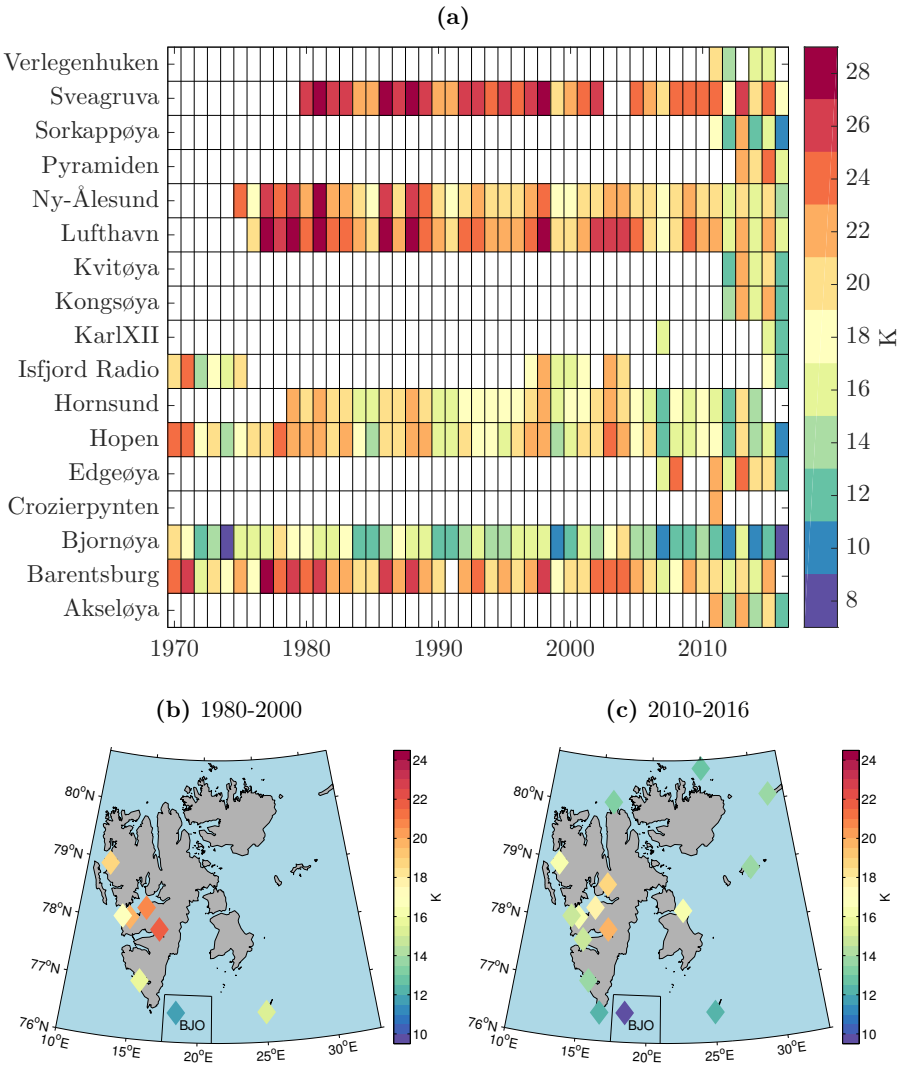

Figure 3.4: **(a)**: temporal evolution of ATR at Svalbard stations. Years with data gaps of at least one month are whitened out. **(b)**: climatological (1980–2000 mean) ATR. **(c)**: Recent (2010–2016 mean) ATR. Note that Bjornøya has been shifted to fit on the map.

reanalysis near surface warming patterns over the north Atlantic sector of the Arctic (Figure 1.2). Figure 3.4 (b) shows the spatial distribution of ATR estimates for the long-term station's climatological period 1980–2000. This period was chosen because firstly, all the long term stations provide data within these years and secondly, it is not contaminated by the strong warming starting in the 2000s. ATR at the stations Bjornøya, Hornsund, Hopen, Isfjord Radio and Ny-Ålesund is by at least 3 K smaller than ATR at the other stations, which evidences the more maritime conditions in the southern and western vicinities of Svalbard, while more continental regimes prevail in the center of the archipelago. The same analysis for the recent years is presented in (Figure 3.4 (c)). Interestingly, the stations in the north/northeast around Nordaustlandet show a consistently small ATR (12–14 K compared to 17–20 K in

the center of Svalbard). This may be rather an effect of the generally year-round cold conditions in theses regions, than of a maritime impact itself. In early studies (Hanssen-Bauer et al., 1990; Førland et al., 1997) it was noted that Sveagruva has the most continental climate on Svalbard. My results using the novel data support this, despite the rapidly proceeding warming in the region. Moreover, it can be seen that the ATR at the long-term stations consistently decreased by 2–3 K in recent years compared to the climatology (Figure 3.3 (c)). Thus, the central regions of Svalbard have recently adapted ATR values comparable to the climatological ones of the stations on the west coast. In the next section, long-term SAT trends from the individual stations are investigated to illuminate what has lead to this shift in the ATR.

3.2.3 *Long-term trends*

In this section, station-based estimates of the long-term SAT development across Svalbard are contrasted. For the sake of consistency, I restrict the analysis to 1980–2016, since several stations were not operating before 1980 (see Table 2.1.2). The climatologies of the stations reflect the aspects brought up in section 3.2.1. At all stations, warming is evident that is most pronounced in the early winter season (December through February). This is illustrated by the significant offset between the climatology and the trend component added upon it in the corresponding months. Interestingly, winter is also the time when marked circulation changes occurr, which will be detailed more in the remainder of this Chapter and particularly in Chapter 4. The fact that the warming is centered in the cold season is also the reason for the decrease in the ATR, that was discussed in the previous section. With the exception of Sveagruva (Figure 3.5 (g)), the stations exhibit weak (<1 K/decade) but significant warming signals during summer, while the winter warming of $\approx$ 2–3 K/decade is markedly stronger, but also has larger uncertainty ranges, given the generally stronger winter SAT variability compared to the rest of the year. It should be noted at this point that large-scale dynamical changes in the atmospheric circulation are contributing to these local seasonal SAT changes, particularly during winter. For instance, Maturilli and Kayser (2017) found, based on radiosonde data, that there is a tendency towards more southerly flow in the atmospheric column above Ny-Ålesund during recent years. Chapter 4 is dedicated to the investigation of links between large-scale circulation- and local temperature changes on the archipelago.

The fact that the peak winter warming is found prior to March interestingly has lead to March becoming the coldest month of the year recently. Figure 3.5 (h) synthesizes the findings on SAT trends. Bjornøya, as the southernmost and most maritime station of the en-

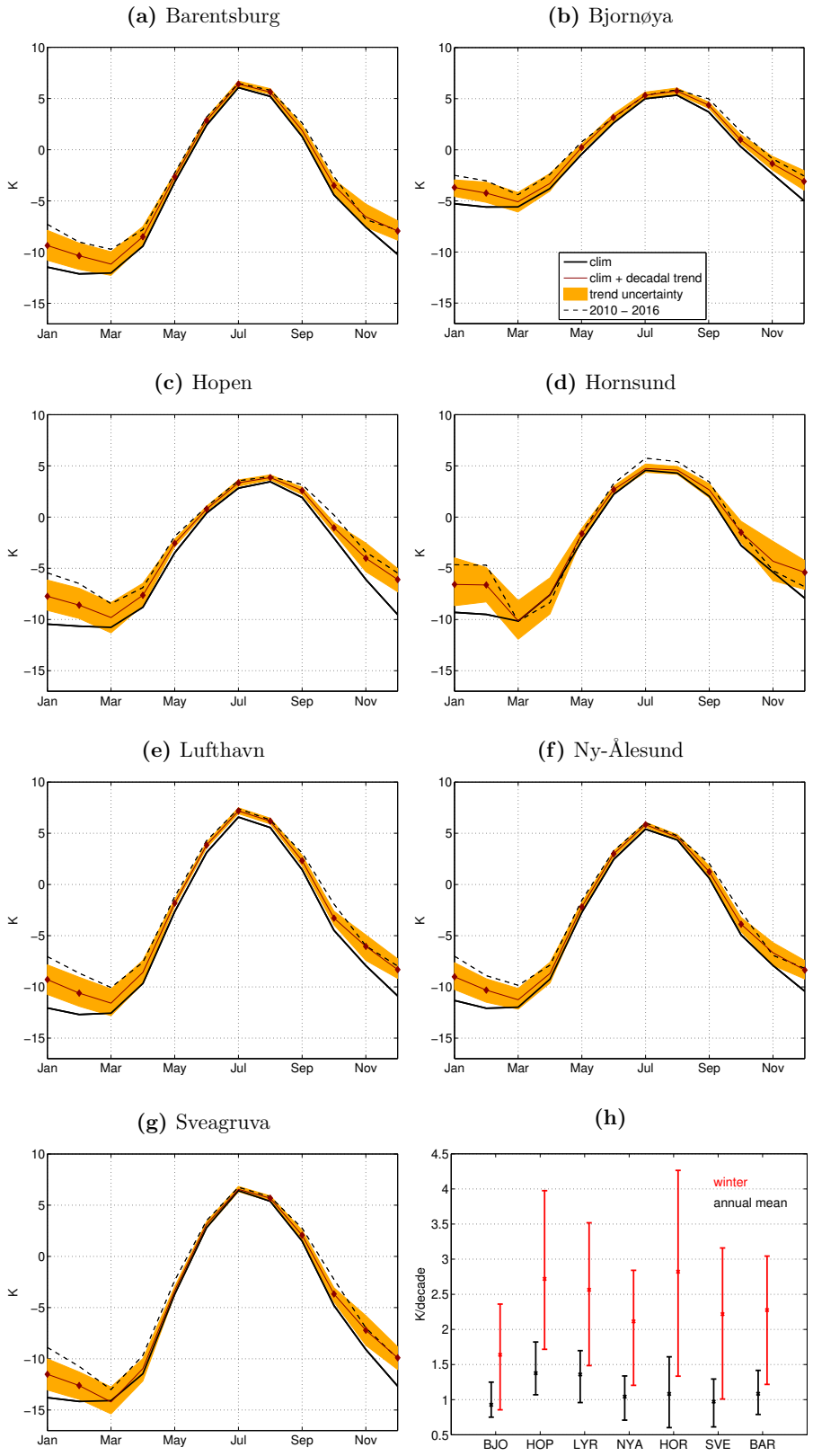

Figure 3.5: **(a)–(g)**: 1980–2016 monthly mean SAT trends for Svalbard long-term stations. Shown is the climatology (solid black), the 2010–2016 mean (dashed black) and the linear decadal trend added upon the climatology (solid red line with ocher confidence interval). Diamonds indicate significance (95%). Note that SAT data are not available at all stations during the full 1980–2016 period (see Table 2.1.2). **(h)**: Annual mean (black) and winter only mean (DJF, red) decadal SAT trends for each station (95% confidence).

semble, stands out with weakest warming and uncertainty. Recalling the zonal gradients of the warming pattern from Figure 3.1, one would expect to see strongest effects in the eastern part of Svalbard. Indeed, when comparing the three stations (from west to east) Ny-Ålesund, Svalbard Lufthavn and Hopen, winter SAT trends increase slightly along that section (2.11, 2.56 and 2.72 K/decade, respectively - see Figure 3.5 (h). However, within the corresponding uncertainty limits, these estimates are not significantly different from each other. Moreover, it should be kept in mind that this transect is also not perfectly zonally oriented along 79°N. The findings provide insights in the recent progression of climate change on Svalbard, and how it spreads over the archipelago. Due to the spatial gradients in continentality, SAT trends and the background climatological state, it becomes clear that these aspects must be taken into account when studying related atmospheric/cryospheric processes and feedbacks in that region.

3.3 FJORD SEA ICE COVERAGE

3.3.1 *Climatology*

The marked regional differences in SAT across Svalbard, that were documented in the previous sections are thought to drive different characteristics in the SIE distribution as well. Analysis of regional SIE is possible by accessing operational ice charts from the Norwegian Ice Service. By merging estimates from 29 regions that span the archipelago, the annual distribution can be contrasted, and Figure 3.6 presents the 1980–2016 monthly mean climatology per region. It can be seen that in all regions, the SIE minimum is achieved by September,

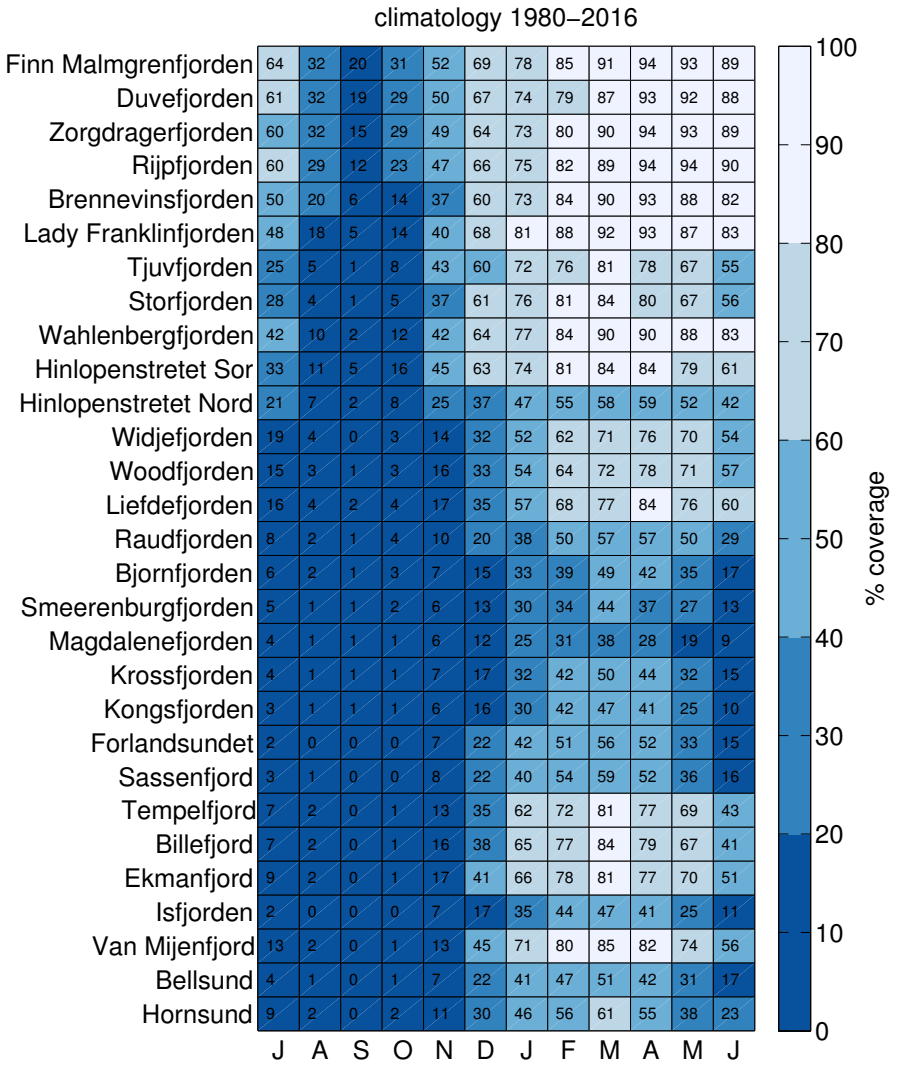

Figure 3.6: 1980–2016 climatology of sea ice extent SIE for the investigated 29 Svalbard fjords and straits (see map in Figure 3.2, based on the daily operational sea ice chart from the Norwegian Ice Service.

while maximum SIE in each region is reached by late winter (March-April). Interesting regional differences appear between a cluster of fjords who are almost ice-free between early summer and November and with mostly only about 50–60% SIE in late winter (panels Hornsund through Wijdefjord in Figure 3.6) and another group with shorter ice-free periods during summer and substantial SIE of more than 80–90% during late winter (regions Hinlopenstret Sør through Finn Malmgrenfjord). It appears that the former group mainly consists of fjords that are located in the west and northwest, where they are in close proximity to the warm Atlantic water surface, and where SAT values are substantially enhanced in comparison to the east/northeast of Svalbard, as I have shown before. By affecting freezup and melt processes, SAT, local wind stress and ocean currents can be strong players in determining and sustaining these spatial SIE differences. As an illustration, for the 2010–2016 DJF seasons I have computed the amount of freezing condition days - that is, when the daily maximum temperature remains below zero (not shown). While this was the case in about 75% (76%) of the days at the western Svalbard Stations Ny-Ålesund and Svalbard Lufthavn, that fraction is sharply increased (91%) at the stations Kvitøya and Kongsøya to the east of Svalbard. Moreover, warm and saline Atlantic water masses can spread the fjords on the west coast (Cottier et al., 2005; Cottier et al., 2007; Nilsen et al., 2008; Pavlov et al., 2013), where they modify the hydrography of the water column and hence may also contribute to climatologically lower SIE than is observed in the east. There, this influence is less dominant and the East Svalbard Current (see Figure 1.11) carries ice and cold waters southward (Hanssen-Bauer et al., 2019). It should also be noted that the large SIE in the eastern parts of Svalbard usually remain quite long into June - a time at which SIE in the western regions typically has fallen towards its minumum already. Representing exceptions, van Mijenfjord, Ekmanfjord, Billefjord and Tempelfjord appear to be mixtures of both characteristics, since they show both rather ice-free summer months and SIE maxima exceeding 80% in late winter. These four fjords are located in the center of Svalbard, where continental climatic conditions prevail and the surrounding mountains favour local wind regimes in the narrow fjords, which also largely decouples them from the large scale processes that may be acting from the west or east. Generally, the surface wind can be a strong driver of sea ice anomalies, by modulating freezup via enhanced sensible heat loss, by ice advection or by mechanically breaking ice. Skogseth et al. (2004) have shown that Storfjord SIE is largely controlled by the local wind field. However, in the often narrow, sheltered fjords on Svalbard, winds are often characterized by katabatic outflow and channeling (Esau and Repina, 2012), which severely complicates studying the effect of wind forcing on ice on such small scales.

3.3.2 *Sea ice cover trends*

The long-term development of sea ice coverage in and around Svalbard has been documented for selected fjords or regions (Gerland et al., 2008; Zhuravskiy et al., 2012; Onarheim et al., 2014; Isaksen et al., 2016; Muckenhuber et al., 2016). Here, I provide a comprehensive overview on Svalbard SIE trends including the remote fjords and straits in the north and east. In Figure 3.7, the trends during a more recent period P2 (1998–2016) are confronted with the trends during an earlier period P1 (1980–1997), and the analysis for the entire 1980–2016 record is also shown. For the latter, the picture is emerging that roughly between December and early summer, SIE has significantly decreased by 5–20%/decade in a vast majority of the fjords. However, for the six fjords from Kongsfjord to Raudfjord, no unequivocal tendency for a trend can be identified. It is interesting that these fjords are regionally confined to the western and northwestern sector of Svalbard. Furthermore, significant SIE reduction sets in one month earlier in November in a number of fjords from Lady Franklinfjord through Finn Malmgrenfjord, where also late winter and spring are not subject to SIE reduction. This is plausible, because strongest downward trends will be expected during the melting and freezup season, when SIE is most vulnerable to changes in its driving factors. Those fjords where SIE reductions are evident already in November are clustered around Nordaustland in the northeast of Spitsbergen, where the still colder temperatures, as reportet in the last section, lead to an earlier freezup season than elsewhere in the Svalbard region. It should be noted in general that trend estimates during the summer and autumn months do not necessarily allow for a physical interpretation, as most regions are then ice-free (see Figure 3.6), with small interannual variations around zero.

The separation in P1 and P2 (Figure 3.7 (a), (b)) gives further insights. From that, it becomes clear that the strongest sea ice decline of up to 20–30% per decade almost only took place during the second half of the record (P2), i. e. 1998–2016, while for P1, i. e. 1980–1997, no such pronounced decline can be seen in most fjords, but rather locally weak SIE upward tendencies are seen in some fjords in the northwestern corner of Spitsbergen during winter (Figure 3.7). It should also be noted that not in all Svalbard fjords strong SIE reductions are evident during P2. Particularly for some fjords around Nordaustlandet to the east of Spitsbergen, the changes over P2 seem imperceptible. Those reflect largely the regions on Svalbard, where climatological SAT is lowest, and SIE is largest (Figures 3.3 and 3.6), pointing towards less vulnerable sea ice conditions when compared to the majority of fjords on the island of Spitsbergen.

It is interesting to shed light on potential drivers of these observed SIE trends and variability, and why they differ spatially across Svalbard as

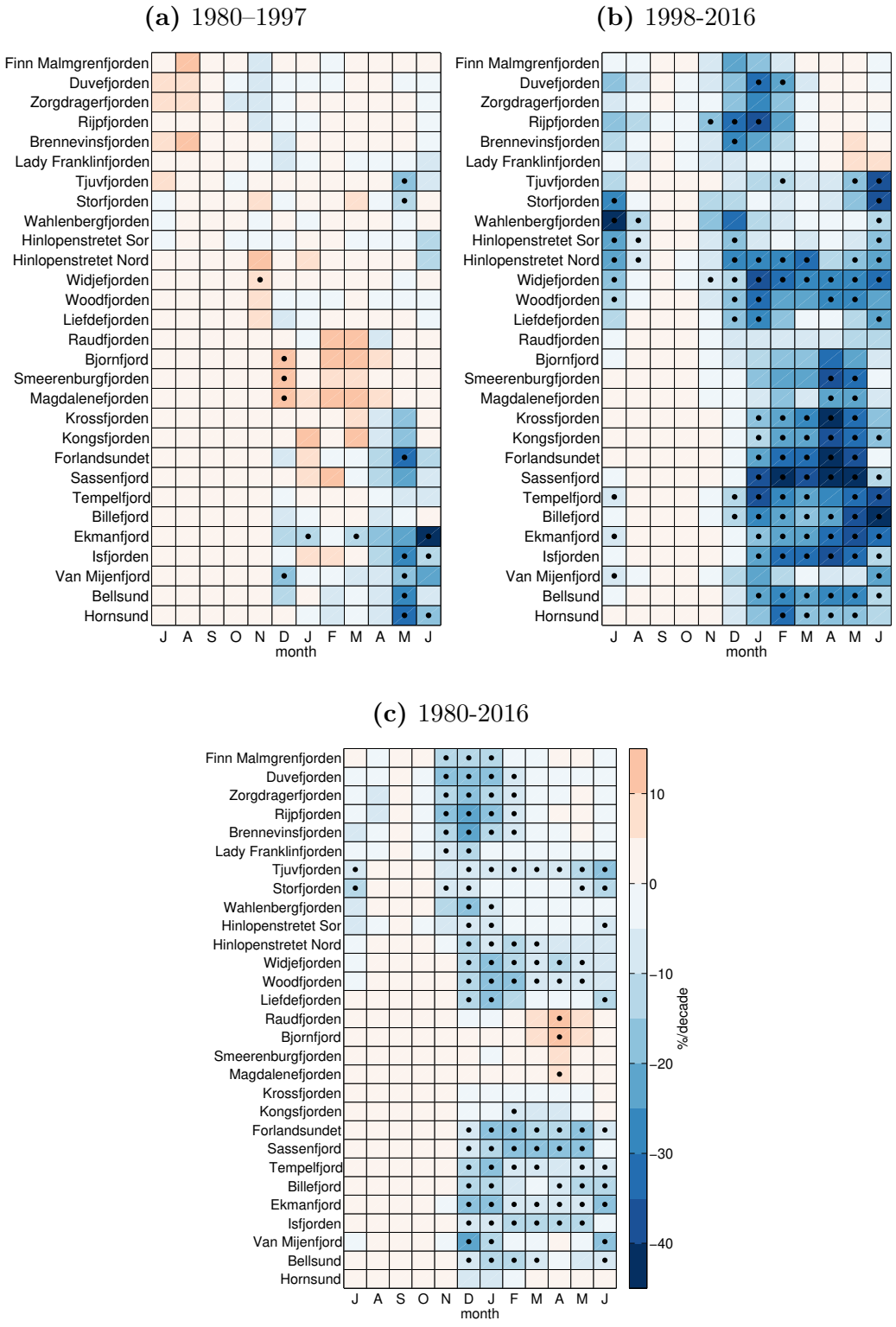

Figure 3.7: Decadal trends of SIE for the 29 investigated Svalbard sub-regions during **(a):** 1980–1997 (P1), **(b):** 1998–2016 (P2), **(c):** 1980–2016.

well as temporally between P1 and P2 (Figure 3.7(a)–(c)). The potential drivers are not limited to SAT forcing alone, because additionally to

SAT, evidence is presented that also the atmospheric circulation in the Svalbard region, as well as the ocean temperature in the western adjacent waters have undergone significant changes during P2 (see Figure 3.9 in Section 3.3.4). A detailed investigation on this, together with a closer analysis of interannual SIE evolution across the Svalbard fjords and straits is subject to the next section.

3.3.3 *Regional classification across Svalbard*

In order to achieve a thorough classification of regional SIE characteristics across Svalbard, time series from all 29 Svalbard fjords and straits have been systematically inspected. Focusing on the late winter season, which is the time of annual SIE maxima, three patterns of temporal SIE evolution are depicted. These are described in the next step, and an investigation of potential physical drivers of these three patterns follows up on that. Among all investigated fjords and straits on Svalbard, the following three classes of fairly distinct temporal SIE evolution were found:

1. No or weak decline in earlier years, followed by strong decline after the mid-2000s. (pattern 1 – western Svalbard, green)
2. Increasing SIE tendency in the 1980s and 1990s, followed by a strong decline (pattern 2 – north/north-western Svalbard, blue)
3. close to 100% sea ice coverage until strong decline in recent years (pattern 3 – north-eastern/eastern Svalbard, pink)

It should be noted that this classification is done by visual inspection of each individual time series and in some cases it appears challenging to assign a pattern to a series. Nonetheless, the method reveals interesting peculiarities on how much SIE conditions can differ on Svalbard, despite the rather limited extent of the archipelago of only some hundreds of kilometers. In Figure 3.8, examples are shown for all three patterns, and their regional distribution across Svalbard is indicated as color coding in Figure 3.2. Generally, it can be seen that SIE increases from November on, until the maximum is reached by March/April, for whose low pass filtered time series the following statements apply. Regarding the pattern 1 fjords, no conclusive statement can be made about any tendency in the time series, until a marked decline commences in the beginning of the 2000s. This decline leaves regions such as Isfjord and Forlandsund almost ice-free in recent years, while they had experienced sea ice coverage of more than 50% two to three decades ago. The same dramatic recent downward trends in SIE are evident for the pattern 2 fjords as well, but with the exception that SIE has had an increasing tendency between 1985–1995. One may be tempted to stress the SIE data quality then, as the high resolution, weather-independent SAR imaging became available from 2005 on

(Muckenhuber et al., 2016). However, the feature is consistently identified over the same period in a set of fjords that are located in the north and northwest of Svalbard, hence it can be suspected that the increase is physically rooted. In fact, a number of studies have adressed southward sea ice drift through Fram Strait, and have identified an increase from a minimum in 1985 to a maximum in 1995 (Vinje et al., 1998; Kwok and Rothrock, 1999; Hilmer and Jung, 2000; Smedsrud et al., 2017). These observations match the pattern 2 behaviour rather

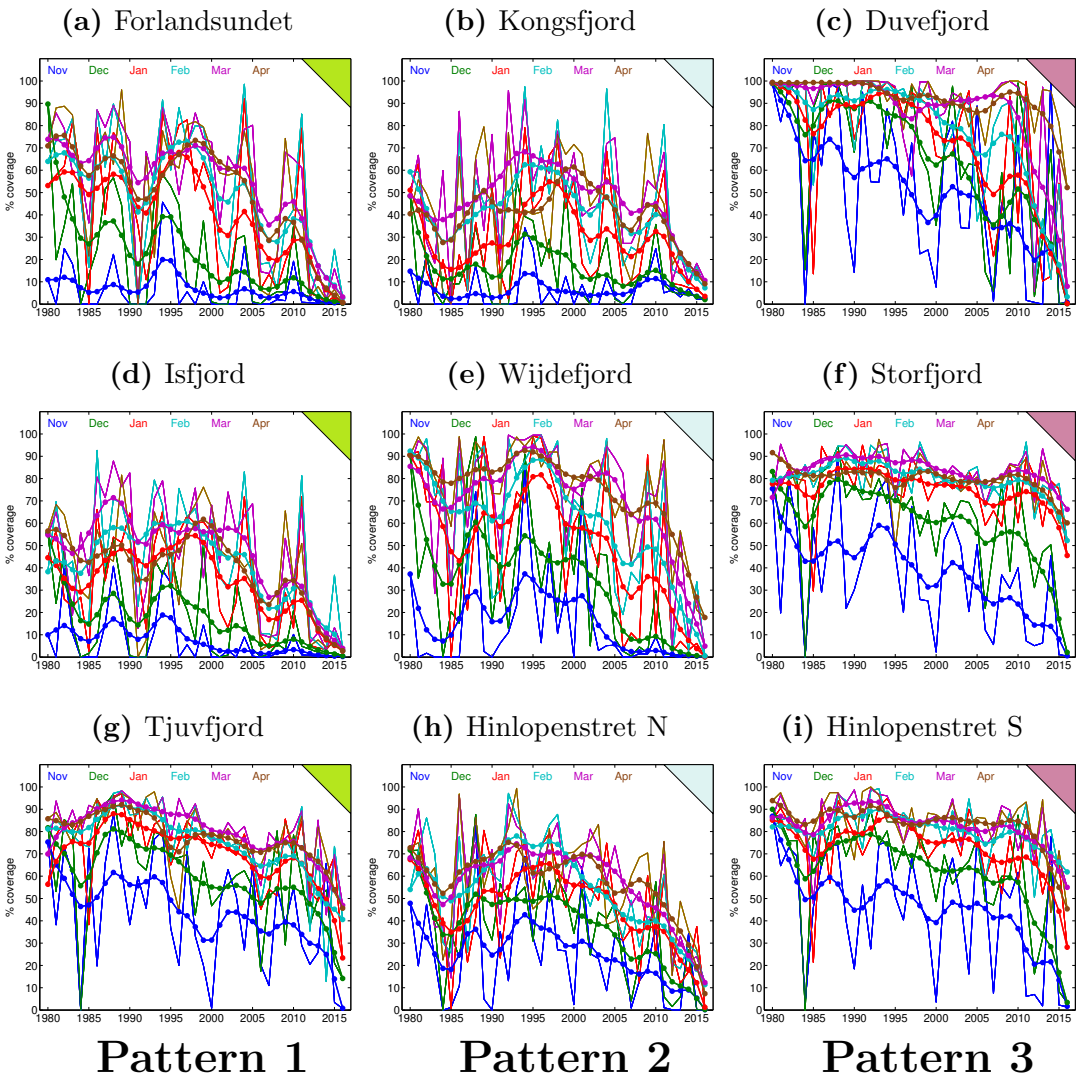

Figure 3.8: Nine examples of SIE evolution across Svalbard. Shown are the months November (blue), December (green), January (red), February (light blue), March (violet) and April (brown). Light curves are monthly mean data, while heavy dotted lines represent 8-year low pass filtered data. Panels **(a)**,**(d)**,**(g)** serve as examples for SIE pattern 1, **(b)**,**(e)**,**(h)** for pattern 2, and **(c)**,**(f)**,**(i)** for pattern 3, respectively (see text). Color shading in the upper right corner indicates the ascription to the regions, as illustrated in Figure 3.2

.

well, and promote the view that local sea ice conditions on Svalbard may be impacted by larger scale drift ice advection, and this potential link is further detailed in the next section.
Pattern three fjords are orderly confined to the east and north-east of the study area, where climatological temperatures are by several degrees colder than elsewhere on Svalbard, but winter warming appears to be somewhat amplified compared to the west (see Figure 3.1). These fjords and straits are characterized by substantial, mostly close to full sea ice coverage during March/April in the early years, with little interannual variation. Over the last decade, sharp SIE decline finds manifestation also in the pattern 3 fjords. Despite the recent decline, the pattern 3 regions have still seen noticeable fractional SIE of at least 40–50% lately, while fjords of pattern 1 and 2 have been approaching ice-free conditions in recent winters. Thereby, even the unfiltered data in some regions like Kongsfjord, Isfjord or Forlandsund have barely exceeded 10% SIE after the last maximum of 2011.
The results demonstrate that sea ice conditions are markedly differing across Svalbard fjords and straits, with regionally differing impact, and a SIE reduction permeating through the entire archipelago that is paralleled by the strong warming in the region. In the next section, the SIE–SAT covariability and other SIE drivers are further investigated.

3.3.4 *Drivers of regional differences*

As outlined above and in Muckenhuber et al. (2016), SIE is a parameter that is sensitive to impacts from various atmospheric and oceanic processes. Here I address the observed co-variability between the SAT, the wind field north-west of Svalbard and the water temperature in the WSC. The individual time series of those are shown in Figure 3.9, and the relations to SIE are discussed in the following.

SAT FORCING AND RELATION TO SAT Here, I aim to stress the local SIE–SAT relationships, for which an inverse relationship is straightforward given that anomalously cold temperatures promote freezing and vice versa. On the other hand, dimishing sea ice cover can also impact SAT via the so called sea ice–insulation feedback (see Chapter 1.2.2). Thereby, larger areas of open water become exposed to the comparably colder winter atmosphere, releasing additional heat and moisture to the atmosphere via latent and sensible heat fluxes. This results in anomalous longwave downward radiation and ultimately drives SAT warming which promotes further sea ice decrease. This downward longwave radiation anomaly can get reinforced by low level clouds that can either form through convection over the opening ice surfaces or get advected by the large scale flow. Burt et al. (2016) estimated, using the Community Earth System Model under a scenario of quadrupling pre-industrial CO_2 concentrations, that the sea ice–

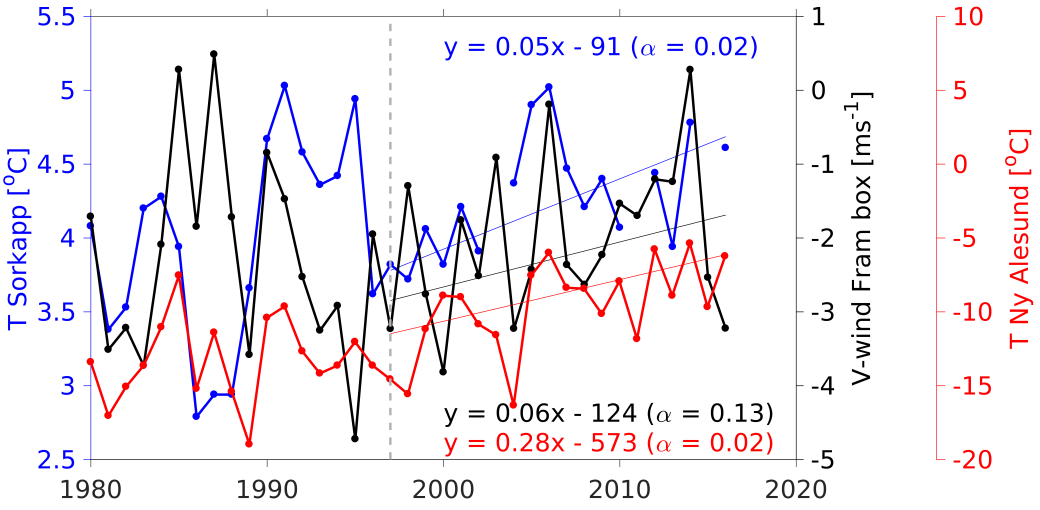

Figure 3.9: Comparison of DJF mean SAT in Ny-Ålesund (red), DJF mean meridional wind averaged over the Fram box [0°E–10°E, 78°N–81°N, see text and Figure 1.12] (black), annual mean ocean temperature at the Sørkapp section (see Figure 1.11), averaged over 50–200 m depth (blue). The vertical dashed line separates P1 (1980–1997) and P2 (1998–2016). Linear trends for each parameter during P2 are indicated in the Figure. Note the common upward tendency of all three parameters during P2.

insulation feedback would drive anomalous downward longwave radiation of 80–120 Wm^{-2} in the central Arctic regions during winter. From that, a portion of 30–50 Wm^{-2} was due to clouds. However, this feedback has garnered attention mostly for the larger-scale Arctic (Burt et al., 2016; Kim et al., 2019). By applying lead-lag correlations to the monthly mean SAT and SIE estimates, I here address the SIE–SAT relations, and an overview is given in Figure 3.10. The application of one month lags is motivated by the comparably large inertia of the cryosphere in reacting to synoptically driven thermodynamic forcing. It was shown before that SIE in many regions is approaching 0% around summer and autumn, and variability is then made up by small departures from zero. Hence, I will focus on the relationships during winter and spring, when variability is physically interpretable in all Svalbard regions. Instantaneous correlations (black boxes) are apparent between October and July, and are most strongly pronounced during winter, when median correlation coefficients exceed 0.5. For the case of SIE following SAT at one month lag, sets of significant correlations appear in all months of the year, but again strongest during winter. Moreover, the resulting median correlation coefficients are slightly larger than the instantaneous ones during all months from October through January. This may be seen as an indication of that sea ice, given its rather long memory, is prone to SAT forcing from the previous weeks. Lagged correlations with SAT following SIE at one

month lag (blue boxes) are not consistently established throughout the winter, and they are in all cases weaker than the instantaneous ones. The results promote the hypothesis that the direct impact of SAT forcing on the sea ice is more dominant than vice versa via the sea ice insulation feedback across Svalbard, particularly during winter. While the above results are based on SAT from the station Ny-Ålesund, qualitatively similar findings are retrieved when applying any other of the Svalbard long term stations (not shown). This illustrates that currently on Svalbard it is the large-scale SAT forcing in the region that sets up the linkage to sea ice variability, although the full complexity of the involved processes cannot be captured with this analysis. On the other hand, the sea ice-insulation feedback is clearly evident in future projections over the wintertime Arctic ocean through the emergence of reduced atmospheric stability (Koenigk et al., 2015) and anomalous downward longwave radiation (Burt et al., 2016). Moreover, only a fraction of SIE variability can be explained with SAT, as the correlations translate to coefficients of determination of r^2= 20–36% only. As was noted by Muckenhuber et al. (2016), SIE is a parameter that directly responds to forcing from many local climate components, such as wind-, air temperature-, and oceanic forcing. It must be understood that additionally to this obvious SAT link affecting the freezup and melt period, other processes must be active in shaping the local sea ice conditions.

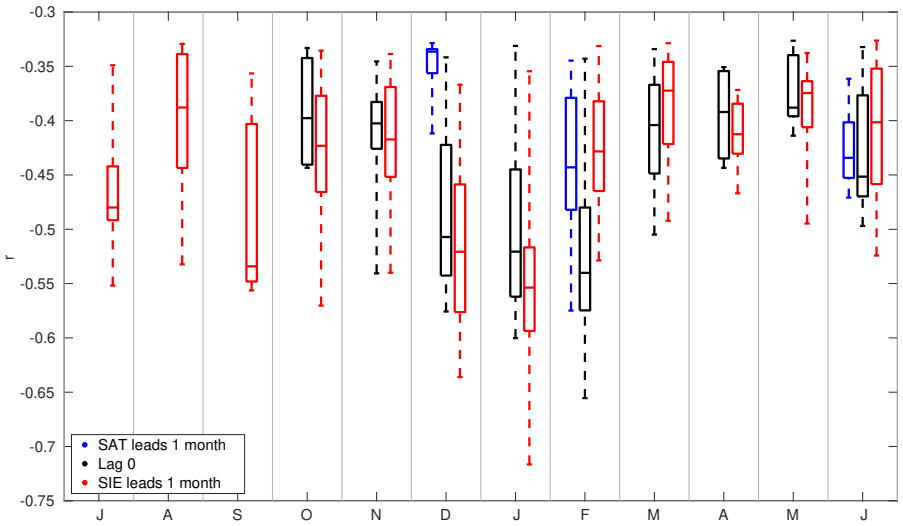

Figure 3.10: Boxplot showing the correlations coefficients of 1980–2016 monthly mean SAT in Ny-Ålesund and SIE in all 29 investigated subregions. Each black whisker represents the set of only significant (95%) SIE–SAT correlation coefficients during the displayed month. Blue (red) whiskers are for correlations when SAT is lagging (leading) SIE in the indicated month by one month, respectively. Each box contains the 25th–75th percentile of each set of correlations, the horizontal line denotes the median, and the whisker covers the whole range.

WIND FORCING Wind stress at surface levels can significantly impact SIE on the regional scale via both mechanically breaking and moving the ice cover and by advecting drift ice from other regions. For the example of the comparably large and exposed Storfjord (see Figure 3.2), Skogseth et al. (2004) have demonstrated that sea ice cover is to a large degree atmospherically driven by the local winds. Such an observational assessment is complicated in the vicinity of the smaller, sheltered fjords on the archipelago, where katabatic outflow, drainage, and channeling effects drive very localized wind regimes (Esau and Repina, 2012) and it is challenging to estimate wind vectors that are representative for each fjord. However, the striking charactristic of pattern 2 fjords, namely the increasing SIE between 1985 and 1995 is interesting, and it appears to go a long with enhanced southward directed ice drift through Fram Strait, that is to large parts wind-driven and documented in a range of studies (Vinje et al., 1998; Kwok and Rothrock, 1999; Hilmer and Jung, 2000; Smedsrud et al., 2017). In order to quantify this potential effect, I have consulted DJF Era-Interim near surface meridional wind in a box over the eastern Fram Strait, that stretches from 0°E–10°E, 78°N–81°N. This area represents a box just off the northeastern coast of Svalbard (see Figure 1.12), where pattern 2 fjords are predominantly located (see Figure 3.2). The resulting time series of meridional wind is shown in Figure 3.9, and both the northerly trend from the mid 1980s to the mid 1990s, as well as the southerly trend afterwards is depicted. The time series bears strong resemblance to the Smedsrud et al. (2017) Fram Strait ice export estimates in the period of overlap (r=-0.87), although these authors base their time series of the meridional pressure gradients across the entire Fram Strait. Figure 3.11 (a) shows coefficients of determination between SIE across Svalbard and the meridional wind in the Fram box for DJF. It can be seen that during P1 (1980–1997), which contains the years of SIE increases in pattern 2 fjords, significant correlations are established in roughly half of the examined fjord regions. These regions are mostly located in the north of the archipelago, and for individual places like Wijdefjord and northern Hinlopenstret, meridional wind in the Fram box alone can explain more than 50% of the observed SIE variability. It is striking that those fjords with largest r^2 estimates preferably extend in the north–south direction, with an opening towards the north (see Figure 3.2). This allows very effective sensible heat losses of the fjord water surfaces, hence promoting freezup, as well as advection of drift ice from the north. Nonetheless, the association of SIE anomalies with the large-scale wind and ice drift west of Svalbard is not robust among all the pattern 2 fjords. Particularly a number of comparably small fjords in the north-western corner of Svalbard do not exhibit significant r^2 coefficients during P1. It should be noted that most of the SIE estimates during P1 stem from passive microwave imagery, which is of coarser resolution than SAR data. This may spread some

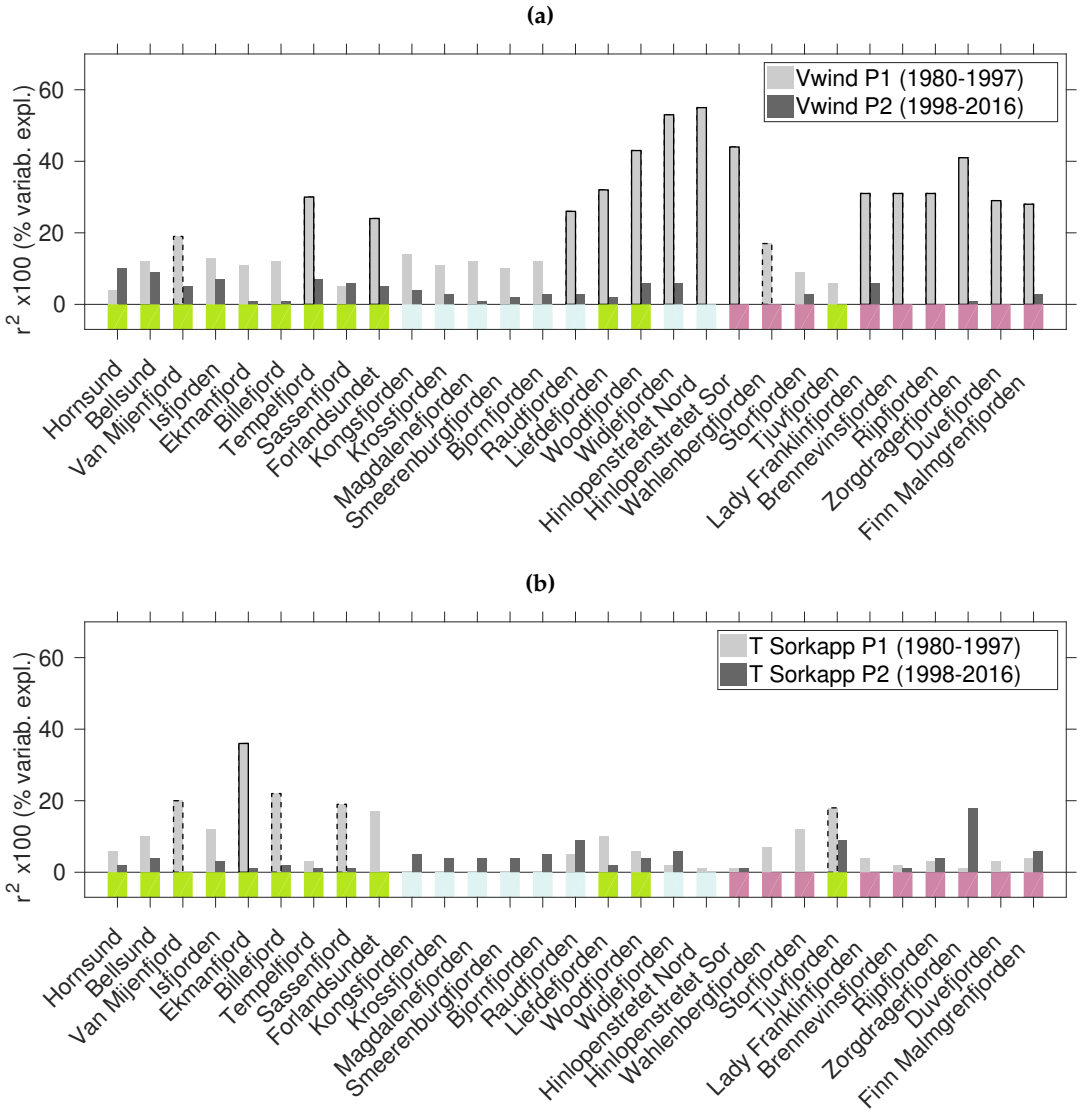

Figure 3.11: **(a):** Coefficient of determination between regional SIE and the meridional component of the wind from Era-Interim area-averaged over the Fram box [0°E–10°E, 78°N–81°N, see text] at 1000 hPa during DJF. r^2 is computed separately for P1 (light grey bar) and P2 (dark grey bar). Solid and dashed outlines of each bar indicate significance at the 95% and 90% level, respectively. Colored markers at the bottom row correspond to the three patterns of SIE development, as introduced in section 3.3.3 and illustrated in Figure 3.2. **(b):** Same as (a), but for the relation between regional SIE and the oceanic temperature at the Sørkapp section.

uncertainty on the estimates for those smaller fjords during the early years of the record.

Regarding P2 (1998–2016) however, it is interesting that the wind–SIE correspondence diminishes in all regions, as no significant r^2 estimates are found in any fjord. A reasonable interpretation of this shift

would be that regions whose SIE used to be impacted by northerly and southerly wind and ice drift anomalies in the 1980s and 1990s, have become increasingly decoupled from those processes in recent years, because the overarching forcing that is represented by the winter warming in the region becomes more and more dominant in determining interannual variability. Moreover the availability of potential drift ice to advect from north of Svalbard is limited by the winter time polynya there. This terms refers to a large area of open water within the ice cover, that is driven by winds or warm ocean water. Extent and occurrence frequency of the wintertime polynya north of Svalbard have reportedly increased in recent decades (Onarheim et al., 2014).

OCEANIC FORCING As pointed out before, the WSC is associated with the northward advection of warm and saline Atlantic water at depths of 50–200 m along the west coast of Svalbard, an it is an important player in shaping local climatic conditions (Walczowski and Piechura, 2011). Specific wind constellations allow the penetration of pulses of Atlantic water into the western fjords, which can in turn become "Atlantic-dominated" in terms of the hydrography (Cottier et al., 2005; Harms et al., 2007). Once penetrated into the fjords, these anomalies alter the thermal energy transport in the upper water layers, representing anomalous heat fluxes with the potential to affect glaciers and fjord sea ice (Cottier et al., 2007; Pavlov et al., 2013; Sundfjord et al., 2017). A statistical assessment of such an impact over the course of decades is challenging, as fjord monitoring has intensified just in recent years. However, measurements at the Sørkapp section provide valuable annual mean data from the summer and autumn seasons since the late 1970s. Hydrographic anomalies in the Sørkapp section take about 2 months to propagate towards Kongsfjord (Onarheim et al., 2014), so an impact on the sea ice conditions in the following DJF season in the fjords seems plausible. The time series of WSC temperature is shown in Figure 3.9, which reveals marked interannual variability during P1 and a significant increase over P2. In Figure 3.11 (b), the same analysis is repeated for the Sørkapp temperature that has previously been presented for the meridional wind. During P1, there is some indication that the WSC temperature anomalies impact sea ice in a number of fjords belonging to pattern 1 only, where about 20% of SIE variablity appears to be associated with it. Notably, in the March–April mean, which is the time of SIE maxima, these relations are even stronger (not shown), such that r^2 exceed 20% in Sassenfjord and Forlandsund, and 30% for Isfjord an Ekmanfjord, at significances of 95%, respectively. As for the wind impact, during P2 the association breaks down, and no statistically significant statements on WSC–SIE covariability can be made, which points towards the dominant role of recent SAT forcing for the pattern 1 fjords as well.

3.4 DISCUSSION AND CONCLUSION

In this chapter, a broad range of observational data covering the 1980–2016 period has been applied, including operational sea ice charts, SAT from Svalbard Stations and hydrographic data of the WSC. The SAT record at the long term stations is found to be representative for the unprecedented winter warming in the North Atlantic region of the Arctic, that is proceeding at a rate of 3–4 K/decade, hence outclassing the annual mean warming of 1–1.5 K/decade. The winter warming is most strongly pronounced during December, January and February, which has lead to March becoming the coldest month of the year in recent years. Along with this warming, a transition of the whole Svalbard region has been demonstrated from winter cold, continental conditions to more maritime conditions. This applies also for the stations in the center of the archipelago, that had formerly experienced the most continental climate. The results also demonstrate the vast rate at which sea ice conditions are changing. SIE among most of the 29 investigated subregions of Svalbard has declined at rates of 5–20% per decade in 1980–2016, but the majority of those trends is motivated by the strong SAT forcing during the more recent years (1998–2016), when SIE has shrunk by up to 30–40% per decade in some regions. As far as it can be regarded using observations alone, lead-lag correlations promote the view that SAT is dominant in driving SIE variability across Svalbard during winter, rather than the other way round via the sea ice-insulation feedback, which is discussed in the context of Arctic warming (Burt et al., 2016; Kim et al., 2019).

In particular, my analysis has revealed interesting Pan-Svalbard differences regarding the long term development of SIE during late winter, that are distributed in fairly regionalized patterns across the archipelago. Along the west coast, weak downward trends have accelerated markedly since the 2000s, while in the northern and eastern sector, close to very close drift ice dominated until the recent years when a strong sea ice decline took place. In the north-western corner of Svalbard, SIE has had an increasing tendency from 1985–1995 in several fjords before the recent decline. Evidence is presented that this increase may in parts be due to enhanced southward winds and associated anomalous ice drift, which was documented for the same period (Vinje et al., 1998; Kwok and Rothrock, 1999; Hilmer and Jung, 2000; Smedsrud et al., 2017). Winter and spring SIE variability in the western Svalbard fjords are further impacted by hydrographic warm and saline anomalies in the WSC, which provide additional heat to the fjords interior. It has for long been known that low-frequency, decadal variability in the North Atlantic Ocean modulates the climate on Svalbard. For instance, Tislenko and Ivanov (2015) examined historical hydrographic measurements in four fjords on the Svalbard west coast. They found that during the early 20th century warming, the cooling

in the 1950s and 1960s, as well as for the warming from 1970 on, that are observed in the SAT, water temperature anomalies of the same sign had prevailed at depth in the fjords. Those fluctuations are in line with the Atlantic Meridional Overturning Circulation (AMOC), that redistributes oceanic heat between the tropical and the (sub)polar regions of the North Atlantic. Inter-decadal variability of the AMOC has been proposed to contribute to AA (Chylek et al., 2009). My results on the other hand show that interannual variability in the hydrography of the Atlantic waters west of Spitsbergen are also related to variability in the local sea ice cover.

However, these impacts appear to be mostly established during the 1980–1997 periods and not anymore in the recent years. This is indicative for that the strong forcing from SAT warming, that affects the freeze-up and melting seasons, has overruled the coupling of SIE to these processes in recent years (1998–2016).

It can be concluded that Svalbard is a natural observatory of the profound changes in the coupled atmosphere–ice–ocean system that large parts of the Arctic are undergoing in recent decades. Increased understanding and monitoring of the involved processes in the highly sampled western fjords can presumably deliver valuable insights in the near-future fate of northern and eastern Svalbard, as well as other parts the Arctic. With an ongoing warming in the region it must be considered that fjords and straits in the northern and eastern parts of Svalbard will become more similar to those in the west, namely by experiencing largely ice-free winters. It can be expected that this and the shift from continental to more maritime climatic conditions will have large impacts on the marine biology, productivity and abundance of species with Atlantic origin as well, as they have already started occupying the region more frequently (Drinkwater, 2009; Buchholz et al., 2012; Berge et al., 2015).

3.5 CURRENT STATE OF CLIMATE PROJECTIONS FOR THE SVALBARD REGION

Climate models can provide valuable insights in the possible future climate in the Arctic, thereby resolving feedbacks and coupled processes such as those studied from an observational view in this chapter. These models are based on physical equations regarding thermodynamics and dynamics. By applying forcing terms to the model equations that represent to the radiative footprint of different greenhouse gas emission scenarios, so called "Representative Concentration Pathways" (RCPs), the models can be integrated forward in time to estimate the effects of RCPs on the future climate. For instance, RCP4.5 accounts for slow increases in greenhouse gas concentrations until the year 2050, and decreasing concentrations afterwards. RCP8.5 assumes that emissions will continue to increase at the rate of prior to 2005, with

no reductions in the future (IPCC, 2013).

Climate projections for Svalbard are complicated mainly for two reasons. At first, Svalbard has a complex terrain with sharp spatial contrasts in topography, SAT and SIE, as was shown in this chapter. The model grid size of state of the art global climate models is of the order of 100 km, which does not resolve the archipelago in a sufficient manner. The second problem is that state of the art coupled global climate models tend to overestimate sea ice concentration in the Arctic, and are not able to simulate the magnitude of the observed recent decline sufficiently, with large spreads between different models (Stroeve et al. (2012b) and Figure 1.4). As was shown in this chapter, today's climate conditions on Svalbard are closely coupled to the presence of sea ice in each region, and the prediction skill of future climate simulations strongly depends on an accurate representation of sea ice around Svalbard, and when it will be gone. Therefore, methods such as empirical-statistical downscaling, as well as dynamical downscaling have to be applied in order to gain information on such local scales. Empirical-statistical downscaling uses empirically determined relationships between large scale processes and local observations that can be statistically implemented in the model. This method requires reliable long term observations of climate parameters in different locations, and valorizes such detailed observational efforts as those on Svalbard presented in this chapter. Dynamical downscaling on the other hand side means that regional climate models, which have a higher grid resolution than global ones, but only cover a limited domain of interest (e. g., the Arctic), are run with output data from global climate models. This enhances the amount of regional information in the output, but is computationally more expensive. *Arctic CORDEX* is an international effort, in which CMIP5 models are dynamically downscaled in the Arctic region. For the following, the reader is referred to Hanssen-Bauer et al. (2019) and references therein for a thorough description of the models that were used in MET Norway's report on climate projections for Svalbard.

Dedicated studies within the Arctic CORDEX initiative show robust evidence that for both RCP4.5 and RCP8.5 scenarios, substantial warming can be expected to continue in the Svalbard region (Koenigk et al., 2015; Osuch and Wawrzyniak, 2016; Hanssen-Bauer et al., 2019). In the most pessimistic RCP8.5 scenario, winter temperatures on Svalbard by the end of the 21st century may be up to 15–20 degrees warmer than the climatological average around the end of the 20th century (Koenigk et al., 2015; Hanssen-Bauer et al., 2019). It is interesting that the large scale warming pattern in the models follows the pattern of sea ice loss in the model, which is consistent with the sea ice-insulation feedback (Koenigk et al., 2015; Burt et al., 2016). These studies also highlight significant changes in precipitation, SLP, atmospheric stability, sea ice concentration and cloudiness. As was detailed throughout this chap-

ter, clouds are an important player for the climate in the Arctic, but Koenigk et al. (2015) show that projections of cloud cover in a warming Arctic differ substantially between their global and regional climate models, pointing towards the importance of the parametrization of cloud microphysics.

Dobler (2019) has run the COSMO-CLM at convection-permitting scale (≈2.5 km spatial resolution) for the Svalbard region and under the RCP8.5 emission scenario. For the comparison of the mean state with the observed sea ice concentration from the HadiSST data set, the model performed rather well, but it produced too much sea ice north of Svalbard and west of Novaya Zemlya. Sea ice concentration in the 2060s is estimated to be up to 40% below todays levels in the Barents/Kara Sea between Svalbard and Novaya Zemlya. Sea ice concentration is predicted to be slightly higher in some localized regions in Storfjorden and Hinlopenstredet, but these are regions where SST is predicted by the model to show no or a slight downward trend (Hanssen-Bauer et al., 2019). However, sea ice concentration in the Barents/Kara Seas is in large parts determined by the inflow of comparably warm waters through the Barents Sea opening to the south of Svalbard, and no CMIP5 model is cabable of reproducing such a warm inflow sufficiently, which spreads some uncertainty on the sea ice projections around Svalbard (Smedsrud et al., 2013; Sandø et al., 2014; Hanssen-Bauer et al., 2019).

Overall, state of the art climate models still show large uncertainties regarding future projections in the Svalbard region. Realistical representation of surface conditions and associated turbulent and radiative fluxes appear to be key for skillful predictions. Factors determining the surface conditions and processes –mainly the representation of sea ice–need to be better understood and implemented in regional climate models. Availability of detailed observations of related climate parameters are therefore essential for evaluation of the models.

4

AIR MASS BACK TRAJECTORIES

4.1 METHODOLOGY

THE EFFECT OF SYNOPTIC FLOW DIRECTION Among the various processes that contribute to Arctic-mean warming, the North Atlantic sector of the Arctic is strikingly sensitive to changes in the atmospheric circulation. Particularly during winter, the comparably warm SST of the North Atlantic Ocean bounds the atmosphere at the surface, enabling moisture and energy fluxes from the ocean to the atmosphere. The resulting atmospheric structure is hence different from the one further north towards the central Arctic, where snow and ice surfaces prevail. As a result, at mid-tropospheric levels, a cold and dry Arctic air mass occupies the Central Arctic region. This air mass is normally well separated from the comparably warm and moist air masses at lower latitudes by strong westerly circumpolar winds. The terms Polar Jet Stream and Polar Vortex correspond to the climatological abundance of these winds in the troposphere and stratosphere, respectively. Meridional exchange is however increased in episodes of a weak, meandering jet stream, with strongest impacts for the (surface) meteorology during the winter time, when the differing solar heating rates lead to largest contrasts between the characteristics of polar and mid-latitude air masses. It has been shown that injections of moist and warm air into the Atlantic sector of the Arctic, that are often associated with cyclonic activity, can lead to substantial warming of the near-surface atmosphere during winter (Woods et al., 2013; Woods and Caballero, 2016; Moore, 2016). By analysing the daily near surface temperature tendency across the Arctic, Serreze et al. (2011) identified temperature differences of the order of 10 K between northerly and southerly flow conditions in the North Atlantic Arctic region during winter. Figure 4.1 evidences that these relations are also apparent in the Ny-Ålesund homogenized radiosonde record at mid tropospheric levels. Throughout the course of the year, 850–800 hPa temperatures at the site are warmer during southerly wind episodes than during northerly wind episodes. This difference is most distinctively developed during the winter months ($\Delta T \approx 8\,\mathrm{K}$). Note that the corresponding circulation patterns for northerly or southerly flow will be presented in the following Sections. On the other hand, westerly/easterly conditions have no clear effect on the averaged temperature. Utilizing Era-Interim reanalysis data for locations of prominent Arctic research stations, where ongoing observations promise sufficient assimilation quality, I tried to reproduce the findings for strong temperature dependency on

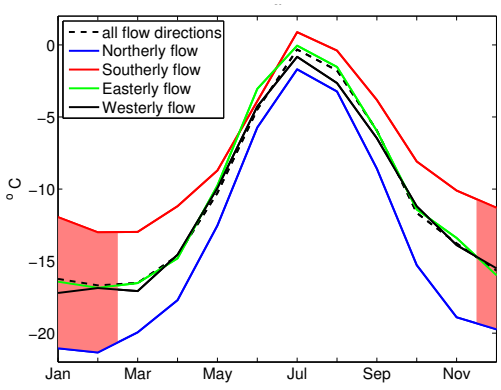

(a)

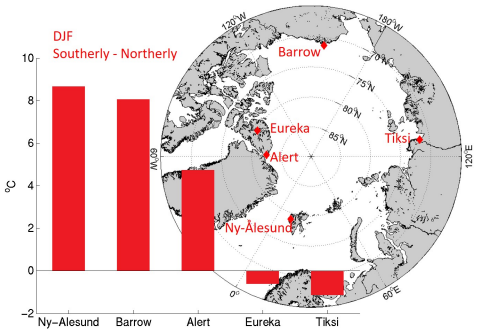

(b)

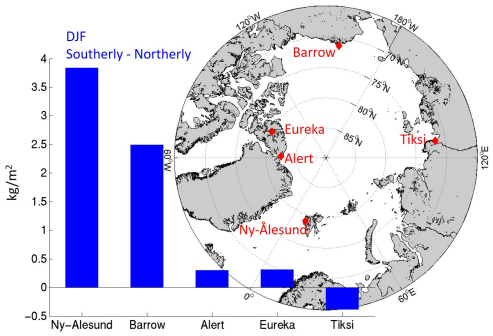

(c)

Figure 4.1: **(a):** Ny-Ålesund 800–850 hPa averaged temperatures for different background flow conditions during 1993–2016. The four cardinal wind directions are defined as exact ± 45° and at least 75% of the winds in the layer need to be within that range. **(b):** S-N differences in 800–850 hPa mean temperature at five Arctic locations from Era-Interim. **(c):** As (b), but for the vertically integrated water vapor content from Era-Interim (IWV, integrated up to 200 hPa)

the air flow direction in other vicinities of the Arctic (4.1 (b)). These include the sites Alert (82.5°N, 62.3°W), Eureka (80.0°N, 86.0°W), Barrow (71.3°N, 156.6°W) and Tiksi (71.6°N, 128.9°E). It can be seen that Ny-Ålesund is quite unique in terms of the role of the air flow, as S-N

differences at the other locations are much weaker. Only Barrow in North Alaska shows anomalies of a comparable magnitude; for Eureka and Tiksi the sign of the temperature anomalies is even reversed. The same qualitative results are revealed when applying the analysis to the integrated water vapor content (IWV, Figure 4.1 (c)), a clear indication for the profound role of advecting warm, moist, maritime air masses from the North Atlantic during winter. Yeo et al. (2018) consistently demonstrated for the case of Ny-Ålesund, that in winter an enhanced fraction of low-level clouds is associated with southerly flow conditions.

It is hence interesting to investigate the contribution of circulation changes for the strong recent warming observed in the region, and whether they project differently on different seasons of the year. Regarding the region of Svalbard and Ny-Ålesund in particular, Maturilli and Kayser (2017) have demonstrated based on radiosonde measurements, that there is a trend towards more frequent southerly flow conditions during winter in recent decades. In this chapter I apply an air back-trajectory analysis to link the lower-tropospheric temperature field to circulation patterns and air mass characteristics, and assess the amount of warming that these circulation changes may contribute to the overall observed warming in the region.

FROM TRAJECTORIES TO SOURCE REGIONS In order to allocate "source regions" to the air that reaches Ny-Ålesund, 6-hourly FLEXTRA air back-trajectories (see Chapter 2) are analyzed for Zeppelin mountain, roughly 2 km from the AWIPEV balloon launch platform. The trajectory end points were chosen at 1500 m height well above the mountain ridges to avoid the effects of topographic steering and boundary layer processes. Then, the air parcel was tracked back for three days, and the resulting location is referred to as "source region" of the air through the remainder of this chapter. I chose three days maily for two reasons. First, the actual trajectory path gets more uncertain the further back in time gets calculated (Stohl et al., 1995). Second, when investigating air mass characteristics from too far in the past, they may barely be representative for the air package that finally arrives in Ny-Ålesund. As introduced in Chapter 4.1, the analysis is based on the 1997–2016 period.

For a statistical analysis of the source regions, circular areas with a radius of 300 km are projected on a global 1° x 1° latitude x longitude grid. Then, the number of trajectories is counted, whose source regions fall within each circle. Division by the overall number of available trajectories for a certain season yields source region probability maps with the unit % per circle. Radii other than 300 km were also tested, but larger radii smeared out pecularities of the resulting maps, while for too small radii the number of "unoccupied" circles increased markedly. I conducted the analysis for all four seasons of the year individually,

but only for winter (DJF) and summer (JJA) conclusive results were found and are presented in the following sections.

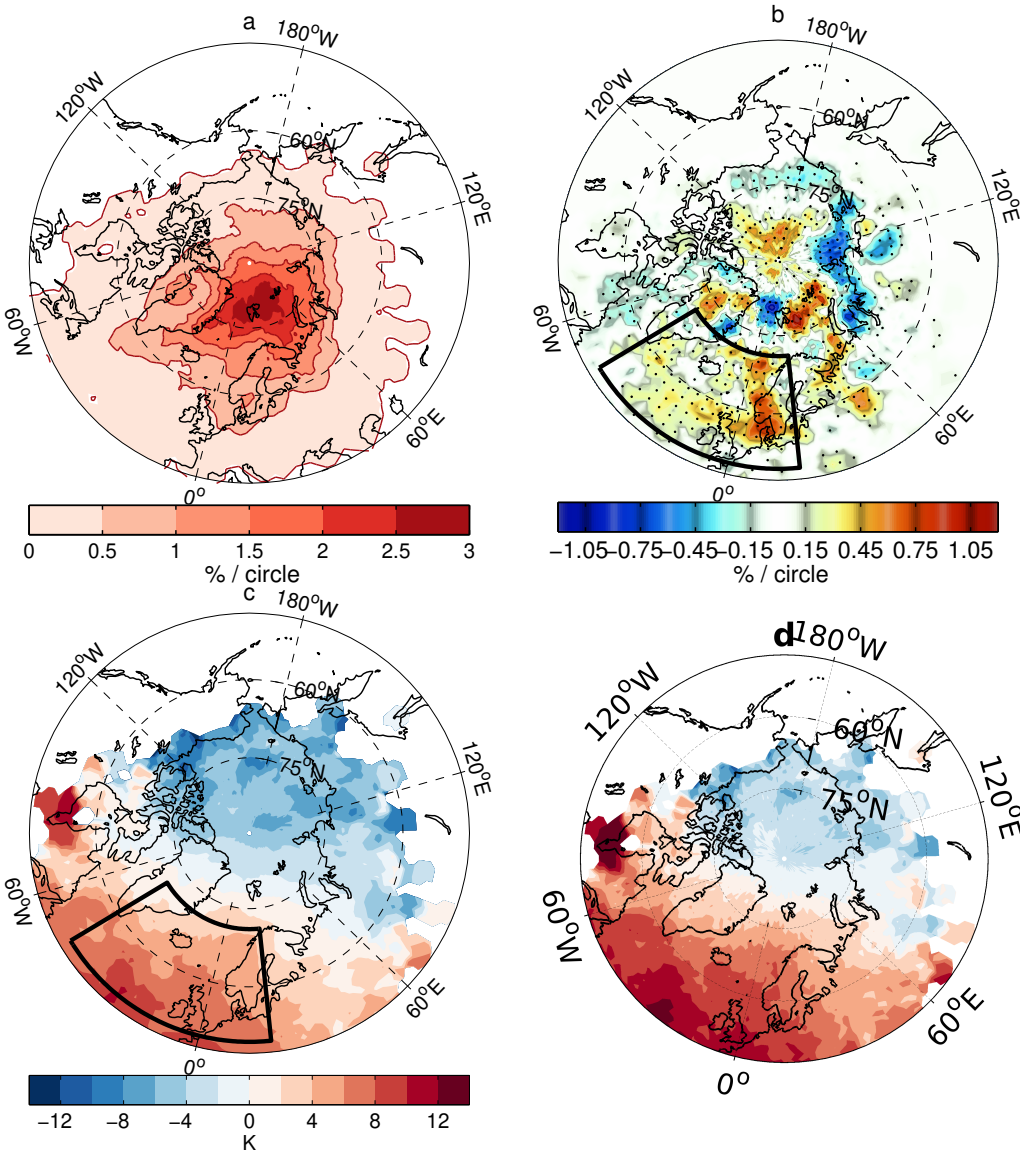

Figure 4.2: **(a):** Probability distribution map for source regions of Ny-Ålesund air at 1500 m height during DJF. **(b):** Change in probability expressed as difference P2 (Dec. 2006–Feb. 2016) minus P1 (Dec. 1996–Feb. 2006). Black dots indicate differences significantly different from zero (99%) and are only shown for changes exceeding ± 0.1% /circle (see text for details), **(c):** Ny-Ålesund temperature anomaly at 1500 m height as a function of source region during DJF, **(d):** Ny-Ålesund station-based SAT anomaly as a function of trajectory source region during DJF.

4.2 WINTER

4.2.1 *Source Regions of Ny-Ålesund Air*

Figure 4.2 sums up the main results of the source region analysis for all 6-hourly trajectories during the 1996–2016 winters (DJF). The source region probability map (Figure 4.2 (a)) suggests that in most cases, Ny-Ålesund air has actually originated in the Svalbard region itself, or has spent the last days prior to its arrival in that region. This is indicated by the highest probabilties of $\approx$ 3% per circle around Svalbard, with a rather smooth decline with increasing distance from the archipelago. It is however noteworthy that there is a non-zero chance that air has originated in very distant places, such as the midlatitude North Atlantic.
In a next step, I investigated temporal changes in the source region distribution over the analysed period. Therefore, the dataset was split into two sub periods of equal length, resulting in an erlier period P1 (Dec.1996–Feb.2006) and a more recent period P2 (Dec.2006–Feb.2016). Note that these subperiods have the same nomenclature as the ones in the previous Chapter 3.3, but they here correspond to different years. The P2 - P1 difference is presented in Figure 4.2 (b). Statistical significance of these differences was assessed using a Monte Carlo approach, where two subperiods P_{G1} and P_{G2} were randomly resampled from the available pool of years. This procedure was repeated 10000 times and the resulting average source region map was compared to the original decomposition in P1 and P2. The most striking feature to observe is that there is a broad region of enhanced source region occurence spanning the subpolar North Atlantic and Scandinavia during P2. At the same time, negative anomalies of source region probability appear over the coastal region of northern Siberia, implying that in recent years, Ny-Ålesund has received air from that region less frequently. To describe the former region of enhanced probabilities, I define the "Atlantic Box" (ATL Box, see Figure 4.2 (b), (c)), spanning from 50°N to 71°N, 45°W to 20°E, respectively. The ATL Box has been source region to Ny-Ålesund air in 16% (21%) of cases during P1 (P2) respectively, representing a relative increase of about 31%. This increase is particularly interesting, since the entire ATL region is associated with above average temperatures in Ny-Ålesund. This is shown in Figure 4.2 (c), where Ny-Ålesund temperature is plotted as a function of source region of the air. It can be seen that air masses originating in the sub-Arctic source regions in the Atlantic sector lead to above-average temperatures in Ny-Ålesund, while source regions in the Central Arctic lead to anomalously cold temperatures. Ny-Ålesund temperatures are on average 5.5 K warmer when the air has originated in the ATL box, compared to all other source regions, which clearly reflects the processes outlined in the beginning of this chapter. Figure

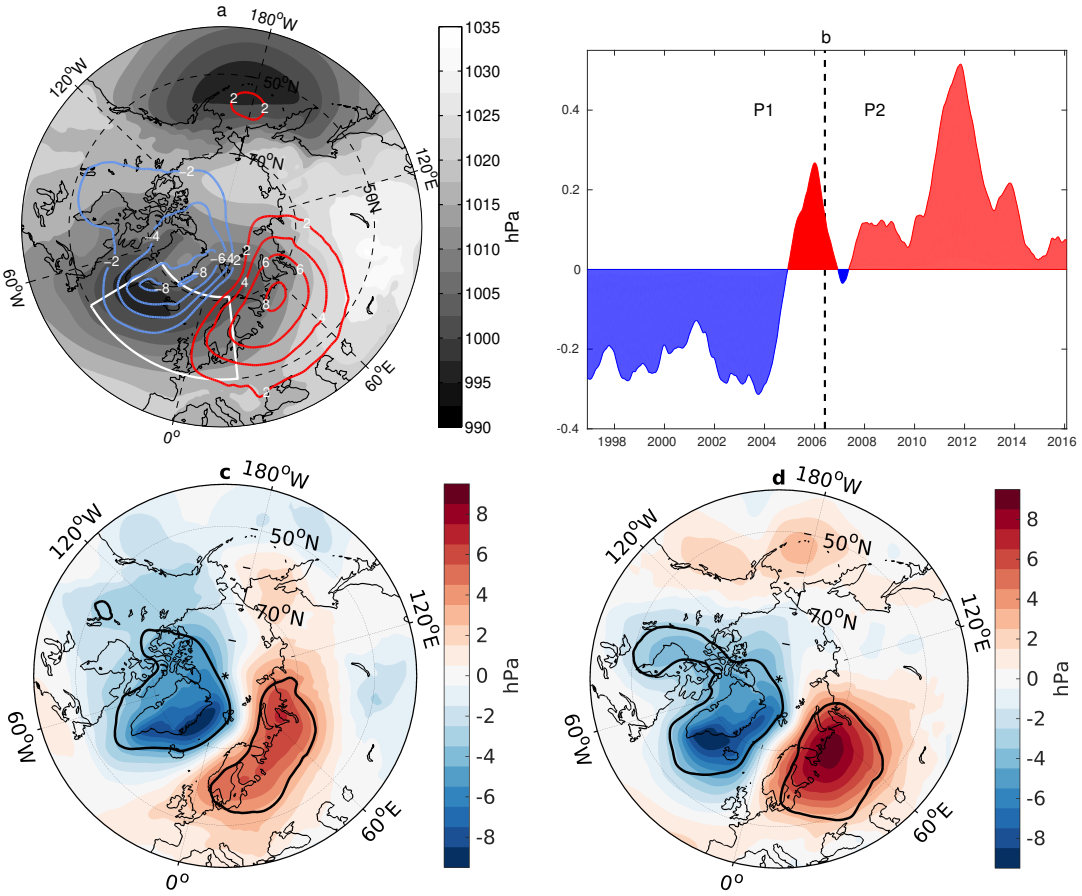

Figure 4.3: **(a):** 1996–2016 climatological DJF SLP (gray shading) and 1996–2016 SLP composite for ATL Box trajectories arriving in Ny-Ålesund (hPa, color contours). **(b):** Normalized time series of the DJF SLP composite pattern shown in (a), with a three-year low pass filter applied (see text and Section A.1 for details). **(c):** The anomalous (with respect to the mean over 1996–2016) SLP pattern for ATL box days during P1 only. Statistical significant anomalies (99%, see text and Section A.1 for details) are enclosed by black contours. **(d):** Same as (c), but for ATL box days during P2 only.

4.2 (d) further indicates that these findings for the temperature filed at 1500 m height are also valid for the surface temperature.

4.2.2 *Circulation changes*

In a next step, it is investigated which circulation changes have driven the change in source regions that is evendent in Figure 4.2 (b). Therefore, I consult the 6-hourly SLP field from the Era-Interim reanalysis. Regarding all trajectories that originated in the ATL Box, a composite SLP field was calculated for ATL days, with respect to the climatological SLP over the whole time. A deteiled description on the calculation is provided in Chapter A.1. Both climatology and composite SLP are

pesented in Figure 4.3 (a). Regarding the former, prominent features that normally govern the winter time northern hemisphere can be identified, such as the Icelandic and Aleutian lows and the Siberian high. The pattern of the ATL SLP composite stands out as a well defined dipole pattern with maximum values of about 8 hPa for each centre of action. Anomalously low pressure governs Greenland and the North Atlantic, hence projecting on an intensified Icelandic low. At the same time, anomalously high pressure is evident over Scandinavia and north-western Russia, representing the so called Ural blocking, which has already received attention in recent discussions on implications of Arctic warming and Barents/Kara sea ice loss (Luo et al., 2016; Crasemann et al., 2017; Gong and Luo, 2017). It should be noted that the entire presented composite pattern is significantly different from zero at the 99% confidence level, according to a two-sided Student's t-test (see Chapter A.1 for details).

In terms of anomalous geostrophic flow, the dipole pattern promotes very effective "pumping" of lower-latitude air towards the Svalbard region, consistent with the enhanced occurrence of source regions over the Atlantic in P2, as well as with the reduced occurrence of air approaching from Siberia (Figure 4.2). Yeo et al. (2018) found that a comparable circulation pattern is associated with the enhanced occurrence of low level clouds in Ny-Ålesund, consistent with the association to positive temperature anomalies in the lower troposphere and at the surface.

To investigate the temporal evolution of the SLP composite pattern over the analysis period, I calculated an index describing its state, which is presented in Figure 4.3 (b). A detailed description on how the index is retrieved can be found in the Appendix (Section A.1). It may be interpreted as proxy for how "well developed" the SLP composite pattern shown in Figure 4.3 (a) was at a certain time, accounting for both amplitude and spatial expression of the pattern. During episodes of prevailing positive (negative) index values, the pattern is particularly strongly (weakly) developed. The index reveals interannual and a marked decadal variabilty in the ATL pattern. Most strikingly, while the index has been mainly in its negative phase during P1, a strong upward trend through the winters 2004/05–2011/12 guided the index towards a regime of predominantly positive values during P2. The hence amplified SLP pattern during P2 is consistent with enhanced meridional transport of air masses from the ATL box, carrying comparably warm and moist air towards Svalbard. To allow a more direct physical interpretation of the strengthening of the SLP dipole over time, which is communicated by the sharp increase in the index from P1 to P2, the SLP composite pattern was calculated for both time periods individually. The resulting patterns are shown in Figure 4.3 (c) and (d). As expected, air mass advection from the ATL box is associated with a corresponding dipole pattern in both P1 and P2. However, during

P2, the anomalous high pressure east of Scandinavia is much stronger developed, and the center of its maximum has shifted towards the west compared to P1, while the center of the anomalous low pressure pole has shifted towards the southeast of Greenland. For P2, this introduces a much stronger anomalous zonal pressure gradient along 70°N over the North Atlantic when compared to P1, which is consistent with an increase in advection from the south towards Svalbard. The stronger expression of this so called "Scandinavian Pattern" in the more recent period is consistent with Crasemann et al. (2017), who linked the strengthening to sea ice loss in the Barents/Kara Seas.

4.2.3 *Quantification of Advective Warming*

The above analysis evidences that the recent unprecedented winter warming in the Svalbard region is indeed accompanied by a marked shift in the large scale circulation patterns over the North Atlantic. In this section I attempt to quantify the amount of warming that can be attributed solely to the enhanced occurrence of air flow from the ATL box in P2 compared to P1. Therefore, I calculated the difference between the actual mean temperature and the hypothetical mean temperature that would arise if all other than ATL box days were systematically neglected. This procedure is applied at every grid point using the Era-Interim 850 hPa temperature field, and for P1 and P2 individually. The P2 - P1 difference in that value may be referred to as the "warming footprint of the ATL box" (cf. Dahlke and Maturilli, 2017):

$$\begin{aligned}(\bar{T}_{P2} - \bar{T}_{\neg ATL,P2}) - (\bar{T}_{P1} - \bar{T}_{\neg ATL,P1}) = \\ \frac{n_2}{N_2}\left(\Delta\bar{T}_{ATL} - \Delta\bar{T}_{\neg ATL}\right) + \left(\frac{n_2}{N_2} - \frac{n_1}{N_1}\right)\left(\bar{T}_{ATL,P1} - \bar{T}_{\neg ATL,P1}\right)\end{aligned} \tag{4.1}$$

where

$n_{1/2}$	number of ATL box days in $P1/2$
$N_{1/2}$	number of days in $P1/2$
Δ	$P2 - P1$ difference
$\bar{T}$	mean temperature
$\bar{T}_{ATL}$	mean temperature during ATL box days only
$\bar{T}_{\neg ATL}$	mean temperature during all but ATL box days

A detailed derivation of equation (4.1) is provided in section A.3. The first term on the right hand side corresponds to different warming signals between days with trajectories from the ATL box and days with trajectories from all other regions. The second term one the right hand side finally represents the warming effect of more frequent advection

from the ATL box, and is plotted in Figure 4.4 (b). The footprint appears as a patch of warm anomalies of up to 0.45 K amplitude centered over Svalbard. It is noteworthy that the pattern of warming associated with enhanced air advection from the Atlantic region bears resemblance to the overall pattern of Arctic wide warming at the same height level (see Figure 4.4 (a)), given the pronounced warming features in the North Atlantic sector of the Arctic, with Svalbard located in the key region. On the other hand, the widespread, but mostly insignificant winter warming in other parts of the Arctic, such as Siberia and Northern

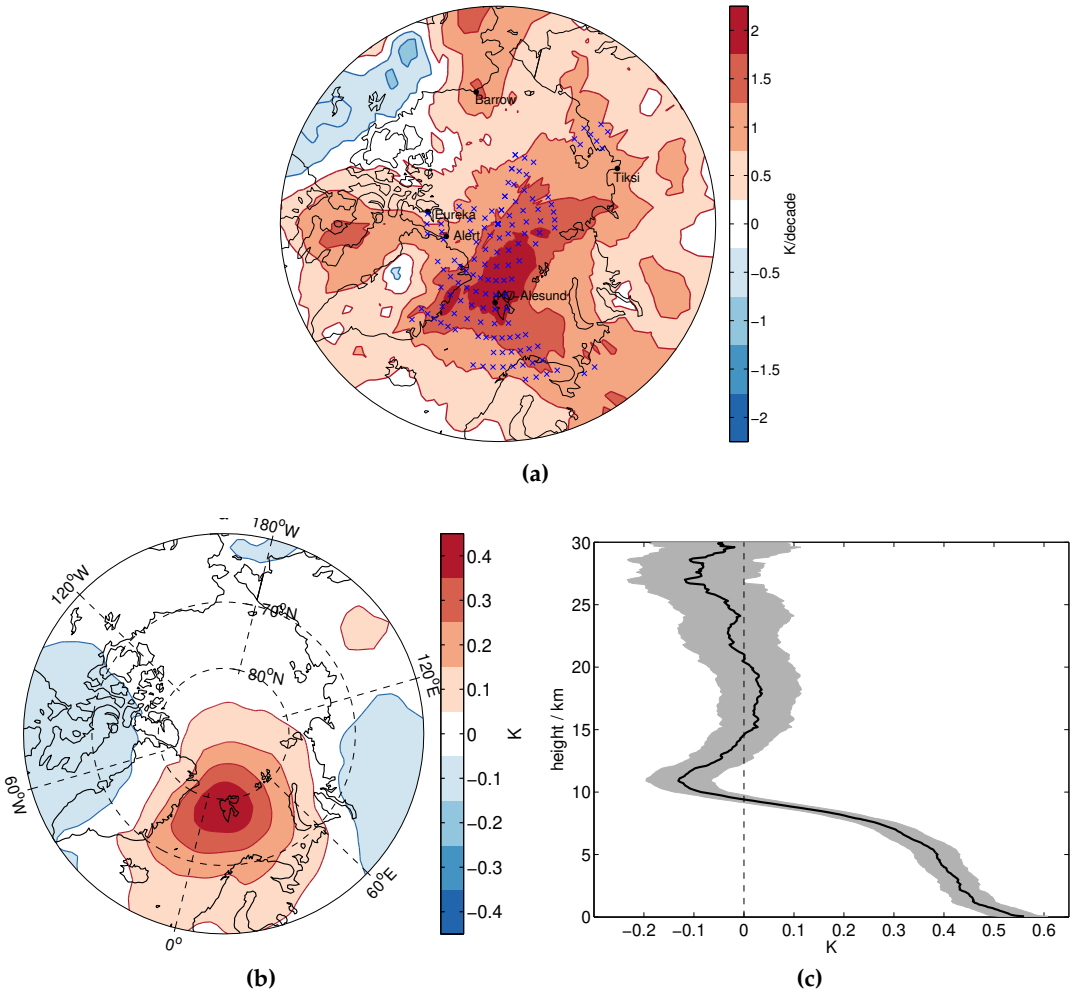

Figure 4.4: **(a):** 1996–2016 DJF warming trend at 850 hPa from Era-Interim. Crosses indicate significance at the 95% level. **(b):** Difference in DJF 850 hPa temperature between an average day when an ATL-box trajectory reached Ny-Ålesund and an average day for all other trajectories, multiplied by the increase in fraction of ATL-box days from P1 to P2 (second term on the right in equation (4.1)) from ERA-Interim. **(c):** The same analysis as (b), but as a vertical plot based on temperatures from the Ny-Ålesund long-term radiosonde record. Grey shading indicates the 95% confidence level

Canada (see Figure 4.4 (a)) does not seem to be connected to these circulation changes. Moreover, the amplitude (0.45 K) of the ATL box warming footprint represents only about a quarter of the observed warming in that region ($\approx$ 2 K, see Figure 4.4 (a)), pointing towards the importance of other processes and feedbacks at presence.
In order to analyse the vertical structure of the ATL box warming footprint, I additionally evaluated the second term on the right in equation (4.1) in the Ny-Ålesund homogenized radiosonde record (Figure 4.4 (c)). It can be seen that the radiosonde data agree well in the amplitude of the Era-Interim ATL warming footprint in the lower troposphere. Furthermore they evidence strongest warming at the surface (up to 0.6 K) which decays with altitude. The apparent cooling at tropopause levels ($\approx$ 11 km) may be interpreted such that during ATL-box days, the tropopause level is lifted because of the generally warmer atmospheric column. As a consequence, the weaker lapse rate of the stratosphere is then replaced by the stronger negative lapse rate of the troposphere, resulting in a weak cooling in that altitude range. However, the ATL box warming footprint in the radiosondes reveals significant warming contributions throughout the troposphere up to $\approx$ 7 km height. This finding is consistent with the concept of bottom-amplified Arctic warming (Serreze et al., 2009) and may serve as another piece of evidence that atmospheric advection can yield surface amplified warming, as proposed by Woods and Caballero (2016).

4.3 SUMMER

Arctic warming is recognized most strikingly during the winter season, as most of the involved feedback mechanisms that act to provide additional heat to the atmosphere are most effective in winter (Pithan and Mauritsen, 2014). Still, weaker but significant warming is found in both reanalysis and station data for the Atlantic Sector of the Arctic, as indicated by Figure 1.2. The atmospheric summer circulation, particularly the summer Northern Annular Mode (NAM), has been recognized as driver of temperature variability in the Arctic (Serreze and Barrett, 2008). Hence, the analysis of the previous paragraphs has been repeated for the summer season, and key results are presented in the following.

4.3.1 *Source Regions of Ny-Ålesund Air*

Figure 4.5 provides an overview of Ny-Ålesund air mass source regions during the summer months (JJA). As for the winter months, the Svalbard region itself is the most frequent source region, with reduced occurrence frequency of air from more distant regions (Fig. 4.5 (a)). Another feature that is shared between both summer and

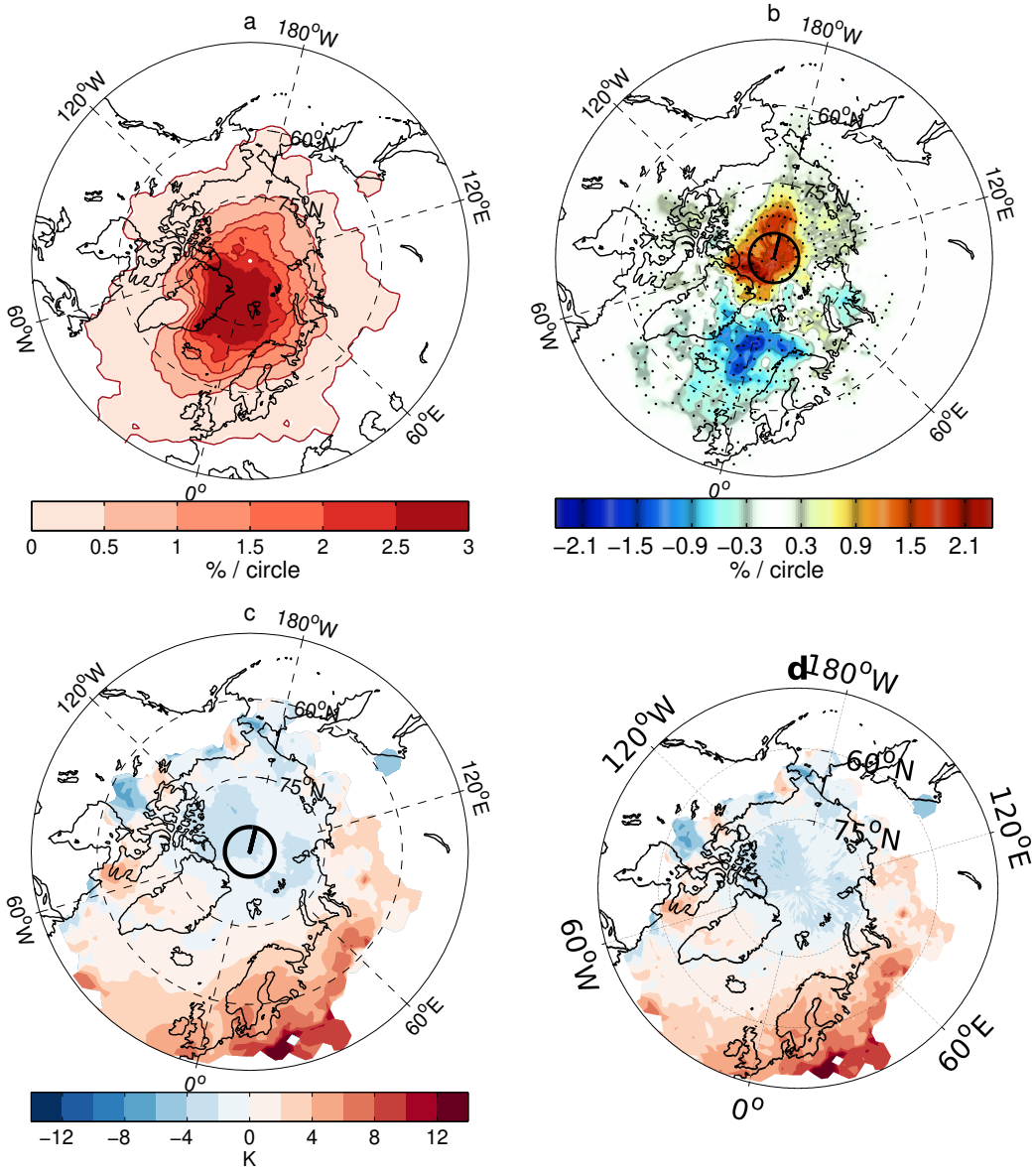

Figure 4.5: As Figure 4.2, but for the summer: **(a):** Probability distribution map for source regions of Ny-Ålesund air at 1500 m height during JJA. **(b):** Change in probability expressed as difference P2 (Jun. 2007–Aug. 2016) minus P1 (Jun. 1997–Aug. 2006). Black dots indicate differences significantly different from zero (99%) and are only shown for changes exceeding ± 0.1% /circle (see text for details), **(c):** Ny-Ålesund temperature anomaly at 1500 m height as a function of source region during JJA, **(d):** Ny-Ålesund satation-based SAT anomaly as a function of trajectory source region during JJA.

winter season is the tendency of colder temperatures in Ny-Ålesund when the air masses orgin in the central Arctic, and the tendency for anomalously warm temperatures in Ny-Ålesund for air masses approaching from the lower latitude Atlantic (Figure 4.5 (c) and (d)).

However, the magnitude of these temperature anomalies is somewhat weaker during summer than during winter, owing to the generally stronger hemispheric merdidional temperture gradients in winter. The P2 (Jun. 2007–Aug. 2016) minus P1 (Jun. 1997–Aug. 2006) difference reveals interesting large scale features, and is shown in Figure 4.6 (b). Air masses approaching Ny-Ålesund from the central Arctic occur significantly more often in P2 compared to P1. This happens at the cost of the occurrence frequency of air masses originating over the broader North Atlantic ocean, from where Ny-Ålesund experiences reduced impact during P2. These changes are in sharp contrast to those found for the winter season (Figure 4.2 (b)), where a decrease with time was found for air originating in the Central Arctic, paralleled by an increase in air approaching from the North Atlantic.

4.3.2 *Circulation changes*

It is straight forward that an increased meridionalization of the atmospheric flow, that is - more northerlies over the Fram Strait- must have been responsible for the characteristic north-south shift in the air mass source region distribution. I defined a "Central Arctic" Box (CA box, see circle in Figure 4.6), which is the area north of 85°N, well representative for the region of enhanced source region occurrence during P2. Figure 4.6 (a) shows the anomalous SLP composite field for days when the CA box has been source region to Ny-Ålesund air. The pattern consists of anomalous high pressure over Greenland and parts of the Candadian Arctic, as well as a smaller region of low pressure centered over Novaya Zemlya. Besides being geostrophically consistent with a northerly wind component pointing towards Svalbard from the central Arctic, the pattern projects onto a negative phase of the summer NAM, given the high pressure over Greenland. In Figure 4.6 (b), the temporal evolution of the composite SLP pattern is presented. The reader is referred to Section A.1 for a description of the index. It reveals a marked postive trend, corresponding to a strengthening of the SLP pattern over time, guiding it from predominantly weak expressions (negative values) in P1 to predominantly strong expressions (positive values) in P2. Interestingly, the years with the most rapid change in the summer index (2004–2012) are equivalent to the period of most rapid change in the winter index (see Figure 4.3 (b)), which could be an indication for an external driver that impacts the circulation across seasons, for instance ocean variability. The comparison of Figures 4.6 (c) and (d) illustrates the meaning of the shift in time in the summer index. The most prominent difference between P1 and P2 is the strengthening and northward shift of the high pressure anomaly over Greenland, which during P2 extends well over the Beaufort Sea. The strengthened and northward shifted Greenland high is geostrophically consistent with reduced air inflow towards Svalbard from subpolar

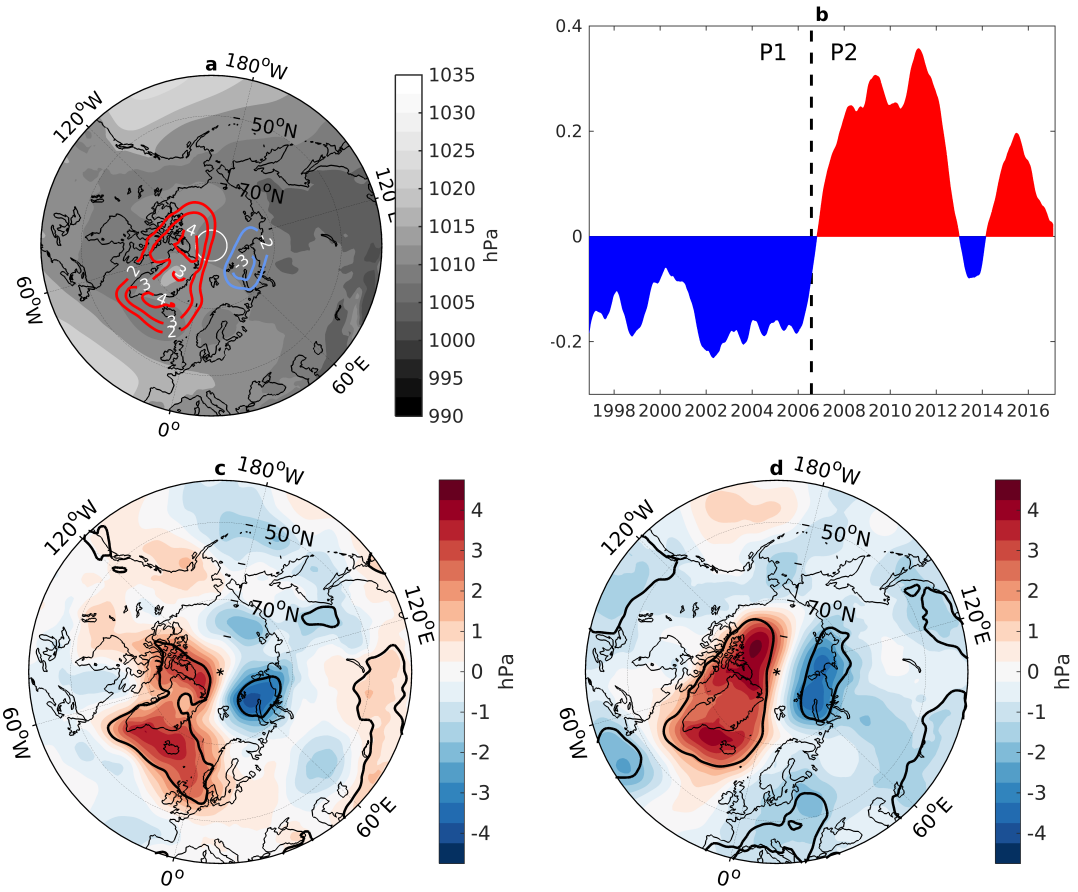

Figure 4.6: As Figure 4.3, but for the summer: **(a):** 1997–2016 climatological JJA SLP (gray shading) and 1997–2016 SLP composite for CA Box trajectories arriving in Ny-Ålesund (hPa, color contours). **(b):** Normalized time series of the JJA SLP composite pattern shown in (a), with a three-year low pass filter applied (see text and Section A.1 for details). **(c):** The anomalous (with respect to the mean over 1997–2016) SLP pattern for CA box days during only P1. Statistical significant composite values (99%, see text and Section A.1 for details) are enclosed by black contours. **(d):** Same as (c), but for CA box days during only P2.

regions and increased inflow from the Central Arctic, as evident from the air mass source region analysis in Figure 4.2 (b). In fact, the recent shift of the summer circulation in the Arctic towards an intensified Greenland high has received attention, and has been linked to the "Greenland blocking" pattern, (e. g.Overland et al., 2012; Hanna et al., 2018b). My results clearly show that the state of this circulation strongly determines air mass advection pathways towards Svalbard.

4.3.3 *Quantification of advective cooling*

The above results suggest that the depicted large scale circulation changes in the 1997–2016 summer period have - in contradiction to the winter season - contributed negatively to the overarching warming in the Svalbard region. Indeed, while summer surface temperature trends from Svalbard stations generally yield weak but significant warming

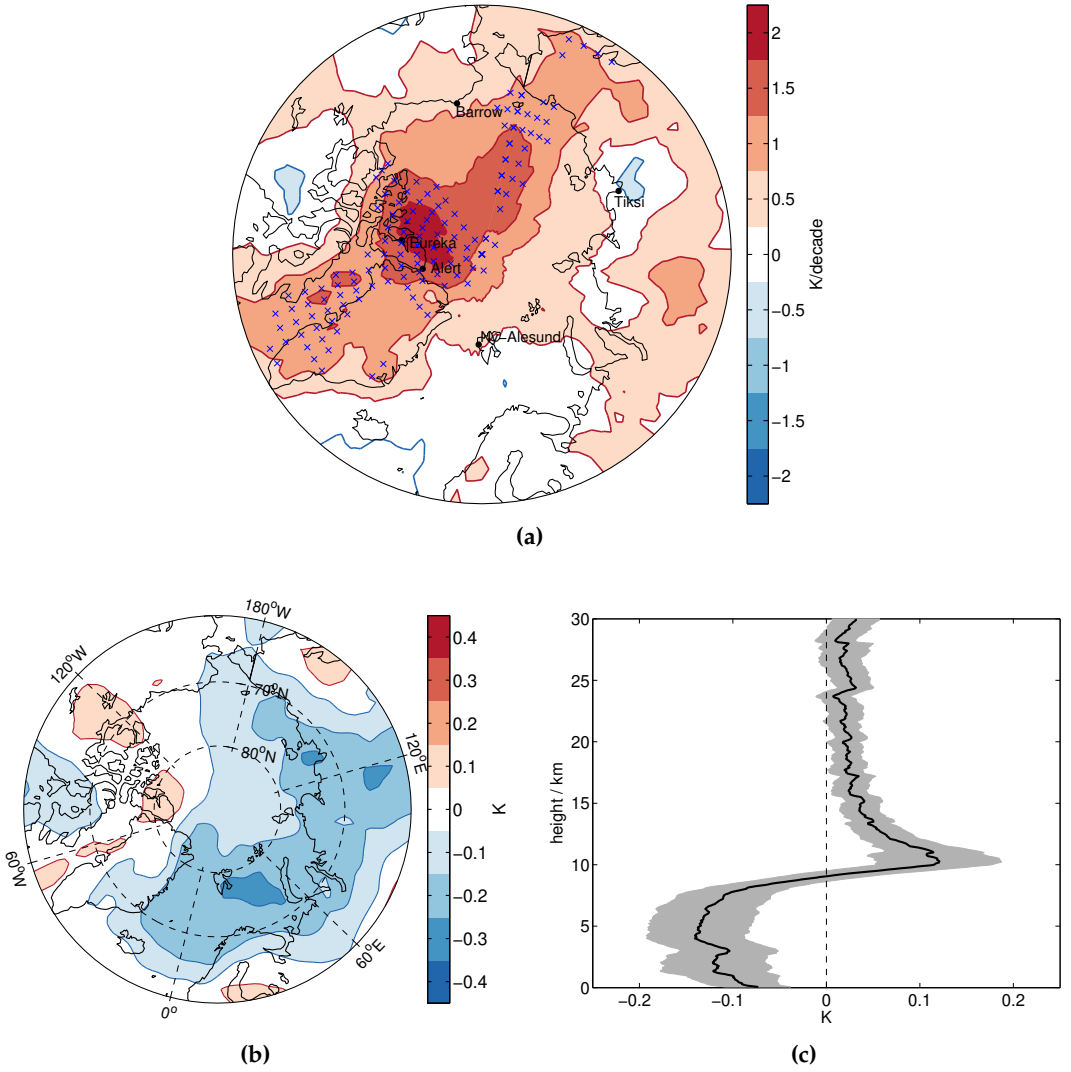

Figure 4.7: As Figure 4.4, but for the summer: **(a) :** 1997–2016 JJA warming trend at 850 hPa from Era-Interim. Crosses indicate significant (95%) trends. **(b):** Difference in JJA 850 hPa temperature between an average day when an CA-box trajectory reached Ny-Ålesund and an average day for all other trajectories, multiplied by the increase in fraction of CA-box days from P1 to P2 (second term on the right in (4.1)) from ERA-Interim.**(c) :** The same analysis as (a), but as a vertical plot based on temperatures from the Ny-Ålesund long-term radiosonde record. Grey shading indicates the 95% confidence level

(see Figure 3.5), Figure 4.7 (a) implies that the temperature field at 850 hPa around Svalbard has - at least during 1997–2016 - experienced neither significant warming nor cooling. Rather, significant warming is evident between Northern Greenland/Canada and the North pole. By quantifying the contribution to temperature changes accounted for by CA days, I do not aim for explaining the warming north of Greenland, but rather the lack of warming in the Svalbard region during summer. This is because the design of my analysis, namely the decomposition in CA days and non-CA days, refers inherently to the location of Ny-Ålesund. Nevertheless it is obvious that large-scale circulation changes with implications for Ny-Ålesund may as well have effects in other vicinities of the Arctic. Analogous to equation 4.1 for the ATL box and winter, Figure 4.7 (b) and (c) show the temperature change footprint due to increased occurrence frequency of air from the CA box during summer. Weak but widespread cooling of up to 0.3 K covers the North Atlantic, the Barents Sea, and northern Siberia. These findings are consistent with the previous notations regarding the effects of the CA region. The vertical structure of the temperature footprint is much weaker and inverted when compared to the winter analysis. Cooling prevails below 7 km and a tight warming region appears around 10 km height, suggestive for a shallower tropopause during CA days. Additional to the enhanced advection of comparably cold air masses from the north towards Svalbard, the role of Central Arctic cyclones during summer may be challenged as well, since these are associated with turbulent fluxes. As was shown by Serreze and Barrett (2008), there is a pronounced maximum of cyclones in the central Arctic during summer, located just in the CA region. These cyclones would potentially be steered towards Svalbard more effectively by the SLP composite pattern in Figure 4.6 (a), thereby modulating clouds and the associated radiative effects. In the summer season, solar irradiance plays an important role in driving surface temperatures. Since cyclones then are typically associated with cloudy conditions and hence larger reflectance of solar radiation back to space, letting more cyclones act on Ny-Ålesund during summer would result in additional radiative cooling, consistent with Figure 4.7 (b). Likewise, anticyclonic conditions during summer generally lead to clear sky conditions, resulting in surface warming.

4.3.4 *Observational Case Study: May/June 2017*

In this section, the relevance of the above findings is illustrated by in situ measurements of the atmospheric column above Ny-Ålesund, that were collected in parallel to the shipborne campaign "Physical feedback of Arctic PBL, Sea ice, Cloud And AerosoL" (PASCAL). PASCAL took place in early summer 2017 in the pack ice approximately 400 km north of Svalbard, where the research ice breaker *Polarstern* was frozen

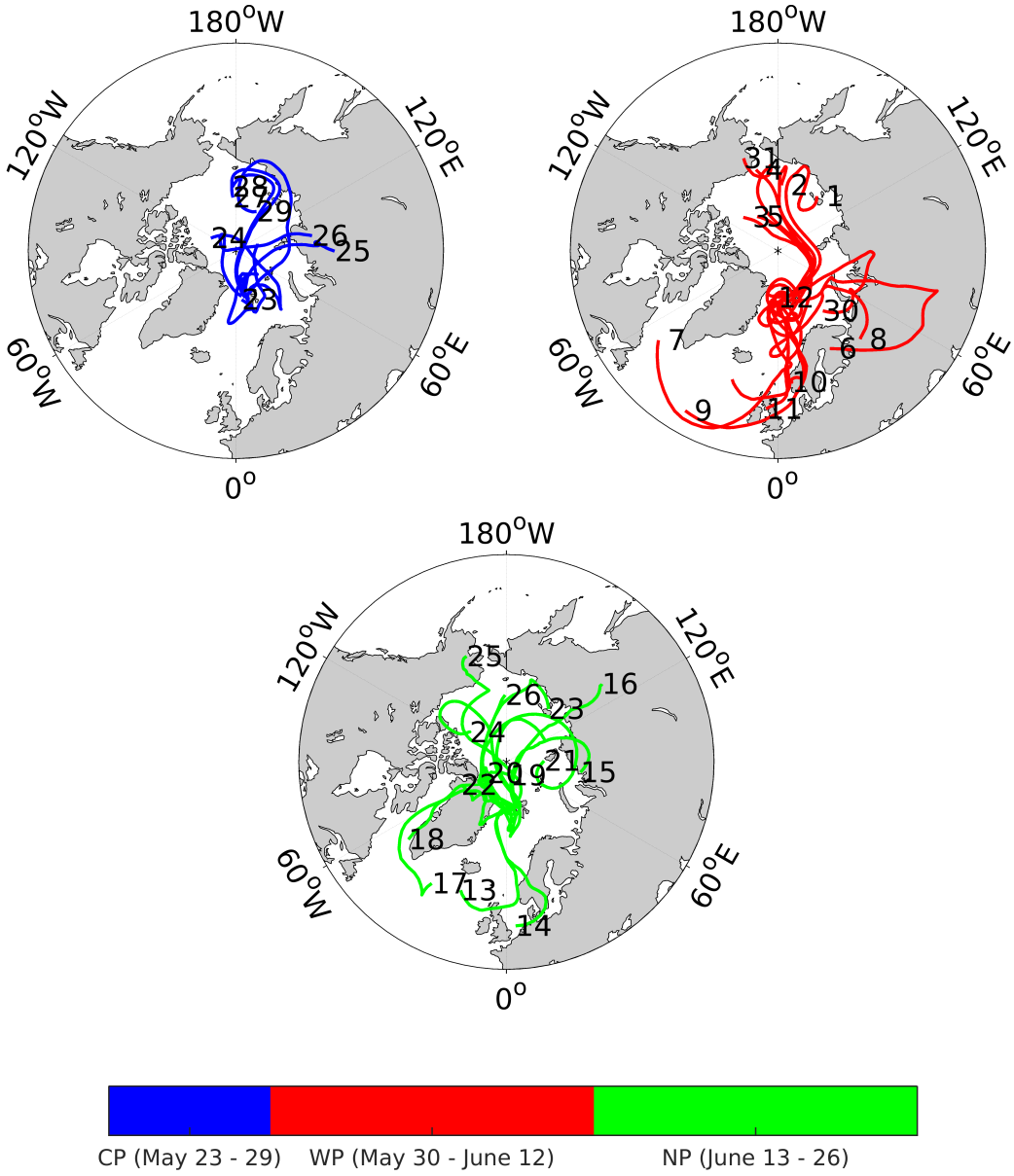

Figure 4.8: Ny-Ålesund 12 UTC, 7 day air back-trajectories at 850 hPa during May 23–June 26, 2017. According to Knudsen et al. (2018), the study period is subdivided into a cold period (CP, May 23–May 29), a warm period (WP, May 30–June 12), and a normal period (NP, June 13–June 26). Corresponding days of trajectory arrival in Ny-Ålesund are indicated at the trajetory start points, respectively. Figure after Knudsen et al. (2018), reproduced with FLEXTRA data.

to the ice. More information about the PASCAL campaign itself are given in Wendisch et al. (2018), and the synoptic background situation during the campaign is summarized in Knudsen et al. (2018). A main outcome of the Knudsen et al. (2018) paper was that the campaign

period could be characterized by a cold period (CP, May 23–May 29) in the beginning of the campaign, a warm period (WP, May 30–June 12) thereafter, and a normal period (NP, June 13–June 26) in the end of the campaign. These periods were characterized by corresponding signals in the temperature and humidity profiles, as retrieved from upper air soundings above the campaign site (warm and moist in WP, cold and dry in CP). At the same time in Ny-Ålesund, similar upper air soundings were taken every 6 hours, and the results were in good agreement with what was observed at *Polarstern*. Also, the transition between the three periods was shown to occur due to changes in the synoptic flow direction. Here, I use FLEXTRA trajectories to reproduce the pathways of the airmasses that reached Ny-Ålesund during the campaign period. Resulting trajectories are shown separately for each period in Figure 4.8. Trajectories during the 7 days of CP are colored blue in Figure 4.8. It can be seen that during that time, air was approaching Ny-Ålesund mostly from the north and northwest, with central Arctic source regions, and never originated in the lower latitude Atlantic region. In the beginning of WP (red trajectories), air was still approaching Ny-Ålesund from the north, but around the 6th of June, the trajectory pattern changes, indicating air mass origins south-east or south-west of Svalbard. These air masses have warmed by travelling significant distances over open water, before arriving in Ny-Ålesund. The situation during NP (green trajectories) is less clear. Some trajectories originated in the central Arctic, approaching Ny-Ålesund from the north east, thereby possibly experiencing adiabatic

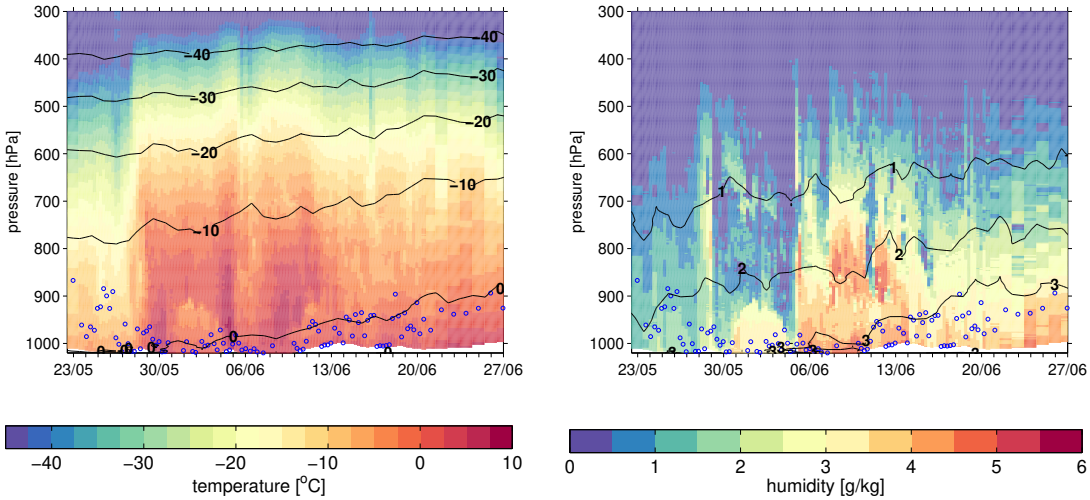

Figure 4.9: Vertical profiles of of temperature (left) and specific humidity (right) from Ny-Ålesund radiosondes. Isolines correspond to the 1993–2016 climatology, color coding indicates the 6-hourly soundings during May–June 2017. Blue circles indicate the PBL height, as computed from equation (1.11). Figure is taken from Knudsen et al. (2018).

warming when passing the Greenland ice shelf. Others originated in the sub-Arctic North Atlantic during NP.

The vertical profiles of temperature and specific humidity observed above Ny-Ålesund during the campaign period, as well as the climatologies, are shown in Figure 4.9. Specific humidity was calculated from the vapor pressure formulations by Hyland and Wexler (1983). The climatologies reveal the steady warming and moistening throughout the progression of early summer. At surface levels, temperature and specific humidity typically exceed the freezing point and $3\,\mathrm{gkg}^{-1}$ by the beginning of June, respectively. Throughout CP, i. e. before May 31, it is apparent that both tropospheric temperature and specific humidity were around or slightly below climatological values. This is consistent with the blue trajectories from Figure 4.8, that represent advection of cold and dry air over the ice edge from the north. At the same time, PBL heights were combarably large, reaching up to 950–870 hPa, as indicated in Figure 4.9. Throughout the entire WP, tropospheric temperatures were consistently enhanced, and specific humidity was enhanced between June 6–13. Also, PBL heigths were markedly reduced or even absent in that time, as indicated by the blue circles during WP. Changing synoptic flow conditions and larger wind speeds, as indicated by the longer trajectory paths when compared to CP, lead to the advection of warm and moist air masses from open water surfaces around Svalbard. This reduces stability as well as the radiative cooling efficiency of the near surface layers, drives more homogenous PBL conditions, and results in shallowing or vanishing of the PBL. During NP, i. e. after June 13, temperature, humidity and PBL height take "intermediate" values when compared to CP and NP. It is emphasized that the findings regarding PBL height also hold when expressing it in terms of geopotential height. Thus, during CP, WP and NP, the average PBL height was 514, 127 and 378 meters, respectively (not shown).

This case study serves as complementary investigation to the long-term trajectory study from Section 4.3. It provides observational evidence for the impact of the synoptic flow on temperature and humidity (and therefore potentially cloud) conditions around Svalbard. It may also be viewed as piece of evidence for the coupling of PBL characteristics to the synoptic flow. In section 4.3 it was revealed that in the recent summers compared to the late 1990s and early 2000s, large-scale circulation changes were responsible for an enhanced fraction or air masses reaching Ny-Ålesund from the central Arctic via anomalous northerly winds. This generally resembles conditions of the CP from the PASCAL campaign, and indicates that the "CP" synoptic phase also occurred more often in the recent decade. Since CP is associated with rather high reaching PBL's, it is suggested that these high reaching PBL's, and the associated vertical radiative and dynamical mechanisms have been particularly important in the recent summers as well.

4.4 DISCUSSION AND CONCLUSION

During the last two decades, the lower troposphere in the Svalbard region has been a hotspot of warming in the Arctic, particularly during winter. Depending on the synoptic flow, the region can be affected by either cold, dry air masses from the central Arctic, or by warm, moist, air masses from the lower latitude Atlantic ocean. As was shown by Yeo et al. (2018), this also affects the distribution of radiatively active low level clouds towards Svalbard. Combining radiosonde data, lagrangian air back trajectories and atmospheric reanalysis fields, I have demonstrated that changes in the large scale meridional circulation have occurred, which imply changes in properties of air masses reaching Ny-Ålesund. In winter, the region is supplied more frequently with air from the south, and less frequently with air from northern Siberia, resulting in a dynamical warming contribution for Svalbard that is of the order of about 25% of the oberved warming and with a bottom-amplified structure. The winter circulation changes include anomalous low pressure over Greenland and anomalous high pressure over Scandinavia and the Ural mountains, generating a southerly geostrophic wind component towards Svalbard. This pattern bears resemblance to the so called Barents Oscillation (Skeie, 2000; Chen et al., 2013), also entitled Arctic Dipole pattern (Wu et al., 2006) as the second dominant mode of variabilty of SLP in this domain of the Arctic. However, Chen et al. (2013) discussed whether the pattern could actually be an artefact of EOF analysis. My analysis may be viewed as new evidence that this mode is indeed physically existent, and its variability exerts a marked impact on temperature in the Svalbard region. In fact, the index minimum in the winters of 2004, and the maxima in 2006 and 2012 (see Figure 4.3 (b)) agree well with observed peaks in temperature and longwave downward radiation in Ny-Ålesund (Humlum et al., 2011; Maturilli et al., 2015). An interesting feature of the Ural blocking high is its association with sea ice reduction in the Barents/Kara Sea by enhancing the thermal downward radiation through the supply of warm moist air (Luo et al., 2016; Crasemann et al., 2017; Gong and Luo, 2017). Honda et al. (2009) further argue that this sea ice reduction can feed back onto a strengthening of the Ural blocking high via setting on a Rossby wave train, hence providing a positive feedback loop. As discussed in Jaiser et al. (2012) and Crasemann et al. (2017), the enhanced heat release in areas of excessive early winter sea ice loss, as seen in the Barents/Kara Seas, may reduce atmospheric static stability and hence promote enhanced baroclinic activity. This in turn can induce blocking situation in the vicinities of sea ice loss. Such a positive feedback loop would indeed help to explain the unprecedented recent warming in the Svalbard region and Barents/Kara Sea, however the causality in the atmosphere-sea ice interactions is still controversial (Sorokina et al., 2016).

Given that Barrow exhibits a comparable sensitivity of temperature and humidity to the synoptic flow direction [Figure 4.1 (b), (c)], I also conducted the trajectory study for Barrow (not shown). The results indicate that while also in Barrow, anomalously warm/cold temperatures are associated with source regions towards the south/north, no systematic trend pattern like the one for Ny-Ålesund is emerging between P1 and P2. This is consistent with Barrows weaker and insignifant temperature trend during winter [see Figure 4.4 (a)], and emphasizes the unique manner by which change is proceeding in the Atlantic domain of the Arctic. However, it should be noted that additional processes need to be considered as drivers of the warming that region, as Isaksen et al. (2016) find that background warming is present for all the major circulation patterns in the Svalbard region.

The results for the summer season are in sharp contrast to those for the winter season. The analysis of the change in air mass source regions reveals that in recent years, Ny-Ålesund is supplied more likely with colder air masses from the central Arctic, while it is less often affected by air from the lower latitude North Atlantic. This fairly distinctive characteristic is due to an increase of anticyclonic conditions over Greenland and the western half of the polar cap, and, to a lesser extent, cyclonic conditions over Novaya Zemlya. This circulation pattern is consitent with the negative phase of the summer NAM, and its recent downward trend (Ogi et al., 2016) and also project on the recently observed increase in the so called Greenland blocking pattern (Overland et al., 2012; Hanna et al., 2018b). The lower tropospheric temperature footprint of this circulation anomaly consists of a rather weak (max. 0.3 K) cooling contribution across the Barents/Kara Seas, Northern Siberia and including Svalbard. Hence, the recent shifts in the large scale circulation act to damp and mask the general warming over Svalbard during summer, while they tend to amplify Svalbard warming during winter. Moreover, the physical existence of "statistically dominant" modes of variability, such as the summer NAM and the Arctic Dipole mode, as well as their impact on local temperatures is evidenced, with the finding that Ny-Ålesund is a suitable place to monitor these processes.

There is debate about possible forcing mechanisms for the recent increase in the Greenland blocking, with explanations ranging from local warming over ice- and snow melt on the Greenland ice shelf to dynamical effects involving a weaker polar jet stream (Hanna et al., 2018a). Unfortunately, it has been reported that both regional and state of the art global climate models are not able to capture the increasing tendency of the associated summer Greenland blocking pattern (Hanna et al., 2018a; Rinke et al., 2019), which may have to be considered for the interpretation of future projections in the Svalbard region.

An interesting point that deserves follow up investigation is the role

of radiative control via cyclones in the Svalbard temperature development. Following the argumentation of Serreze and Barrett (2008), the North Atlantic cyclone maximum during winter, and the central Arctic cyclone maximum during summer correspond to the regions that supply Ny-Ålesund more frequently with air in recent winters/summers, potentially guiding more cyclones towards Svalbard, respectively. This is in agreement - at least for extreme cyclone events and individual winter months - with Rinke et al. (2017). However the effect of summer and winter cyclones must be separated. During polar night, solar radiation is absent and the main effect of Atlantic cyclones migrating towards the Arctic is warming, given that they carry warm, moist and cloudy air northward, hence introducing anomalous downward IR radiation. During summer, in contrast, cloudy (cloudfree) conditions associated with cyclonic (anticyclonic) systems would act to cool (warm) the surface by reflecting (transmitting) a fraction of the solar radiation.

5

CHANGING DRIVERS OF THE ARCTIC NEAR SURFACE TEMPERATURE BUDGET

In the previous chapters, the rapid changes in temperature, sea ice cover and atmospheric circulation of the last few decades have been demonstrated for the North Atlantic sector of the Arctic (Section 4), and for the Svalbard region in particular (Section 3). Both dynamical and thermodynamical processes in association with surface conditions are important and must be considered for explaining the observed changes. By consulting the individual terms of the diagnostic temperature equation (1.16) for the Era-Interim reanalysis data set at lower tropospheric levels, a systematical assessment of the involved processes is presented in this chapter. The analysis is done for winter (DJF) and summer (JJA) individually. First, the 1979–2016 averaged contributions of horizontal advection, vertical warming and diabatic heating to the 6-hourly temperature tendency are presented. In a next step, trends over 1979–2016 in the individual contributing terms are investigated. The results are meant to synthesize the findings of the previous chapters and to put them in an Arctic-wide context.
Recalling equation (1.16), the terms that contribute to the 6-hourly temperature tendency (TEND) read:

$$\underbrace{\frac{\partial T}{\partial t}}_{\text{TEND}} = \underbrace{-\mathbf{v}_h \cdot \nabla_h T}_{\text{ADV}} + \underbrace{\left(\frac{\kappa T}{p} - \frac{\partial T}{\partial p}\right)\omega}_{\text{VERT}} + \underbrace{\frac{J}{c_p}}_{\text{DIAB}} \tag{5.1}$$

Here, $\omega = dp/dt$ is the vertical velocity in pressure coordinates. Thus, positive values of ω correspond to sinking motions, while upward motions yield a negative value. ADV is the temperature change due to horizontal advection. This term is mostly sensitive to changes in the atmospheric circulation and the meridional temperature gradient. VERT is the sum of vertical temperature advection $\omega \cdot \partial T/\partial p$ and temperature change by vertical adiabatic motion, $\omega \cdot \kappa T/p$. Through the continuity equation (1.15), changes in vertical advection would be expected in regions where enhanced cyclonicity/anticyclonicity occurrs, while adiabatic processes are expected in the vicinity of marked topography. DIAB is the diabatic heating term, which corresponds to radiative fluxes and the energy exchanges via the phase transition of water. It is thus associated with latent heat release over open water areas, and does also reflect the integrated longwave radiative effect of water vapor, clouds and further absorbers/emitters in the atmosphere, as well as solar radiation during the bright seasons. All the terms have the unit Kday^{-1}. The diabatic term is not directly included in the reanalysis, and is hence computed as a residual with the other terms.

The analysis is conducted at the 925 hPa level, and vertical gradients are computed as centered differences between 900 and 950 hPa which are the nearest available vertical levels. Serreze et al. (2011) conducted a similar analysis based on the American National Centers for Atmospheric Prediction and National Center for Atmospheric Research (NCEP/NCAR) reanalysis product. In line with Serreze et al. (2011), I find that the 6-hourly temperature tendency (TEND) is at least an order of magnitude weaker than the contributions from the other terms, and is hence not discussed in the following.

5.1 WINTER

The climatological balances between ADV, DIAB and VERT during the winter (DJF) season are given in Figure 5.1. Green colors correspond to cooling contributions from the respective term, while brown colors correspond to a warming contribution to the averaged daily temperature tendency. In the top panel, the climatological SLP is additionally indicated by the grey isolines. Note the low pressure region over the North Atlantic Ocean, in association with the North Atlantic storm track as the pathway of cyclones. The patterns generally bear resemblance to those in Serreze et al. (2011). The most prominent feature is the occurrence of mean warm advection of the order of 1–3 $\mathrm{K\,day^{-1}}$ over the snow- and ice-covered regions of the Arctic oceans and Siberia. This warm advection is compensated for by diabatic cooling of roughly the same amplitude in those regions, consistent with cold surfaces, strong atmospheric stability, and little available water vapor and clouds. These relations are in sharp contrast to the regions of open water surfaces of the North Atlantic and North Pacific Oceans. These are characterized as regions of mean advective cooling, which is countered by an average warming through the diabatic term. This diabatic warming is closely related to the surface properties, as the northern border of the diabatic warming pattern mimics the climatological sea ice edge (see Figure 1.3 (a)). Open water surfaces are related to latent heat release, enhanced atmospheric water vapor content, cloudiness and the associated longwave downward radiation. Note in particular that a tongue of strong diabatic warming extends northward beyond 80°N along the west coast of Svalbard, resembling the warm SST footprint of the WSC.

Serreze et al. (2011) argue that the North Atlantic Arctic is a region of mean cold advection because it tends to lie on the western side of northward moving cyclones along the North Atlantic storm track, and is hence governed by mean southward winds. Indeed, the mean winter SLP field in Figure 5.1 (top panel) suggests that this may be true for the western half of the Atlantic sector (e. g. west of 10°E) and particularly between Greenland and Svalbard. There, SLP isolines are

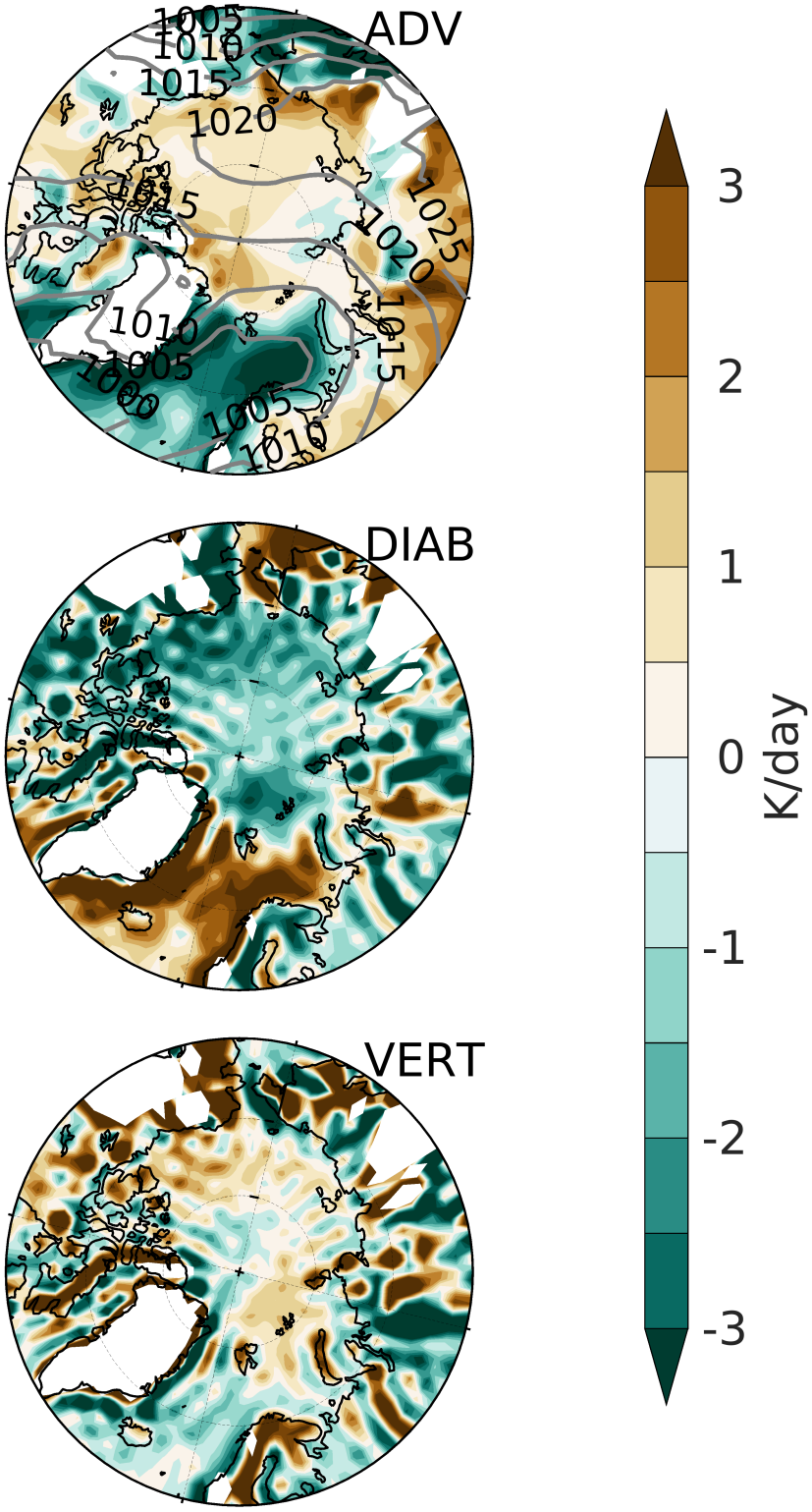

Figure 5.1: 1979–2016 average of 6-hourly winter (DJF) patterns of the advection term (ADV, top panel), diabatic term (DIAB, middle panel) and the vertical term (VERT, bottom panel) following equation (5.1) at the 925 hPa level in Era-Interim. Regions where the local orography is above the average 925 hPa level are left white. In the top panel, gray contour lines show the average SLP in hPa.

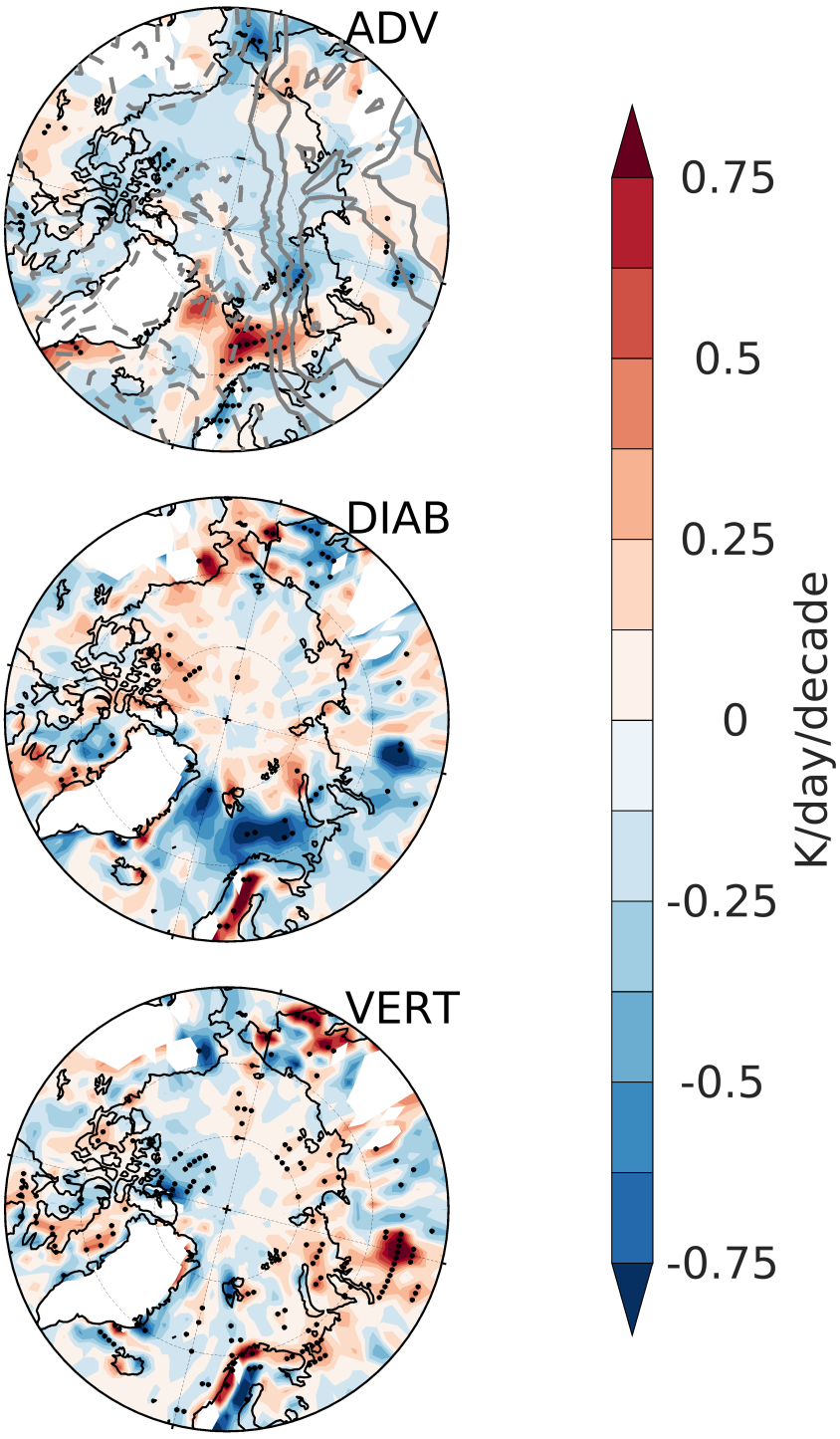

Figure 5.2: Decadal trends over 1979–2016 in the 6-hourly winter (DJF) patterns of the advection term (ADV, top panel), diabatic term (DIAB, middle panel) and the vertical term (VERT, bottom panel) following equation (5.1) at the 925 hPa level in Era-Interim. Significant (95%) trends are indicated with a dot. Regions where the local orography is above the average 925 hPa level are left white. In the top panel, gray contour lines show the decadal trend in SLP, with dashed lines for negative trends and contours every 0.3 hPa/decade.

tilted in the north-south direction, indicating northerly flow. However, between northern Scandinavia and Svalbard, the meridional flow is sluggish, and SLP isolines rather indicate zonal flow. The mean cold advection between Svalbard and Northern Scandinavia may therefore be rather explained by zonal advection features.

The structure of the vertical term in the bottom panel of Figure 5.1 appears to be linked to the location of major topographic features, such as Greenland, the Scandinavian- and Ural Mountains and Brooks Range in northern Alaska, and consists of rather localized features.

Next, temporal changes in winter time ADV, DIAB and VERT patterns over the 1979–2016 period are investigated. Both atmospheric circulation as well as surface parameters (i. e. sea ice) and related processes have undergone marked changes in that period, as was presented in the previous chapters. As a consequence, one would expect to see changes in the ADV, DIAB, and VERT term. Figure 5.2 shows the decadal trends of these parameters. In the top panel, the gray lines represent trends in SLP and the SLP trend pattern underlines the circulation changes that were discussed in section 4.2 in the context of changing Ny-Ålesund air mass source regions, namely a dipole of decreased SLP over Greenland and increased SLP over much of Siberia and particularly over the Ural mountains. One has to note though, that the analysis in this Section starts already in 1979, while the trajectory study was centered in the 1996–2016 period. It is evident from the ADV panel in Figure 5.2 that the anomalous meridional circulation over the Barents Sea has triggered significant positive trends in warm advection covering the area south of Svalbard. Over the Bering Strait, where the anomalous circulation pattern introduces anomalous southward flow from the central Arctic, a region of anomalous cold advection is emerging. The pronounced warm advection tendency between Svalbard and Novaya Zemlya was already noted by Serreze et al. (2011), who built a link to sea ice loss in the northern Barents Sea. Since latent energy is transported away from the region of anomalous warm advection via the anomalous wind, negative DIAB trends (i. e. diabatic cooling) are evident over the Barents Sea and Fram Strait. At the same time, there is some indication for enhanced diabatic warming north of Svalbard and Novaya Zemlya. These features are consistent with enhanced latent heat release from the ocean to the atmosphere in the vicinities of sea ice loss, which can be reinforced through the additional radiative forcing from accociated changes in cloudiness and water vapor (sea ice–insulation feedback).

The trend of the vertical terms seems to reflect the circulation changes. The continuity equation (1.15) requires anomalous downward (upward) velocities in anticyclonic (cyclonic) anomalous circulation patterns, which is clearly observed northwest of Greenland and over the Ural region.

The same analysis for the individual months December, January and

February (not shown) reveals that the trends mostly stem from early to mid winter (December and January), while they are mostly weak and insignificant in February. This is consistent with Crasemann et al. (2017), who identified the increasing occurrence frequency of the Scandinavian high–Iceland low dipole pattern for December and January, but not for February.

5.2 SUMMER

The same analysis as for winter is repeated for the summer season. Figure 5.3 provides climatological estimates of the respective ADV, DIAB and VERT terms. Compared to the winter, the amplitudes of the three terms are generally weaker, because both horizontal circulation and meridional temperature gradients are weaker during summer. In contrast to the findings for the winter season, the dominant feature is an Arctic-wide land-ocean contrast, with ADV and DIAB opposing each other. Thereby, most areas over the Arctic ocean are governed by warm temperature advection, while the Arctic landmasses are characterized by cold advection. The diabatic term acts contrary by average diabatic cooling over the Arctic Ocean, while over the Arctic landmasses, diabatic warming prevails. As outlined in Serreze et al. (2011), an interpretation of the diabatic term during summer follows from surface interactions with solar radiation. Over land, solar radiation is used to heat up the surface, such that increased longwave emission from the surface will heat the atmosphere above the ground. Also, convection and precipitation may set in, driving latent heat release to the atmosphere and hence diabatic warming above the ground. Over the ocean, the situation is different. Over ice surfaces, the temperature is locked to the freezing point, because solar radiation is used to melt the ice. Over water, solar radiation will lead to an increase of the oceanic mixed layer heat content. Both of these processes will leave the temperature of the atmosphere above rather unaffected, resulting in a net diabatic cooling.

In that respect, Svalbard shares the behaviour of the Arctic Ocean rather than sharing features of an Arctic landmass. This is because firstly, also during summer more than half of Svalbard is covered by glaciers and snow, which act as sink for the diabatic term rather than as source. Secondly, Svalbard is too small to establish marked diabatic heating signals in the atmosphere above, because constant exchange with surrounding marine air masses overrules these features, in the same way as observed in the coastal regions of northern Siberia (Figure 5.3, middle panel).

Turning to trends, Figure 5.4 provides an overview for the summer season. Note that the color scale is different than the one for winter trends. The trend of SLP is shown as grey contour in the top panel. The main feature is the trend towards higher pressure over Greenland

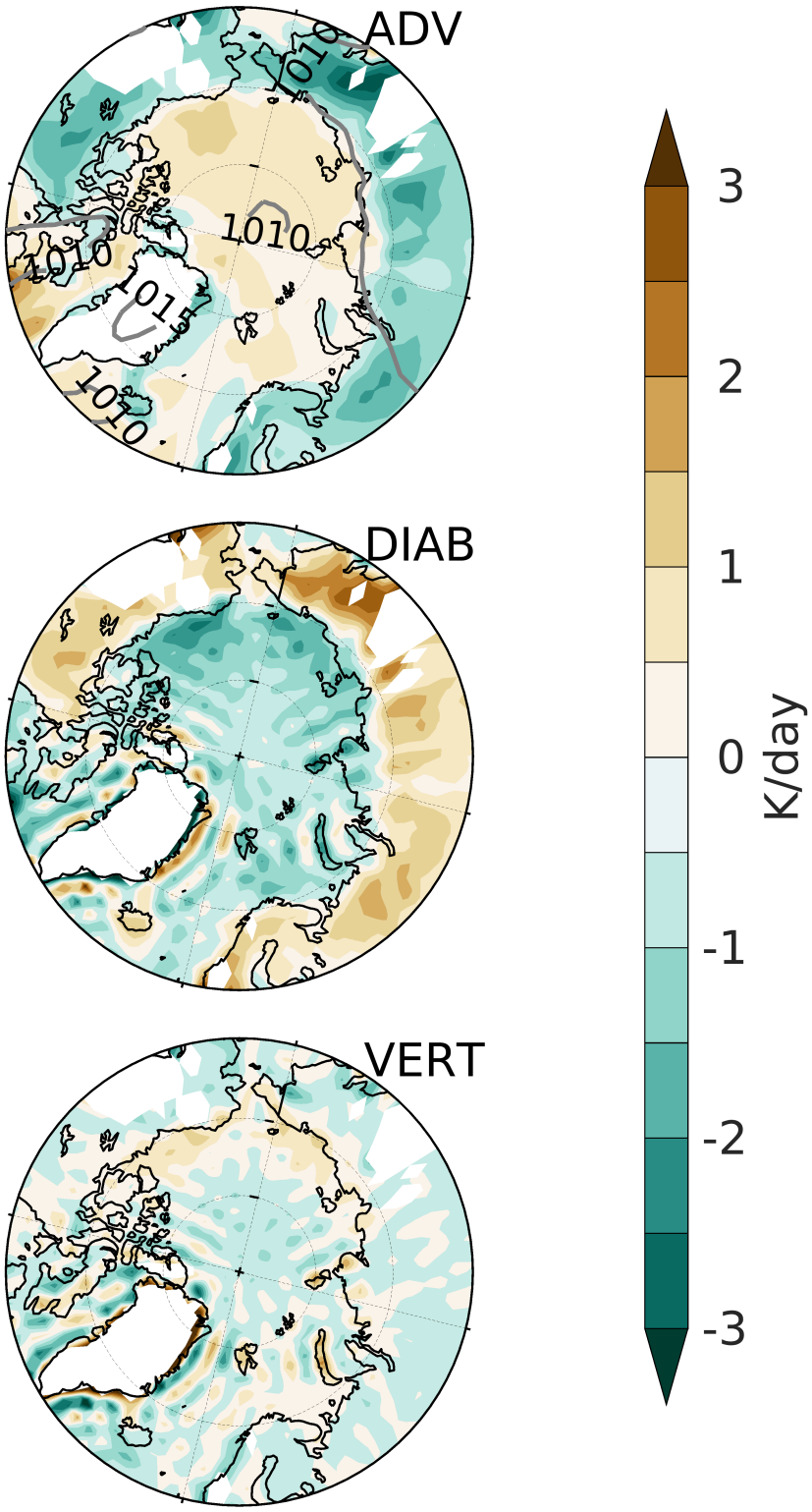

Figure 5.3: Same as Figure 5.1, but for summer: 1979–2016 average of 6-hourly summer (JJA) patterns of the advection term (ADV, top panel), diabatic term (DIAB, middle panel) and the vertical term (VERT, bottom panel) following equation (5.1) at the 925 hPa level in Era-Interim. Regions where the local orography is above the average 925 hPa level are left white. In the top panel, gray contour lines show the average SLP in hPa.

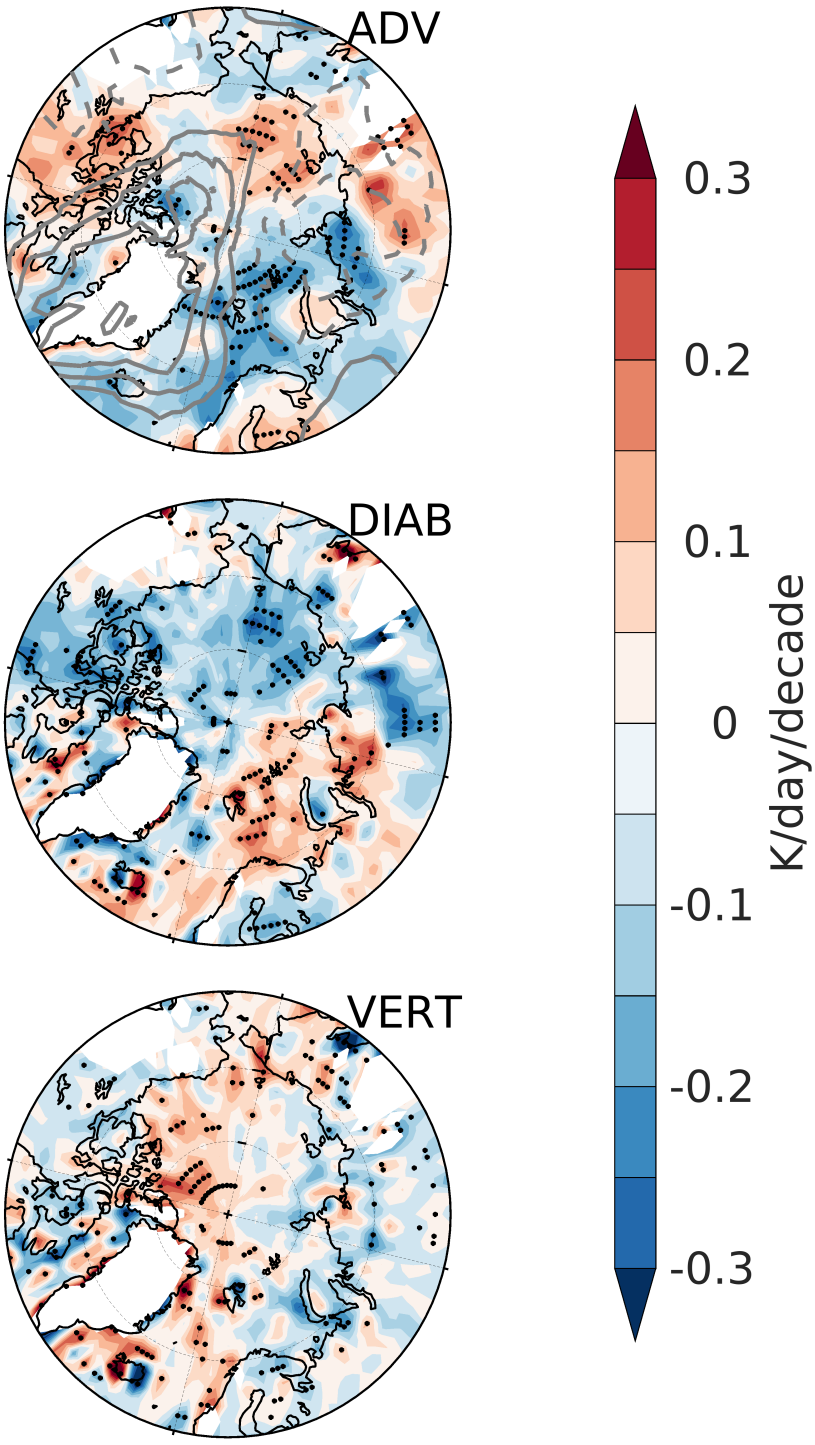

Figure 5.4: Same as Figure 5.2, but for summer: Decadal trends over 1979–2016 in the 6-hourly summer (JJA) patterns of the advection term (ADV, top panel), diabatic term (DIAB, middle panel) and the vertical term (VERT, bottom panel) following equation (5.1) at the 925 hPa level in Era-Interim. Significant (95%) trends are indicated with a dot. Note that the color scale is different than in Figure 5.2. Regions where the local orography is above the average 925 hPa level are left white. In the top panel, gray contour lines show the decadal trend in SLP, with dashed lines for negative trends and contours every 0.3 hPa/decade.

and extending northward into the central Arctic, projecting on the intensified Greenland blocking, which has been broadly discussed in Section 4.3. There it was shown that the Greenland high is associated with negative temperature anomalies in Ny-Ålesund. Indeed, over the whole Atlantic sector surrounding Svalbard, significant cold advection trends are found that go along with the circulation changes over Greenland. The anomalous northerly wind component pushes cold polar air from the central Arctic southward over the ice edge, which finds recognition as cold avection in regions south of the ice edge. The cyclonic low pressure anomaly over the Taymyr pensinsula (dashed contours in top panel of Figure 5.4) on the other hand is suggestive to cause the significant region of anomalous warm advection to its east and anomalous cold advection to its west. This is because the climatological fields of diabatic heating (Figure 5.3, middle) affect atmospheric temperature in a way such that a negative land–ocean temperature gradient is installed. The anomalous poleward circulation over eastern Siberia and anomalous southward circulation over the Taymyr peninsula, crossing the coast, then leads to anomalous warm- and cold advection, respectively. Trends in the advection term are generally countered by opposing trends in the diabatic term (Figure 5.4, middle). This is mainly because temperature changes through advection in the atmosphere imprint on the downward longwave radiation, hence affecting the amount of energy going into ice melting or into the oceanic mixed layer.

The trend of the vertical term is dominated by significant warming north of Greenland and the Canadian Arctic archipelago. This follows from continuity reasons in connection to the anomalous high pressure in the same region. Interestingly, this is exactly the region in the Arctic, where the lower troposphere has warmed strongest during summer in recent years (see Figure 4.7 (a)). A possible explanation would be that high pressure in the region drives descending motions and clear sky conditions, which increases the transmitted solar radiation, leading to warming in the atmosphere. Moreover, there is some indication that the high pressure pattern over Greenland drives meridional warm advection into the region over northern Canada (Figure 5.4 (a)).

Corresponding maps for spring and autumn are not included for the sake of simplicity, as they comprise mixed features of both winter and summer maps. However, maps for the autumn and spring trend patterns in ADV, DIAB and VERT are provided in the Appendix Section in Figures B.2 and B.3, respectively. The most striking feature in the autumn trend maps (Figure B.2) is significantly enhanced warm advection south of Svalbard, as well as significant diabatic heating around Franz Josef Land and Novaya Zemlya, in good agreement to the winter maps. During spring (Figure B.3), the area from Svalbard to Novaya Zemlya is as well subject to significant diabatic warming trends, opposed by the combined effect of cooling via the ADV and

VERT term. Hence, the atmosphere above the northern Barents/Kara Seas is characterized by trends towards anomalous positive diabatic heating in all seasons of the year. This is consistent with the observed year-round sea ice reductions in that region, as indicated in Figure 1.3.

5.3 SUMMARY

The combination of horizontal advection of temperature, adiabatic vertical motion and diabatic heating/cooling maintains the 6-hourly temperature field in the Arctic lower troposphere. The spatial patterns of these terms, and in particular their long term changes, are strongly dependent on both changing atmospheric circulation and changing surface conditions in relation to sea ice reduction, with vertical feedback mechanisms building the bridge between them. The circulation changes during both winter and summer as well as associated signals in horizontal advection underline the results from Chapter 4 in association with air mass source regions for Ny-Ålesund. Trends in summer circulation introduce anomalous southward flow towards Svalbard, crossing the ice edge to its north and leading to advective cooling over Svalbard and the Barents/Kara Seas. Trends for the winter season are opposing those during summer. An anomalous dipole pattern during winter drives anomalous northward flow in the vicinity of Svalbard and the Barents Sea, which leads to significant warm advection trends in that region, consistent with what was postulated in Section 4.2. From an inspection of Figure 5.2 (a) it becomes also clear that the anomalous warm advection feature over the Barents Sea in the recent decades is a phenomenon rather unique in the Arctic, since such features are not found elsewhere on the map. Serreze et al. (2011) argued that this warm advection anomaly motivates sea ice melt in the northern Barents/Kara Sea, where the opening water areas then release latent heat to the atmosphere, which in turn helps to sustain these open water areas via anomalous downward radiation. In fact, diabatic warming trends over the northern Barents/Kara Seas are found for all seasons, consistent with the emergence of ice loss in all seasons in that region. There is evidence that the ocean may have a significant impact on sea ice reductions in the Barents/Kara Seas (Smedsrud et al., 2013; Sandø et al., 2014), which should be subject to future investigations. Svalbard is located in this region of emerging signals with major importance for the Arctic-mean climate, and may be viewed as hotspot for studying the ongoing recent changes.

6

SUMMARY AND CONCLUSION

The climate around the globe has been in a constitution of warming over the last century, with an especially strong warming tendency over the last three to four decades. However, this warming is not uniformly distributed over the globe, but appears to be strongest in the Arctic region and after the mid 1990s. In concert with the pronounced warming, corresponding changes are also apparent in related Arctic climate parameters. These include reduction in sea ice cover and thickness, later (earlier) onset of the freezing (melting) seasons, changing circulation patterns, changes in cloud parameters and moisture content, as well as changes in vertical turbulent fluxes in the planetary boundary layer. The term "Arctic Amplification (AA)" is used to describe the ratio of surface warming in the Arctic alone versus global mean surface warming. While AA is shown to be of the order of 2–3, a complex interplay of physical processes and feedback mechanisms specific to the Arctic must be considered in the effort of an explanation. Thereby, local feedbacks in the Arctic due to rapidly changing surface conditions and associated latent, sensible and radiative energy fluxes can be contrasted to more remote effects, such as oceanic and atmospheric energy transports towards the Arctic. Conclusive insights in the quantitative role of individual processes would be desirable, but this remains subject to debate. Observations of relevant processes are sparse in the Arctic, and there exist substantial uncertainties in future climate projections in the Arctic, with marked differences between different climate models. Reliable observational data from the quickly changing Arctic can help to better understand processes on the local scale and in conjunction with the development of sophisticated, high-resolution, process-resolving regional climate models represent the baseline for adding value to future projections in this highly sensitive environment.

In this thesis I focus my studies on recent changes in air temperature, sea ice cover, as well as atmospheric circulation in the Svalbard region. Svalbard is located in the North Atlantic Sector of the Arctic, and is an exceptional place to study the recent Arctic climate change due to a number of reasons. At first, Svalbard is located in that region of the Arctic, where associated climate parameters are changing at an unrivaled rate. This can be seen when analysing Arctic-wide gridded fields of relevant parameters from atmospheric reanalysis products. In the Era-Interim reanalysis, for instance, spatial patterns of near surface temperature trends, as well as trends in sea ice concentration show local peaks in the Barents/Kara Seas to the east of Svalbard

during winter, with significant anomalies also expanding westwards towards the Svalbard archipelago. It is noteworthy that also in the free troposphere, areas of strong warming occur predominantly in the vicinity of Svalbard. This must be understood being in close relation to the second idiosyncrasy of the region. While almost all other places of the inner Arctic are bounded by landmasses to the south, this does not apply for the Atlantic sector, where large open water areas represent the southern boundary, strongly shaping meridional energy transport. This is true for both the ocean, which supplies the Svalbard region and adjacent seas with comparably warm water currents, as well as for the atmosphere, where the north Atlantic storm track is known for northward propagating synoptic weather systems, carrying anomalous heat and moisture. Moreover, marked surface heterogeneities exist around Svalbard, given the transition from open water surfaces in the south and west to sea-ice covered areas in the north and east. These in turn are shaping vertical turbulent energy fluxes in the region, representing the coupling (or decoupling) between the surface and the free atmosphere. The third way in which Svalbard is a special place for scientific investigations results from its rather well documented long-term in situ climate observations, which are mainly conducted by the Norwegian Meteorological Institute, as well as several international research stations across the archipelago. The abundance of such long–term observational data sets is crucial for identifying climate variability on a regional scale, and is generally limited to few sites in the sparsely sampled Arctic.

With Svalbard as a key region for Arctic changes, the first research question addressed in this thesis was

RQ1: How can Pan-Svalbard differences in the surface meteorology and sea ice development be quantified and classified, and what are the responsible oceanic and atmospheric processes in driving those regional differences?

In this context, a detailed assessment of Pan-Svalbard differences in characteristics of the surface temperature field, as well as local sea ice cover in the fjords and straits of the archipelago is conducted in Chapter 3. This investigation is based on a compilation of unique observational data sets from Svalbard over the 1980–2016 period, including a network of station-based surface air temperatures (SAT), a long-term record of operational sea ice charts for individual fjords and straits, as well as water temperatures from the adjacent shelf seas. SAT records reveal a pronounced spread in absolute values and seasonality across Svalbard, despite the limited spatial extent of the study area. Referring to RQ1, climatological SAT in the coldest northern and eastern vicinities of Svalbard is found to be up to 6 K colder than at the stations along the western coast and in the south of Svalbard. Also, the amplitude of the seasonal cycle, being a measure for continentality

of the local climate, shows larger values (≈21–22 K) in the central part of Spitsbergen compared to the coastal areas (15–19 K). Such gradients are explained by a combination of local surface conditions and the supply of the western coastal areas with heat from both atmospheric and oceanic contributions. More precisely, the western coastal regions are prone to the influence of the warm waters of the West Spitsbergen Current (WSC), which drives a comparably mild climate, particularly during winter. Local evaporation over the open water surfaces along the western coast may increase water vapor in the atmosphere and favour cloudiness. The anomalous downward longwave radiation in accordance with these can be thought of as an amplifying process. These effects are much weaker around Nordaustlandet and Edgeøya in the north and east, where the abundance of sea ice during most of the year limits the impact of the underlying ocean on the atmosphere aloft via thermal insulation.

Seven stations have a long–term data record available, which allows trend analysis. The time series reflect the unprecedented warming in the region, with annual mean warming among those seven stations of 1–1.5 K per decade, but these estimates are outclassed by a twice as strong winter (DJF) warming signal.

An analysis of operational ice charts follows in Chapter 3.3. It reveals that in concert with surface warming, also the sea ice extent (SIE) in the fjords across Svalbard have undergone rapid changes. Generally, the average SIE estimates differ between the southern/western parts of Svalbard and the northern/eastern parts. In the south/west, SIE is a very seasonal feature, since those fjords are mostly ice-free (< 20% SIE) during summer and autumn, and show maximum SIE of about 40–60% during spring. Fjords and straits in the northern and eastern sectors of Svalbard, on the other hand, generally indicate the abundance of substantial SIE for most of the year, with the exception of autumn. Thereby, maximum extents during spring exceed 80–90%. These estimates however refer to the climatology. From 1998–2016, significant downward trends in SIE are found for most regions. In the western fjords, this has lead to virtually ice-free conditions during recent winters and springs, while also in the east and north, SIE has shrunk towards 40–60% recently. This implies that for SIE, the remote north-eastern regions have recently become more similar to what used to be the "average" conditions in the south-west. Turning to regional differences in the long-term (1980–2016) variations of SIE, three fairly distinctive, different patterns are identified:

1. No or weak decline in earlier years, followed by strong decline after the mid-2000s. (pattern 1 – western Svalbard)

2. Increasing SIE tendency in the 1980s and 1990s, followed by a strong decline (pattern 2 – north/north-western Svalbard)

3. close to 100% sea ice coverage until strong decline in recent years (pattern 3 – north-eastern/eastern Svalbard)

Potential drivers for these regional differences are investigated to account for the second part of RQ1. Statistical evidence is presented that depending on the regions, interannual SIE variability during winter can be impacted by both warm waters within the WSC or by anomalous atmospheric meridional circulation west of Svalbard, that impacts sea ice drift and advection. Within the linear framework of correlation analysis it is estimated that during the first half of the record (1980–1997), water temperature anomalies in the WSC can explain up to 20–37% of SIE variability in several "pattern 1" fjords. At the same time, meridional wind anomalies off the north-western coast of Svalbard, highly associated with sea ice drift, can explain 20–35%, and locally more than 50% of SIE variability in a number of "pattern 2" and "pattern 3" fjords in the north and east. However, these statistical significant relations broke down during the more recent years 1998–2016, when the strong SAT warming apparently dictated excessive ice loss. To the existing pool of literature on the climate of Svalbard, my analysis adds valuable information about both SAT and SIE in the more remote northern and eastern vicinities of the archipelago, from where little is known with regards to the local climate (Hanssen-Bauer et al., 2019). Up to date, most research has been focused on the extensively sampled western coastal regions. Also, a Pan-Svalbard picture synthesizing SIE characteristics from numerous fjords and straits, also linking their variability to atmospheric circulation, hydrographic anomalies, and local SAT estimates, has to my knowledge not yet emerged from any study. Potential future work could be centred on a more in depth analysis to elucidate the detailed physical mechanisms and feedbacks behind ocean, sea ice and atmosphere interactions in this key region of AA. Fine scale, non-hydrostatic regional models may represent feasible tools for employing such analyses.

Enlarging the view from the local and regional effects on Svalbard, the second research question emerges:

RQ2: Svalbard is located in the transition zone between cold polar air and warm airmasses from lower latitudes, impacted by both depending on the atmospheric circulation. To what degree are large scale circulation changes contributing to the observed warming over the last decades?

A broader perspective regarding the role of atmospheric circulation changes on temperature development in the Svalbard area is provided in Chapter 4. The analysis is based on FLEXTRA 3-dimensional airback trajectories for the location of Zeppelin mountain, Ny-Ålesund, covering the 1996–2016 period. In that period, Svalbard has been a hotspot of winter warming at the 850 hPa level in the Arctic. A strong

dependence of tropospheric air temperatures above Ny-Ålesund on the wind direction is revealed, with about 8 K warmer temperatures during southerly compared to northerly flow. This reflects the contrast of advecting either cold, dry air from the central polar regions or warm, humid air masses and associated clouds from the North Atlantic region. From the 6-hourly trajectories, air mass "source regions" were calculated as the location of air parcels three days before they reached Ny-Ålesund at 850 hPa. The analysis for winter (DJF) reveals that a shift took place between P1 (1996–2006) and P2 (2007–2016), such that air masses during P2 originated significantly more often in the North Atlantic sector to the south of Svalbard, and were less often of central Arctic origin. In numbers, the North Atlantic had been source region to Ny-Ålesund air in 16% (21%) of cases during P1 (P2), representing a relative increase of 30%. Further analysis shows that anomalous atmospheric circulation was responsible for this shift, including anomalous low pressure over Greenland and Iceland, and anomalous high pressure over Scandinavia and the Ural region, reaching 8 hPa in maximum amplitude of sea level pressure (SLP), each. This pattern has been discussed to be associated with sea ice loss in the Barents/Kara Seas (Crasemann et al., 2017) and atmospheric blocking (Luo et al., 2016). My investigations provide evidence that the increased occurrence frequency of this circulation pattern during P2 compared to P1, may explain about a quarter (25%) of the observed overall warming on Svalbard during the last two decades. However, this underlines that additional processes and feedbacks in association with the surface conditions must be active and are important in the study region. The results are not inconsistent with Isaksen et al. (2016), who find that warming occurs for all the major circulation patterns observed around Svalbard, but who also agree that circulation changes may contribute to the amplified winter warming.

An application of the same trajectory analysis for the summer season (JJA) shows very different results. During summer only moderate warming is observed at 850 hPa above Ny-Ålesund, while the region north-west of Greenland appears to be a hotspot of summer warming during the last two decades. Significant shifts in source regions of Ny-Ålesund air are also found for summer, but towards more frequent air advection from the central Arctic region, and less frequent inflow from the North Atlantic. The source region changes during summer are driven by enhanced occurrence of anomalous high pressure over Greenland and the central Arctic during P2, associated with the Greenland blocking pattern, and anomalous low pressure over northern Siberia. The resulting northerly flow component pushes cold and dry polar air over the ice edge towards Svalbard, which contributes to a cooling of 0.2–0.3 K per decade at the 850 hPa level during 1997–2016. Hence, winter circulation changes tend to amplify the recent warming in the Svalbard region, while summer circulation changes tend to

mask a stronger warming. Potential future research regarding the circulation changes around Svalbard could focus on a more in depth analysis of their impact on surface conditions, such as sea ice cover and inversion strength, and the magnitude of the associated vertical feedback mechanisms. Transformation of airmass properties, particularly with respect to cloud parameters, go along with the meridional exchange of airmasses in the Arctic (Pithan et al., 2018). Since the latter are shown to be subject of recent change around Svalbard, a closer investigation of such transformations in the region would also be a point that deserves further investigation.

Since a large part of the long-term atmospheric observations used in this study were retrieved at Ny-Ålesund, the third research question arises:

RQ3: On the background of the observational super-site Ny-Ålesund located on Svalbard's west coast, how representative are the recent changes in the Svalbard region with regard to the broader Arctic and regional differences in Arctic warming trends?

Therefore, in Chapter 5, the contributing terms to temperature changes in the diagnostic temperature equation are analysed. This Arctic-wide analysis is based on the 6-hourly fields at near surface levels from the Era-Interim reanalysis, and for the 1979–2016 period. Results confirm the differing seasonal temperature advection trends in the Svalbard region, with significantly enhanced warm advection during winter, and enhanced cold advection during summer. This circum-Arctic analysis shows that the associated advection trend patterns are confined to the broader North Atlantic sector of the Arctic, ranging from Fram Strait over Svalbard to Novaya Zemlya. In winter, the pattern of enhanced warm advection is centered over the Barents Sea between Svalbard and northern Scandinavia, and extends also over the Northern Fram Strait. Hence, Svalbard is located in the region representative for the discussed recent advection changes over the Arctic North Atlantic, that are by themself unique in the Arctic. The seasonal analysis further evidences that the lower atmosphere above the northern Barents/Kara Seas and Svalbard is subject to diabatic warming trends in all seasons. This correlates with the concept of observed sea ice loss, enhanced latent and sensible heat fluxes towards the atmosphere and enhanced downward longwave radiation by atmospheric layers aloft. Overall, the results illustrate the unique climate changes in the North Atlantic sector of the Arctic, and give evidence for the combined dynamical and thermodynamical processes that are involved. It should also be noted however, that the results may differ for other climate parameters that are not directly reflected by equation (5.1). The results further suggest a strong seasonal dependence of representativeness, as dynamical changes, sea ice distribution and the PBL structure, which represents the link between those, also show a strong seasonality.

Given that, it is an inevitable challenge for future studies to assess the mid- to longterm trajectory of the climate in the Svalbard region on the background of Arctic changes.

A

DETAILS ON CALCULATIONS

A.1 SLP COMPOSITE INDEX

In Chapter 4, an index is presented (Figures 4.3 (b) and 4.6 (b)) that describes the temporal evolution of a respectively specified stationary spatial pattern of sea level pressure (Figures 4.3 (a) and 4.6 (b), respectively). Its derivation is detailed in the following. The index is derived by projecting the SLP composite pattern on the 6-hourly SLP field. In a first step, significance of the composite SLP pattern is estimated by a two-sided student's t test against the null hypothesis that the true SLP composite is zero. The presence of autocorrelation in the 6-hourly data reduces the effective degrees of freedom. This is accounted for by using a modified number of degrees of freedom

$$N_{eff} = N\frac{(1-r)}{(1+r)} \tag{A.1}$$

Where N is the length of each time series and r is the lag 1 autocorrelation coefficient of SLP at each grid point. The significant and relevant part of the SLP composite pattern is isolated by setting grid points with p-values > 0.01 and with -2 hPa < p < 2 hPa = 0. The second step is done to furher reduce the contributions from far away regions in the tropics and subtropics, where weak but significant composite values can be achieved, and to focus the index on prounced circulation anomalies. The resulting pattern is then weighted by the cosine of latitude, to account for the shrinking grid cell size towards the pole. The absolute values in the remaining are then summed up and the sum is saved as a weighting value:

$$W = \sum_{ij} |p_{ij}| \cos(\Phi_j) \tag{A.2}$$

$$P_{compo,ij} = \frac{p_{ij} \cdot \cos(\Phi_j)}{W} \tag{A.3}$$

where

- i longitude index
- j latitude index
- p SLP composite
- Φ geographical latitude

In that way, the SLP composite pattern is normalized such that $\sum_{ij} |P_{compo,ij}| = 1$, while still accounting for its spatial structure. The resulting pattern is then grid point-wise multiplied by the 6-hourly

SLP anomaly field, and spatially averaged to yield one index value per time step. In a last step, the index is normalized to yield zero mean and unit standard deviation. The final index that is presented in Figures 4.3 (b) and 4.6 (b) results from additionally applying a Butterworth low pass filter with a cutoff frequency of 3 years in order to highlight low frequency variability. The dimension-less index serves as illustration for how strongly pronounced (amplitude-wise) and well defined (spatial expression) the prescribed pattern has been over the years, and does not allow for a direct physical interpretation.

A.2 DERIVATION OF COEFFICIENT OF DETERMINATION

From equation (2.5), it follows that

$$r^2_{\hat{Y},Y} = \left(\frac{C(\hat{Y},Y)}{\sqrt{(var(\hat{Y})var(Y))}} \right)^2 \tag{A.4}$$

$$= \left(\frac{C(\hat{Y},Y)}{\sqrt{(var(\hat{Y})var(Y))}} \right) \left(\frac{C(\hat{Y},Y)}{\sqrt{(var(\hat{Y})var(Y))}} \right) \tag{A.5}$$

$$= \frac{C(\hat{Y},Y)C(\hat{Y},Y)}{var(Y)var(\hat{Y})} \tag{A.6}$$

$$= \frac{C(\hat{Y},\hat{Y}+\epsilon)C(\hat{Y},\hat{Y}+\epsilon)}{var(Y)var(\hat{Y})} \tag{A.7}$$

$$= \frac{(C(\hat{Y},\hat{Y}) + C(\hat{Y},\epsilon))(C(\hat{Y},\hat{Y}) + C(\hat{Y},\epsilon))}{var(Y)var(\hat{Y})} \tag{A.8}$$

Since the errors ϵ of the model are assumed to be uncorrelated with $\hat{Y}$, equation (A.8) reduces to:

$$r^2_{\hat{Y},Y} = \frac{C(\hat{Y},\hat{Y})C(\hat{Y},\hat{Y})}{var(Y)var(\hat{Y})} \tag{A.9}$$

$$= \frac{var(\hat{Y})var(\hat{Y})}{var(Y)var(\hat{Y})} = \frac{var(\hat{Y})}{var(Y)} \tag{A.10}$$

$$= \frac{\frac{1}{n}\sum_i(\hat{Y}_i - \overline{Y})^2}{\frac{1}{n}\sum_i(Y_i - \overline{Y})^2} \tag{A.11}$$

$$= \frac{SS_{REG}}{SS_{TOT}} \tag{A.12}$$

A.3 TEMPERATURE EFFECT OF CHANGING SOURCE REGIONS OVER TIME

The derivation of equation (4.1) is done by splitting the mean temperature of a specific period into the mean temperature of ATL box days (T_{ATL}) and non-ATL box days ($T_{\neg ATL}$) at each grid point as follows:

$$\bar{T} = \frac{1}{N}\sum_{i=1}^{N} T_i; \qquad \text{where } N \in \mathbb{N} \text{ is the number of days in the specific period}$$
$$\Leftrightarrow \bar{T} = \frac{1}{N}\left(T_1 + T_2 + ... + T_{N-1} + T_N\right)$$

At this point I rearrange the days according to their source region

$$\Leftrightarrow \bar{T} = \frac{1}{N}(\underbrace{T_{ATL,1} + T_{ATL,2} + ... + T_{ATL,n_{ATL}}}_{n_{ATL}\cdot\bar{T}_{ATL}} + \underbrace{T_{\neg ATL,1} + T_{\neg ATL,2} + .. + T_{\neg ATL,n_{\neg ATL}}}_{n_{\neg ATL}\cdot\bar{T}_{\neg ATL} = (N-n_{ATL})\cdot\bar{T}_{\neg ATL}})$$
$$\Leftrightarrow \bar{T} = \frac{1}{N}\left(n_{ATL}\cdot\bar{T}_{ATL} + (N - n_{ATL})\cdot\bar{T}_{\neg ATL}\right) \tag{A.13}$$

I seek to isolate the effect of ATL box days. Therefore, $(\bar{T} - \bar{T}_{\neg ATL})$ is inspected. Substituting equation (A.13) for $\bar{T}$ yields:

$$(\bar{T} - \bar{T}_{\neg ATL}) = \frac{1}{N}\left(n_{ATL}\cdot\bar{T}_{ATL} + (N - n_{ATL})\cdot\bar{T}_{\neg ATL}\right) - \bar{T}_{\neg ATL}$$
$$\Leftrightarrow (\bar{T} - \bar{T}_{\neg ATL}) = \frac{1}{N}\left(n_{ATL}\cdot\bar{T}_{ATL} - n_{ATL}\cdot\bar{T}_{\neg ATL}\right) + \cancel{\bar{T}_{\neg ATL}} - \cancel{\bar{T}_{\neg ATL}}$$
$$\Leftrightarrow (\bar{T} - \bar{T}_{\neg ATL}) = \frac{n_{ATL}}{N}\left(\bar{T}_{ATL} - \bar{T}_{\neg ATL}\right) \tag{A.14}$$

The expression from equation A.14 can be calculated for arbitrary time periods separately. For my investigations, the P2 - P1 difference in equation A.14 then can be interpreted as the "warming footprint" of the ATL box from P1 to P2, and this difference reads:

$$(\bar{T}_{P2} - \bar{T}_{\neg ATL,P2}) - (\bar{T}_{P1} - \bar{T}_{\neg ATL,P1}) =$$
$$\frac{n_2}{N_2}(\bar{T}_{ATL,P2} - \bar{T}_{\neg ATL,P2}) - \frac{n_1}{N_1}(\bar{T}_{ATL,P1} - \bar{T}_{\neg ATL,P1}) \tag{A.15}$$

By introducing

$$\Delta\bar{T}_{ATL} = \bar{T}_{ATL,P2} - \bar{T}_{ATL,P1}$$
$$\Delta\bar{T}_{\neg ATL} = \bar{T}_{\neg ATL,P2} - \bar{T}_{\neg ATL,P1}$$

equation (A.15) can be rewritten as

$$(\bar{T}_{P2} - \bar{T}_{\neg ATL,P2}) - (\bar{T}_{P1} - \bar{T}_{\neg ATL,P1}) =$$
$$\underbrace{\frac{n_2}{N_2}\left(\Delta\bar{T}_{ATL} - \Delta\bar{T}_{\neg ATL}\right)}_{\text{I}} + \underbrace{\left(\frac{n_2}{N_2} - \frac{n_1}{N_1}\right)\left(\bar{T}_{ATL,P1} - \bar{T}_{\neg ATL,P1}\right)}_{\text{II}} \tag{A.16}$$

Which is idential to equation (4.1), and can be similarly calculated for source regions other than the ATL box. Term I of equation (A.16) accounts for warming at any grid point, that is not uniformly distributed

between the subset of ATL box days and the subset of non-ATL box days, and is difficult to interprete in regions far away from Svalbard. Term II in equation (A.16) finally accounts for the temperature change solely due to the change in occurrence frequency of the ATL box as source region, and its associated anomalous temperature pattern.

B

SUPPLEMENTARY FIGURES

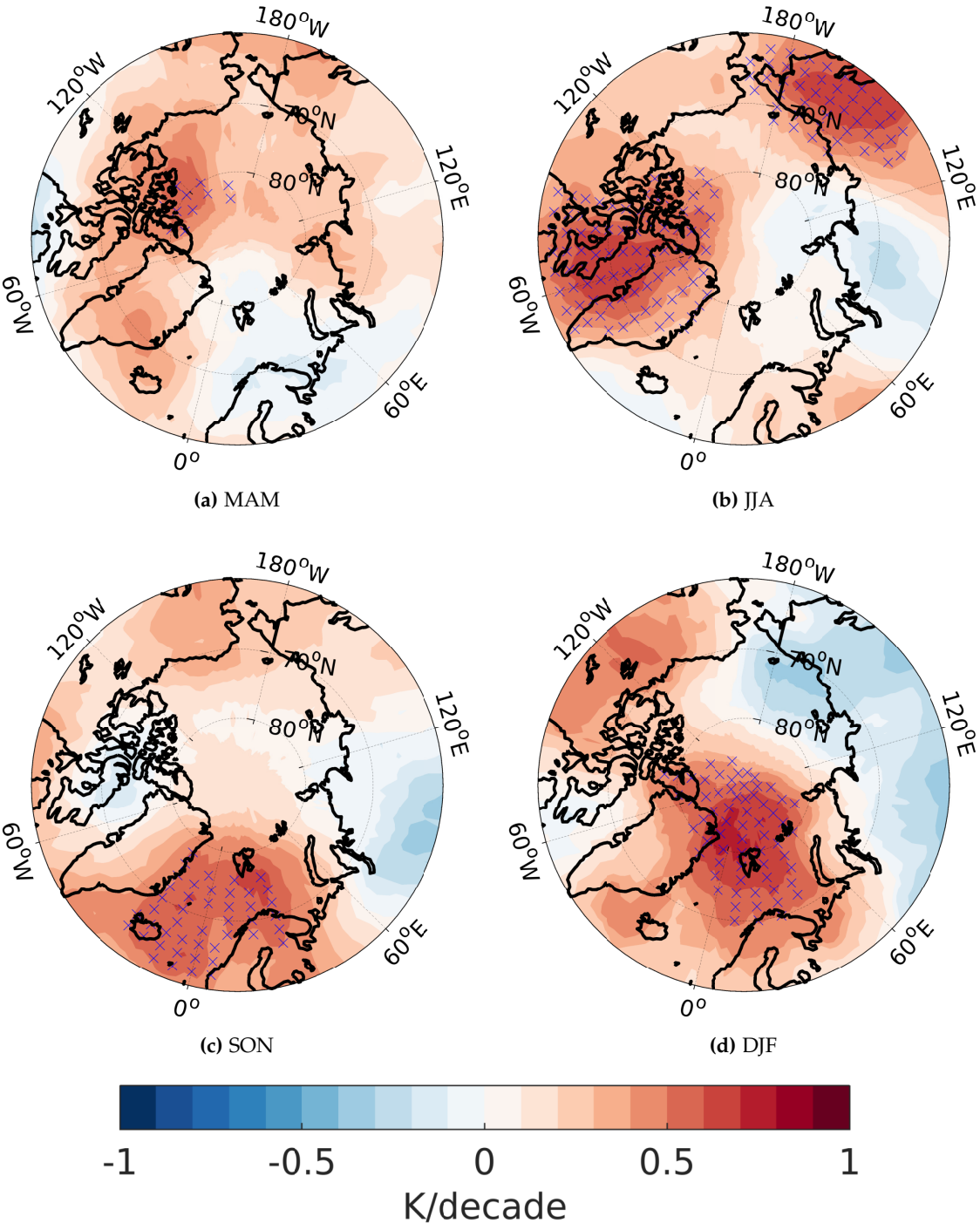

(a) MAM **(b)** JJA

(c) SON **(d)** DJF

Figure B.1: As Figure 1.2, but for the 500 hPa level: 1979–2016 decadal trends in the Era-Interim 500 hPa temperature, for: **(a)**: spring (March–April–May, MAM), **(b:)**: summer (June–July–August, JJA), **(c)**: autumn (September–October–November, SON), **(d)**: winter (December, January, February, DJF). Crossed areas indicate trends significantly (α<0.01) different from zero.

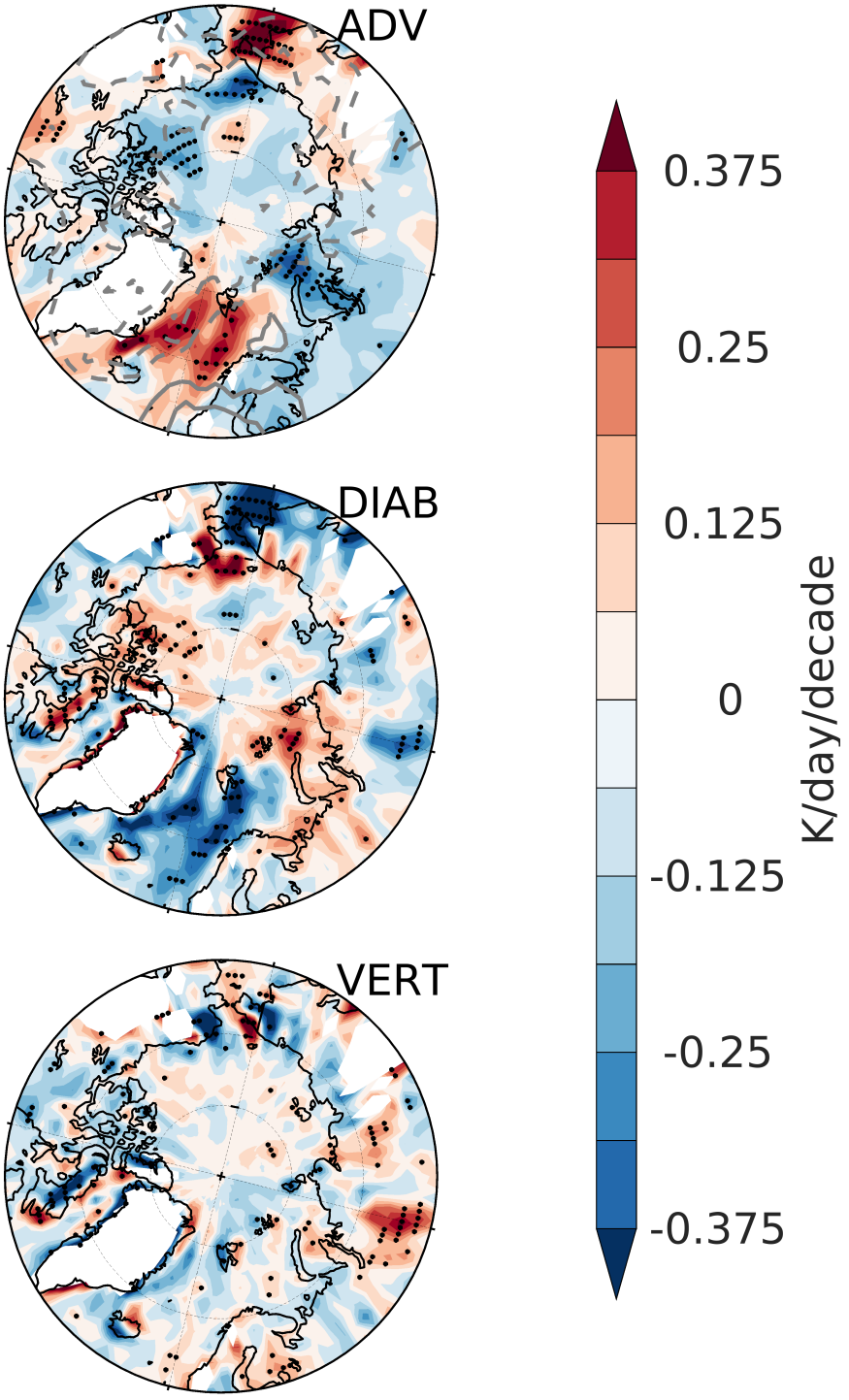

Figure B.2: Same as Figure 5.2, but for autumn: Decadal trends over 1979–2016 in the 6-hourly autumn (SON) patterns of the advection term (ADV, top panel), diabatic term (DIAB, middle panel) and the vertical term (VERT, bottom panel) following equation (5.1) at the 925 hPa level in Era-Interim. Significant (95%) trends are indicated with a dot. Note that the color scale is different than in Figure 5.2. Regions where the local orography is above the average 925 hPa level are left white. In the top panel, gray contour lines show the decadal trend in SLP, with dashed lines for negative trends and contours every 0.3 hPa/decade.

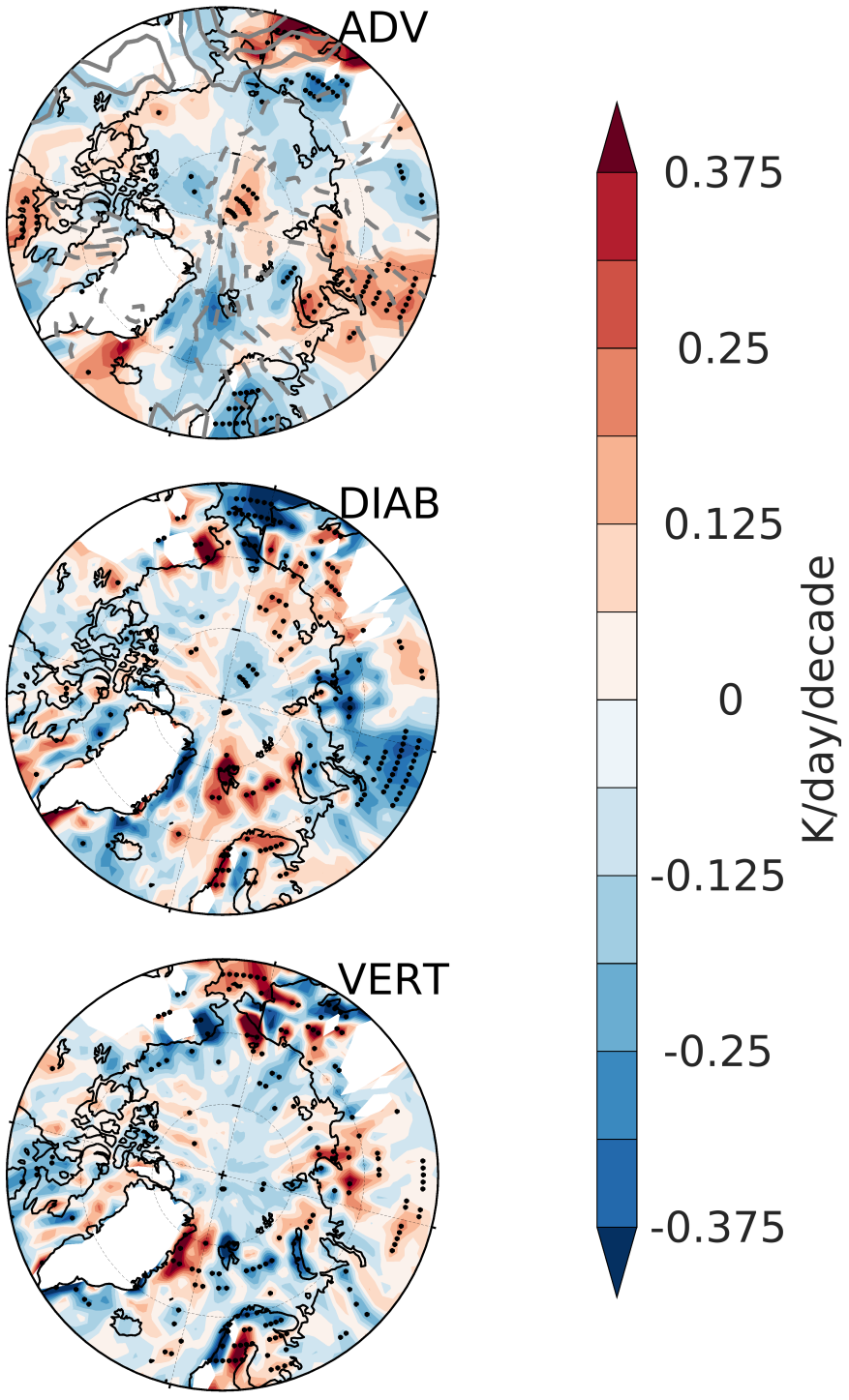

Figure B.3: Same as Figure 5.2, but for spring: Decadal trends over 1979–2016 in the 6-hourly spring (MAM) patterns of the advection term (ADV, top panel), diabatic term (DIAB, middle panel) and the vertical term (VERT, bottom panel) following equation (5.1) at the 925 hPa level in Era-Interim. Significant (95%) trends are indicated with a dot. Note that the color scale is different than in Figure 5.2. Regions where the local orography is above the average 925 hPa level are left white. In the top panel, gray contour lines show the decadal trend in SLP, with dashed lines for negative trends and contours every 0.3 hPa/decade.

BIBLIOGRAPHY

ACSYS (2003). "ACSYS Historical Ice Chart Archive (1553-2002). IACPO Informal Report No. 8. Tromsø, Norway: Arctic Climate System Study." In: *IACPO Informal Report No. 8. Tromsø, Norway: Arctic Climate System Study*.

Berge, J., K. Heggland, O. Lønne, F. Cottier, H. Hop, G. Gabrielsen, L. Nøttestad, and O. Misund (2015). "First Records of Atlantic Mackerel (Scomber scombrus) from the Svalbard Archipelago, Norway, with Possible Explanations for the Extension of Its Distribution." In: *ARCTIC* 68.1, pp. 54–61. ISSN: 1923-1245. DOI: 10.14430/arctic4455.

Beszczynska-Möller, A., E. Fahrbach, U. Schauer, and E. Hansen (Apr. 2012). "Variability in Atlantic water temperature and transport at the entrance to the Arctic Ocean, 1997–2010." In: *ICES Journal of Marine Science* 69.5, pp. 852–863. ISSN: 1054-3139. DOI: 10.1093/icesjms/fss056.

Bintanja, R (2018). "The impact of Arctic warming on increased rainfall." In: *Scientific reports* 8.1, p. 16001. DOI: 10.1038/s41598-018-34450-3.

Bintanja, R, R. Graversen, and W Hazeleger (2011). "Arctic winter warming amplified by the thermal inversion and consequent low infrared cooling to space." In: *Nature Geoscience* 4.11, p. 758. DOI: 10.1038/ngeo1285.

Bintanja, R. and E. Van der Linden (2013). "The changing seasonal climate in the Arctic." In: *Scientific reports* 3, p. 1556. DOI: 10.1038/srep01556.

Blindheim, J. and H. Loeng (1981). "On the variability of Atlantic influence in the Norwegian and Barents Seas." In: *Fiskeridirektoratets Skrevne Serie av Havundersøkelser 17*, pp. 161–189.

Buchholz, F., T. Werner, and C. Buchholz (2012). "First observation of krill spawning in the high Arctic Kongsfjorden, west Spitsbergen." In: *Polar Biology* 35.8, pp. 1273–1279. ISSN: 1432-2056. DOI: 10.1007/s00300-012-1186-3.

Burt, M. A., D. A. Randall, and M. D. Branson (2016). "Dark Warming." In: *Journal of Climate* 29.2, pp. 705–719. DOI: 10.1175/JCLI-D-15-0147.1.

Chen, H. W., Q. Zhang, H. Körnich, and D. Chen (2013). "A robust mode of climate variability in the Arctic: The Barents Oscillation." In: *Geophysical Research Letters* 40.11, pp. 2856–2861. DOI: 10.1002/grl.50551.

Chylek, P., C. K. Folland, G. Lesins, M. K. Dubey, and M. Wang (2009). "Arctic air temperature change amplification and the Atlantic

Multidecadal Oscillation." In: *Geophysical Research Letters* 36.14. DOI: 10.1029/2009GL038777.

Cohen, J., J. A. Screen, J. C. Furtado, M. Barlow, D. Whittleston, D. Coumou, J. Francis, K. Dethloff, D. Entekhabi, J. Overland, and J. Jones (2014). "Recent Arctic amplification and extreme mid-latitude weather." In: *Nature Geoscience* 7.9, pp. 627–637. DOI: 10.1038/ngeo2234.

Cokelet, E. D., N. Tervalon, and J. G. Bellingham (2008). "Hydrography of the West Spitsbergen Current, Svalbard Branch: Autumn 2001." In: *Journal of Geophysical Research: Oceans* 113.C1. DOI: 10.1029/2007JC004150.

Comiso, J. C. and D. K. Hall (2014). "Climate trends in the Arctic as observed from space." In: *Wiley Interdisciplinary Reviews: Climate Change* 5.3, pp. 389–409. DOI: 10.1002/wcc.277.

Cottier, F., F. Nilsen, M. Inall, S. Gerland, V. Tverberg, and H. Svendsen (2007). "Wintertime warming of an Arctic shelf in response to large-scale atmospheric circulation." In: *Geophysical Research Letters* 34.10.

Cottier, F., V. Tverberg, M. Inall, H. Svendsen, F. Nilsen, and C. Griffiths (2005). "Water mass modification in an Arctic fjord through cross-shelf exchange: The seasonal hydrography of Kongsfjorden, Svalbard." In: *Journal of Geophysical Research: Oceans* 110.C12. DOI: 10.1029/2004JC002757.

Crasemann, B., D. Handorf, R. Jaiser, K. Dethloff, T. Nakamura, J. Ukita, and K. Yamazaki (2017). "Can preferred atmospheric circulation patterns over the North-Atlantic-Eurasian region be associated with arctic sea ice loss?" In: *Polar Science* 14, pp. 9–20. DOI: 10.1016/j.polar.2017.09.002.

Curry, J. A., J. L. Schramm, W. B. Rossow, and D. Randall (1996). "Overview of Arctic cloud and radiation characteristics." In: *Journal of Climate* 9.8, pp. 1731–1764. DOI: 10.1175/1520-0442(1996)009<1731:OOACAR>2.0.CO;2.

Dahlke, S. and M. Maturilli (2017). "Contribution of Atmospheric Advection to the Amplified Winter Warming in the Arctic North Atlantic Region." In: *Advances in Meteorology* 2017, Article ID 4928620, 8 pages. DOI: 10.1155/2017/4928620.

Dee, D. P., S. M. Uppala, A. Simmons, P. Berrisford, P Poli, S Kobayashi, U Andrae, M. Balmaseda, G Balsamo, d. P. Bauer, et al. (2011). "The ERA-Interim reanalysis: Configuration and performance of the data assimilation system." In: *Quarterly Journal of the royal meteorological society* 137.656, pp. 553–597.

Dethloff, K., D. Handorf, R. Jaiser, A. Rinke, and P. Klinghammer (2019). "Dynamical mechanisms of Arctic amplification." In: *Annals of the New York Academy of Sciences* 1436.1, pp. 184–194. DOI: 10.1111/nyas.13698.

Divine, D. V. and C. Dick (2006). "Historical variability of sea ice edge position in the Nordic Seas." In: *Journal of Geophysical Research: Oceans* 111.C1. DOI: 10.1029/2004JC002851.

Dobler, A. (2019). "Convection permitting climate simulations for Svalbard - Background-report for Climate in Svalbard 2100." In: *NCCS-Report 2/2019* (www.klimaservicesenter.no).

Drinkwater, K. (2009). "Comparison of the response of Atlantic cod (Gadus morhua) in the high-latitude regions of the North Atlantic during the warm periods of the 1920s–1960s and the 1990s–2000s." In: *Deep Sea Research Part II: Topical Studies in Oceanography* 56.21. The Proceedings of the ECONORTH Symposium on Ecosystem Dynamics in the Norwegian Sea and Barents Sea, pp. 2087–2096. ISSN: 0967-0645. DOI: 10.1016/j.dsr2.2008.12.001.

Esau, I. and I. Repina (2012). "Wind climate in Kongsfjorden, Svalbard, and attribution of leading wind driving mechanisms through turbulence-resolving simulations." In: *Advances in Meteorology* 2012. DOI: 10.1155/2012/568454.

Etling, D. (2002). *Theoretische Meteorologie: Eine Einführung*. Springer-Verlag. ISBN: 978-3-540-75979-9.

Ewert, A. (1972). "About calculating thermic continentality of climate." In: *Prz. Geogr.* 44, 273–328 (in Polish).

Faegri, K. (1950). "On the value of palaeoclimatological evidence." In: *Centenary Proceedings of the Royal Meteorological Society*. Vol. 188, p. 95.

Førland, E. J., I. Hanssen-Bauer, and P. Ø. Nordli (1997). "Climate statistics and longterm series of temperature and precipitation at Svalbard and Jan Mayen." In: *Norwegian Meteorolgical Institute report Klima No21/97*, 72pp.

Francis, J. A. and S. J. Vavrus (2012). "Evidence linking Arctic amplification to extreme weather in mid-latitudes." In: *Geophysical Research Letters* 39.6. DOI: 10.1029/2012GL051000.

Gerland, S., A. H. H. Renner, F. Godtliebsen, D. Divine, and T. B. Løyning (2008). "Decrease of sea ice thickness at Hopen, Barents Sea, during 1966–2007." In: *Geophysical Research Letters* 35.6. DOI: 10.1029/2007GL032716.

Gerland, S. and R. Hall (2006). "Variability of fast-ice thickness in Spitsbergen fjords." In: *Annals of Glaciology* 44, pp. 231–239. DOI: 10.3189/172756406781811367.

Gerland, S. and A. H. Renner (2007). "Sea-ice mass-balance monitoring in an Arctic fjord." In: *Annals of Glaciology* 46, pp. 435–442. DOI: 10.3189/172756407782871215.

Gjelten, H. M., Ø. Nordli, K. Isaksen, E. J. Førland, P. N. Sviashchennikov, P. Wyszynski, U. V. Prokhorova, R. Przybylak, B. V. Ivanov, and A. V. Urazgildeeva (2016). "Air temperature variations and gradients along the coast and fjords of western Spitsbergen." In: *Polar Research* 35.1, p. 29878. DOI: 10.3402/polar.v35.29878.

Gong, T. and D. Luo (2017). "Ural Blocking as an Amplifier of the Arctic Sea Ice Decline in Winter." In: *Journal of Climate* 30.7, pp. 2639–2654. DOI: 10.1175/JCLI-D-16-0548.1.

Graham, R. M., L. Cohen, N. Ritzhaupt, B. Segger, R. G. Graversen, A. Rinke, V. P. Walden, M. A. Granskog, and S. R. Hudson (2019). "Evaluation of six atmospheric reanalyses over Arctic sea ice from winter to early summer." In: *Journal of Climate* 32.14, pp. 4121–4143. DOI: 10.1175/JCLI-D-18-0643.1.

Handorf, D., R. Jaiser, K. Dethloff, A. Rinke, and J. Cohen (2015). "Impacts of Arctic sea ice and continental snow cover changes on atmospheric winter teleconnections." In: *Geophysical Research Letters* 42.7, pp. 2367–2377. DOI: 10.1002/2015GL063203.

Hanna, E., X. Fettweis, and R. J. Hall (2018a). "Brief communication: Recent changes in summer Greenland blocking captured by none of the CMIP5 models." In: *The Cryosphere* 12.10, pp. 3287–3292. DOI: 10.5194/tc-12-3287-2018.

Hanna, E., R. J. Hall, T. E. Cropper, T. J. Ballinger, L. Wake, T. Mote, and J. Cappelen (2018b). "Greenland blocking index daily series 1851–2015: Analysis of changes in extremes and links with North Atlantic and UK climate variability and change." In: *International Journal of Climatology* 38.9, pp. 3546–3564. DOI: 10.1002/joc.5516.

Hanna, S. R. (1969). "The thickness of the planetary boundary layer." In: *Atmospheric Environment (1967)* 3.5, pp. 519–536. ISSN: 0004-6981. DOI: https://doi.org/10.1016/0004-6981(69)90042-0.

Hanssen-Bauer, I, M. K. Solås, and E. Steffensen (1990). *Climate of Spitsbergen*. DNMI.

Hanssen-Bauer, I, E. Førland, H Hisdal, S Mayer, A. Sandø, and A Sorteberg (Eds.) (2019). "Climate in Svalbard 2100 - a knowledge base for climate adaption." In: *NCCS report* M-1242. ISSN: 2387-3027.

Harms, A. A. P., V. Tverberg, and H. Svendsen (2007). "Physical Qualification and Quantification of the Water Masses in the Kongsfjorden-Krossfjorden System Cross Section." In: *OCEANS 2007 - Europe*, pp. 1–6. DOI: 10.1109/OCEANSE.2007.4302332.

Hendricks, S., S. Gerland, L. Smedsrud, C. Haas, A. Pfaffhuber, and F. Nilsen (2011). "Sea-ice thickness variability in Storfjorden, Svalbard." In: *Annals of Glaciology* 52.57, pp. 61–68. DOI: 10.3189/172756411795931561.

Hilmer, M. and T. Jung (Apr. 2000). "Evidence for a recent change in the link between the North Atlantic Oscillation and Arctic Sea ice export." In: *Geophysical Research Letters* 27.7, pp. 989–992. ISSN: 1944-8007. DOI: 10.1029/1999GL010944.

Honda, M., J. Inoue, and S. Yamane (2009). "Influence of low Arctic sea-ice minima on anomalously cold Eurasian winters." In: *Geophysical Research Letters* 36.8. DOI: 10.1029/2008GL037079.

Houghton, J. T., Y Ding, D. Griggs, M Noguer, P. Van der Linden, X Dai, K Maskell, and C. Johnson, eds. (2001). *Climate Change 2001: The*

Scientific Basis. Contribution of Working Group I to the Third Assessment Report of theIntergovernmental Panel on Climate Change. Cambridge, United Kingdom and New York, NY, USA: Cambridge University Press, 881pp.

Høyland, K. V. (2009). "Ice thickness, growth and salinity in Van Mijenfjorden, Svalbard, Norway." In: *Polar Research* 28.3, pp. 339–352. DOI: 10.1111/j.1751-8369.2009.00133.x.

Huang, J., X. Zhang, Q. Zhang, Y. Lin, M. Hao, Y. Luo, Z. Zhao, Y. Yao, X. Chen, L. Wang, et al. (2017). "Recently amplified arctic warming has contributed to a continual global warming trend." In: *Nature Climate Change* 7.12, p. 875. DOI: 10.1038/s41558-017-0009-5.

Humlum, O., J.-E. Solheim, and K. Stordahl (2011). "Spectral analysis of the Svalbard temperature record 1912–2010." In: *Advances in Meteorology* 2011.

Hyland, R. and A Wexler (1983). "Formulations for the thermodynamic properties of the saturated phases of H2O from 173.15 K to 473.15 K." In: *ASHRAE Transactions* 89.2A, pp. 500–519.

IPCC (2013). *Climate Change 2013: The Physical Science Basis. Contribution of Working Group I to the Fifth Assessment Report of the Intergovernmental Panel on Climate Change*. Ed. by T. Stocker, D. Qin, G.-K. Plattner, M. Tignor, S. Allen, J. Boschung, A. Nauels, Y. Xia, V. Bex, and P. Midgley. Cambridge, United Kingdom and New York, NY, USA: Cambridge University Press, p. 1535. ISBN: ISBN 978-1-107-66182-0. DOI: 10.1017/CBO9781107415324. URL: www.climatechange2013.org.

Intrieri, J. M., C. W. Fairall, M. D. Shupe, P. O. G. Persson, E. L. Andreas, P. S. Guest, and R. E. Moritz (2002). "An annual cycle of Arctic surface cloud forcing at SHEBA." In: *Journal of Geophysical Research: Oceans* 107.C10, SHE 13–1–SHE 13–14. DOI: 10.1029/2000JC000439.

Isaksen, K., Ø. Nordli, E. J. Førland, E. Łupikasza, S. Eastwood, and T Niedźwiedź (2016). "Recent warming on Spitsbergen – Influence of atmospheric circulation and sea ice cover." In: *Journal of Geophysical Research: Atmospheres* 121.20. DOI: 10.1002/2016JD025606.

Isaksson, E., J. Kohler, V. Pohjola, J. Moore, M. Igarashi, L. Karlöf, T. Martma, H. Meijer, H. Motoyama, R. Vaikmäe, et al. (2005). "Two ice-core δ18O records from Svalbard illustrating climate and sea-ice variability over the last 400 years." In: *The Holocene* 15.4, pp. 501–509.

Jaiser, R., K. Dethloff, D. Handorf, A. Rinke, and J. Cohen (2012). "Impact of sea ice cover changes on the Northern Hemisphere atmospheric winter circulation." In: *Tellus A: Dynamic Meteorology and Oceanography* 64.1, p. 11595. DOI: 10.3402/tellusa.v64i0.11595.

Jaiser, R., T. Nakamura, D. Handorf, K. Dethloff, J. Ukita, and K. Yamazaki (2016). "Atmospheric winter response to Arctic sea ice changes in reanalysis data and model simulations." In: *Journal of Geophysical Research: Atmospheres* 121.13, pp. 7564–7577. DOI: 10.1002/2015JD024679.

Kayser, M., M. Maturilli, R. M. Graham, S. R. Hudson, A. Rinke, L. Cohen, J.-H. Kim, S.-J. Park, W. Moon, and M. A. Granskog (2017). "Vertical thermodynamic structure of the troposphere during the Norwegian young sea ICE expedition (N-ICE2015)." In: *Journal of Geophysical Research: Atmospheres* 122.20, pp. 10855–10872. DOI: 10.1002/2016JD026089.

Kim, H.-M. and B.-M. Kim (2017). "Relative Contributions of Atmospheric Energy Transport and Sea Ice Loss to the Recent Warm Arctic Winter." In: *Journal of Climate* 30.18, pp. 7441–7450. DOI: 10.1175/JCLI-D-17-0157.1.

Kim, K.-Y., B. D. Hamlington, H. Na, and J. Kim (2016). "Mechanism of seasonal Arctic sea ice evolution and Arctic amplification." In: *The Cryosphere* 10.5, pp. 2191–2202. DOI: 10.5194/tc-10-2191-2016.

Kim, K.-Y., J.-Y. Kim, J. Kim, S. Yeo, H. Na, B. D. Hamlington, and R. R. Leben (2019). "Vertical Feedback Mechanism of Winter Arctic Amplification and Sea Ice Loss." In: *Scientific reports* 9.1, p. 1184.

Kirtman, B., S. Power, J. Adedoyin, G. Boer, R. Bojariu, I. Camilloni, F. Doblas-Reyes, A. Fiore, M. Kimoto, G. Meehl, M. Prather, A. Sarr, C. Sch ar, R. Sutton, G. van Oldenborgh, G. Vecchi, and H. Wang (2013). "Near-term Climate Change: Projections and Predictability." In: *Climate Change 2013: The Physical Science Basis. Contribution of Working Group I to the Fifth Assessment Report of the Intergovernmental Panel on Climate Change*. Ed. by T. Stocker, D. Qin, G.-K. Plattner, M. Tignor, S. Allen, J. Boschung, A. Nauels, Y. Xia, V. Bex, and P. Midgley. Cambridge, United Kingdom and New York, NY, USA: Cambridge University Press. Chap. 11, pp. 953–1028. ISBN: ISBN 978-1-107-66182-0. DOI: 10.1017/CBO9781107415324.023.

Knudsen, E. M., B. Heinold, **S. Dahlke**, H. Bozem, S. Crewell, I. V. Gorodetskaya, G. Heygster, D. Kunkel, M. Maturilli, M. Mech, C. Viceto, A. Rinke, H. Schmithüsen, A. Ehrlich, A. Macke, C. Lüpkes, and M. Wendisch (2018). "Meteorological conditions during the ACLOUD/PASCAL field campaign near Svalbard in early summer 2017." In: *Atmospheric Chemistry and Physics* 18.24, pp. 17995–18022. DOI: 10.5194/acp-18-17995-2018.

Koch, L. (1945). "The east Greenland ice, Medd." In: *Grønland 130* 130.3.

Koenigk, T., P. Berg, and R. Döscher (2015). "Arctic climate change in an ensemble of regional CORDEX simulations." In: *Polar Research* 34.1, p. 24603. DOI: 10.3402/polar.v34.24603.

Kwok, R. (2018). "Arctic sea ice thickness, volume, and multiyear ice coverage: losses and coupled variability (1958–2018)." In: *Environmental Research Letters* 13.10, p. 105005. DOI: 10.1088/1748-9326/aae3ec.

Kwok, R. and D. A. Rothrock (Mar. 1999). "Variability of Fram Strait ice flux and North Atlantic Oscillation." In: *Journal of Geophysical*

Research: Oceans 104.C3, pp. 5177–5189. ISSN: 0148-0227. DOI: 10.1029/1998JC900103.

Larsen, K. M. H., G.-P. C., P. Fratantoni, A. Beszczynska-Möller, and S. L. E. Hughes (2016). "ICES Report on Ocean Climate 2015. ICES Cooperative Research Report No. 331." In: 77pp.

Lien, V. S., P. Schlichtholz, Ø. Skagseth, and F. B. Vikebø (2017). "Wind-Driven Atlantic Water Flow as a Direct Mode for Reduced Barents Sea Ice Cover." In: *Journal of Climate* 30.2, pp. 803–812. DOI: 10.1175/JCLI-D-16-0025.1.

Lind, S. and R. B. Ingvaldsen (2012). "Variability and impacts of Atlantic Water entering the Barents Sea from the north." In: *Deep Sea Research Part I: Oceanographic Research Papers* 62, pp. 70–88. ISSN: 0967-0637. DOI: 10.1016/j.dsr.2011.12.007.

Lindsay, R., M. Wensnahan, A. Schweiger, and J. Zhang (2014). "Evaluation of Seven Different Atmospheric Reanalysis Products in the Arctic." In: *Journal of Climate* 27.7, pp. 2588–2606. DOI: 10.1175/JCLI-D-13-00014.1.

Luo, D., Y. Xiao, Y. Yao, A. Dai, I. Simmonds, and C. L. E. Franzke (2016). "Impact of Ural Blocking on Winter Warm Arctic–Cold Eurasian Anomalies. Part I: Blocking-Induced Amplification." In: *Journal of Climate* 29.11, pp. 3925–3947. DOI: 10.1175/JCLI-D-15-0611.1.

Maturilli, M. and M. Kayser (2017). "Arctic warming, moisture increase and circulation changes observed in the Ny-Ålesund homogenized radiosonde record." In: *Theoretical and Applied Climatology* 130.1, pp. 1–17. ISSN: 1434-4483. DOI: 10.1007/s00704-016-1864-0.

Maturilli, M., A. Herber, and G. König-Langlo (2015). "Surface radiation climatology for Ny-Ålesund, Svalbard (78.9 N), basic observations for trend detection." In: *Theoretical and Applied Climatology* 120.1-2, pp. 331–339. DOI: 10.1007/s00704-014-1173-4.

Mewes, D. and C. Jacobi (2019). "Heat transport pathways into the Arctic and their connections to surface air temperatures." In: *Atmospheric Chemistry and Physics* 19.6, pp. 3927–3937. DOI: 10.5194/acp-19-3927-2019.

Moore, G. W. K. (2016). "The December 2015 North Pole Warming Event and the Increasing Occurrence of Such Events." In: *Scientific Reports* 6. DOI: 10.1038/srep39084.

Muckenhuber, S., F. Nilsen, A. Korosov, and S. Sandven (2016). "Sea ice cover in Isfjorden and Hornsund, Svalbard (2000–2014) from remote sensing data." In: *The Cryosphere* 10.1, pp. 149–158. DOI: 10.5194/tc-10-149-2016.

Nilsen, F., F. Cottier, R. Skogseth, and S. Mattsson (2008). "Fjord–shelf exchanges controlled by ice and brine production: The interannual variation of Atlantic Water in Isfjorden, Svalbard." In: *Continental Shelf Research* 28.14, pp. 1838–1853. ISSN: 0278-4343. DOI: 10.1016/j.csr.2008.04.015.

Nomokonova, T., K. Ebell, U. Löhnert, M. Maturilli, C. Ritter, and E. O'Connor (2019). "Statistics on clouds and their relation to thermodynamic conditions at Ny-Ålesund using ground-based sensor synergy." In: *Atmospheric Chemistry and Physics* 19.6, pp. 4105–4126. DOI: 10.5194/acp-19-4105-2019.

Nordli, Ø., R. Przybylak, A. E. Ogilvie, and K. Isaksen (2014). "Long-term temperature trends and variability on Spitsbergen: the extended Svalbard Airport temperature series, 1898—2012." In: *Polar Research* 33.1, p. 21349. DOI: 10.3402/polar.v33.21349.

Ogi, M., S. Rysgaard, and D. G. Barber (2016). "Importance of combined winter and summer Arctic Oscillation (AO) on September sea ice extent." In: *Environmental Research Letters* 11.3, p. 034019. DOI: 10.1088/1748-9326/11/3/034019.

Onarheim, I. H., L. H. Smedsrud, R. B. Ingvaldsen, and F. Nilsen (2014). "Loss of sea ice during winter north of Svalbard." In: *Tellus A: Dynamic Meteorology and Oceanography* 66.1, p. 23933. DOI: 10.3402/tellusa.v66.23933.

Onarheim, I. H., T. Eldevik, M. Årthun, R. B. Ingvaldsen, and L. H. Smedsrud (2015). "Skillful prediction of Barents Sea ice cover." In: *Geophysical Research Letters* 42.13, pp. 5364–5371. DOI: 10.1002/2015GL064359.

Onarheim, I. H., T. Eldevik, L. H. Smedsrud, and J. C. Stroeve (2018). "Seasonal and regional manifestation of Arctic sea ice loss." In: *Journal of Climate* 2018.

Osuch, M. and T. Wawrzyniak (2016). "Climate projections in the Hornsund area, Southern Spitsbergen." In: *Polish Polar Research* 37.3, pp. 379–402. DOI: 10.1515/popore-2016-0020.

Overland, J. E., J. A. Francis, E. Hanna, and M. Wang (2012). "The recent shift in early summer Arctic atmospheric circulation." In: *Geophysical Research Letters* 39.19. DOI: 10.1029/2012GL053268.

Overland, J. E., K. Dethloff, J. A. Francis, R. J. Hall, E. Hanna, S.-J. Kim, J. A. Screen, and T. Shepherd Theodore G.and Vihma (2016). "Nonlinear response of mid-latitude weather to the changing Arctic." In: *Nature Climate Change* 6, pp. 992 –999. DOI: 10.1038/nclimate3121.

Pavlov, A. K., V. Tverberg, B. V. Ivanov, F. Nilsen, S. Falk-Petersen, and M. A. Granskog (2013). "Warming of Atlantic Water in two west Spitsbergen fjords over the last century (1912–2009)." In: *Polar Research* 32.1, p. 11206. DOI: 10.3402/polar.v32i0.11206.

Pithan, F. and T. Mauritsen (2014). "Arctic amplification dominated by temperature feedbacks in contemporary climate models." In: *Nature Geoscience* 7.3, p. 181. DOI: 10.1038/ngeo2071.

Pithan, F., G. Svensson, R. Caballero, D. Chechin, T. W. Cronin, A. M. Ekman, R. Neggers, M. D. Shupe, A. Solomon, M. Tjernström, and M. Wendisch (2018). "Role of air-mass transformations in exchange between the Arctic and mid-latitudes." In: *Nature Geoscience* 11.11, pp. 805–812. DOI: 10.1038/s41561-018-0234-1.

Przybylak, R., A. Araźny, Ø. Nordli, R. Finkelnburg, M. Kejna, T. Budzik, K. Migała, S. Sikora, D. Puczko, K. Rymer, and G. Rachlewicz (2014). "Spatial distribution of air temperature on Svalbard during 1 year with campaign measurements." In: *International Journal of Climatology* 34.14, pp. 3702–3719. DOI: 10.1002/joc.3937.

Rayner, N. A., D. E. Parker, E. B. Horton, C. K. Folland, L. V. Alexander, D. P. Rowell, E. C. Kent, and A. Kaplan (2003). "Global analyses of sea surface temperature, sea ice, and night marine air temperature since the late nineteenth century." In: *Journal of Geophysical Research: Atmospheres* 108.D14. DOI: 10.1029/2002JD002670.

Rinke, A., M. Maturilli, R. M. Graham, H. Matthes, D. Handorf, L. Cohen, S. R. Hudson, and J. C. Moore (2017). "Extreme cyclone events in the Arctic: Wintertime variability and trends." In: *Environmental Research Letters* 12.9, p. 094006. DOI: 10.1088/1748-9326/aa7def.

Rinke, A, E Knudsen, D Mewes, W Dorn, D Handorf, K Dethloff, and J. Moore (2019). "Arctic summer sea-ice melt and related atmospheric conditions in coupled regional climate model simulations and observations." In: *Journal of Geophysical Research: Atmospheres*. DOI: 10.1029/2018JD030207.

Sandø, A. B., Y. Gao, and H. R. Langehaug (2014). "Poleward ocean heat transports, sea ice processes, and Arctic sea ice variability in NorESM1-M simulations." In: *Journal of Geophysical Research: Oceans* 119.3, pp. 2095–2108. DOI: 10.1002/2013JC009435.

Schellnhuber, H. J., S. Rahmstorf, and R. Winkelmann (2016). "Why the right climate target was agreed in Paris." In: *Nature Climate Change* 6.7, p. 649. DOI: 10.1038/nclimate3013.

Scheuchl, B., D. Flett, R. Caves, and I. Cumming (2004). "Potential of RADARSAT-2 data for operational sea ice monitoring." In: *Canadian Journal of Remote Sensing* 30.3, pp. 448–461. DOI: 10.5589/m04-011.

Screen, J. A. and I. Simmonds (2010). "The central role of diminishing sea ice in recent Arctic temperature amplification." In: *Nature* 464.7293, p. 1334. DOI: 10.1038/nature09051.

Sen, P. K. (1968). "Estimates of the regression coefficient based on Kendall's tau." In: *Journal of the American statistical association* 63.324, pp. 1379–1389.

Serreze, M. C. and A. P. Barrett (2008). "The Summer Cyclone Maximum over the Central Arctic Ocean." In: *Journal of Climate* 21.5, pp. 1048–1065. DOI: 10.1175/2007JCLI1810.1.

Serreze, M. C. and R. G. Barry (2011). "Processes and impacts of Arctic amplification: A research synthesis." In: *Global and Planetary Change* 77.1, pp. 85 –96. ISSN: 0921-8181. DOI: 10.1016/j.gloplacha.2011.03.004.

Serreze, M. C., A. Barrett, J. Stroeve, D N. Kindig, and M M. Holland (2009). "The emergence of surface-based Arctic amplification." In: *The Cryosphere* 3, pp. 11–19. DOI: 10.5194/tc-3-11-2009.

Serreze, M. C., A. P. Barrett, and J. J. Cassano (2011). "Circulation and surface controls on the lower tropospheric air temperature field of the Arctic." In: *Journal of Geophysical Research: Atmospheres* 116.D7. DOI: 10.1029/2010JD015127.

Shepherd, T. G. (2016). "Effects of a warming Arctic." In: *Science* 353.6303, pp. 989–990. DOI: 10.1126/science.aag2349.

Shupe, M. D. and J. M. Intrieri (2004). "Cloud Radiative Forcing of the Arctic Surface: The Influence of Cloud Properties, Surface Albedo, and Solar Zenith Angle." In: *Journal of Climate* 17.3, pp. 616–628. DOI: 10.1175/1520-0442(2004)017<0616:CRFOTA>2.0.CO;2.

Skeie, P. (2000). "Meridional flow variability over the Nordic Seas in the Arctic oscillation framework." In: *Geophysical Research Letters* 27.16, pp. 2569–2572. DOI: 10.1029/2000GL011529.

Skogseth, R., P. M. Haugan, and J. Haarpaintner (2004). "Ice and brine production in Storfjorden from four winters of satellite and in situ observations and modeling." In: *Journal of Geophysical Research: Oceans* 109.C10. DOI: 10.1029/2004JC002384.

Smedsrud, L. H., M. H. Halvorsen, J. C. Stroeve, R. Zhang, and K. Kloster (2017). "Fram Strait sea ice export variability and September Arctic sea ice extent over the last 80 years." In: *The Cryosphere* 11.1, pp. 65–79. DOI: 10.5194/tc-11-65-2017.

Smedsrud, L. H., I. Esau, R. B. Ingvaldsen, T. Eldevik, P. M. Haugan, C. Li, V. S. Lien, A. Olsen, A. M. Omar, O. H. Otterå, B. Risebrobakken, A. B. Sandø, V. A. Semenov, and S. A. Sorokina (2013). "The role of the Barents Sea in the Arctic climate system." In: *Reviews of Geophysics* 51.3, pp. 415–449. DOI: 10.1002/rog.20017.

Sorokina, S. A., C. Li, J. J. Wettstein, and N. G. Kvamstø (2016). "Observed Atmospheric Coupling between Barents Sea Ice and the Warm-Arctic Cold-Siberian Anomaly Pattern." In: *Journal of Climate* 29.2, pp. 495–511. DOI: 10.1175/JCLI-D-15-0046.1.

Steffen, W., J. Rockström, K. Richardson, T. M. Lenton, C. Folke, D. Liverman, C. P. Summerhayes, A. D. Barnosky, S. E. Cornell, M. Crucifix, J. F. Donges, I. Fetzer, S. J. Lade, M. Scheffer, R. Winkelmann, and H. J. Schellnhuber (2018). "Trajectories of the Earth System in the Anthropocene." In: *Proceedings of the National Academy of Sciences* 115.33, pp. 8252–8259. ISSN: 0027-8424. DOI: 10.1073/pnas.1810141115.

Steig, E. J., D. P. Schneider, S. D. Rutherford, M. E. Mann, J. C. Comiso, and D. T. Shindell (2009). " Warming of the Antarctic ice-sheet surface since the 1957 International Geophysical Year." In: *Nature–Corrigendum* 460, p. 766. DOI: 10.1038/nature08286.

Stohl, A. and P. Seibert (1998). "Accuracy of trajectories as determined from the conservation of meteorological tracers." In: *Quarterly Journal of the Royal Meteorological Society* 124.549, pp. 1465–1484. DOI: 10.1002/qj.49712454907.

Stohl, A, L Haimberger, M. P. Scheele, and H Wernli (2001). "An intercomparison of results from three trajectory models." In: *Meteorological Applications* 8.2, pp. 127–135. DOI: 10.1017/S1350482701002018.

Stohl, A. (1998). "Computation, accuracy and applications of trajectories—A review and bibliography." In: *Atmospheric Environment* 32.6, pp. 947 –966. ISSN: 1352-2310. DOI: 10.1016/S1352-2310(97)00457-3.

Stohl, A., G. Wotawa, P. Seibert, and H. Kromp-Kolb (1995). "Interpolation Errors in Wind Fields as a Function of Spatial and Temporal Resolution and Their Impact on Different Types of Kinematic Trajectories." In: *Journal of Applied Meteorology* 34.10, pp. 2149–2165. DOI: 10.1175/1520-0450(1995)034<2149:IEIWFA>2.0.CO;2.

Stramler, K., A. D. Del Genio, and W. B. Rossow (2011). "Synoptically Driven Arctic Winter States." In: *Journal of Climate* 24.6, pp. 1747–1762. DOI: 10.1175/2010JCLI3817.1.

Stroeve, J. C., V. Kattsov, A. Barrett, M. Serreze, T. Pavlova, M. Holland, and W. N. Meier (2012a). "Trends in Arctic sea ice extent from CMIP5, CMIP3 and observations." In: *Geophysical Research Letters* 39.16. DOI: 10.1029/2012GL052676.

Stroeve, J., M. Holland, W. Meier, T. Scambos, and M. Serreze (2007). "Arctic sea ice decline: Faster than forecast." In: *Geophysical Research Letters* 34.9. DOI: 10.1029/2007GL029703.

Stroeve, J., M. Serreze, M. Holland, J. Kay, J. Malanik, and A. Barrett (2012b). "The Arctic's rapidly shrinking sea ice cover: a research synthesis." In: *Climatic Change* 110.3-4, pp. 1005–1027. DOI: 10.1007/s10584-011-0101-1.

Stuecker, M. F., C. M. Bitz, K. C. Armour, C. Proistosescu, S. M. Kang, S.-P. Xie, D. Kim, S. McGregor, W. Zhang, S. Zhao, W. Cai, and F.-F. Jin (2018). "Polar amplification dominated by local forcing and feedbacks." In: *Nature Climate Change* 8.12, p. 1076. DOI: 10.1038/s41558-018-0339-y.

Stull, R. B. (2012). *An introduction to boundary layer meteorology*. Vol. 13. Springer Science & Business Media.

Sundfjord, A, J Albretsen, Y Kasajima, R Skogseth, J Kohler, C Nuth, J Skarðhamar, F Cottier, F Nilsen, L Asplin, et al. (2017). "Effects of glacier runoff and wind on surface layer dynamics and Atlantic Water exchange in Kongsfjorden, Svalbard; a model study." In: *Estuarine, Coastal and Shelf Science* 187, pp. 260–272. DOI: 10.1016/j.ecss.2017.01.015.

Taylor, P. C. (2018). "Local processes with a global reach." In: *Nature Climate Change* 8.12, p. 1035. DOI: 10.1038/s41558-018-0342-3.

Taylor, P. C., B. M. Hegyi, R. C. Boeke, and L. N. Boisvert (2018). "On the Increasing Importance of Air-Sea Exchanges in a Thawing Arctic: A Review." In: *Atmosphere* 9.2. ISSN: 2073-4433.

Theil, H (1950). "A rank-invariant method of linear and polynominal regression analysis (Parts 1-3)." In: *Ned. Akad. Wetensch. Proc. Ser. A*. Vol. 53, pp. 1397–1412.

Tislenko, D. and B. Ivanov (2015). "Long-term variability of Atlantic water temperature in the Svalbard fjords in conditions of past and recent global warming." English. In: *Czech Polar Reports* 2, pp. 134–142. ISSN: 1805-0689. DOI: 10.5817/CPR2015-2-12.

Torres, R. et al. (2012). "GMES Sentinel-1 mission." In: *Remote Sensing of Environment* 120. The Sentinel Missions - New Opportunities for Science, pp. 9–24. ISSN: 0034-4257. DOI: 10.1016/j.rse.2011.05.028.

Trenberth, K. E. and J. M. Caron (2001). "Estimates of Meridional Atmosphere and Ocean Heat Transports." In: *Journal of Climate* 14.16, pp. 3433–3443. DOI: 10.1175/1520-0442(2001)014<3433:EOMAAO>2.0.CO;2.

Verlinde, J. et al. (2007). "The Mixed-Phase Arctic Cloud Experiment." In: *Bulletin of the American Meteorological Society* 88.2, pp. 205–222. DOI: 10.1175/BAMS-88-2-205.

Vinje, T. (2001). "Anomalies and Trends of Sea-Ice Extent and Atmospheric Circulation in the Nordic Seas during the Period 1864–1998." In: *Journal of Climate* 14.3, pp. 255–267. DOI: 10.1175/1520-0442(2001)014<0255:AATOSI>2.0.CO;2.

Vinje, T., N. Nordlund, and Å. Kvambekk (1998). "Monitoring ice thickness in Fram Strait." In: *Journal of Geophysical Research: Oceans* 103.C5, pp. 10437–10449. DOI: 10.1029/97JC03360.

Walczowski, W. and J. Piechura (2007). "Pathways of the Greenland Sea warming." In: *Geophysical Research Letters* 34.10. DOI: 10.1029/2007GL029974.

– (2011). "Influence of the West Spitsbergen Current on the local climate." In: *International Journal of Climatology* 31.7, pp. 1088–1093. DOI: 10.1002/joc.2338.

Wang, C., B. Cheng, K. Wang, S. Gerland, and O. Pavlova (2015). "Modelling snow ice and superimposed ice on landfast sea ice in Kongsfjorden, Svalbard." In: *Polar Research* 34.1, p. 20828. DOI: 10.3402/polar.v34.20828.

Wendisch, M., M. Brückner, J. Burrows, S Crewell, K. Dethloff, K Ebell, C. Lüpkes, A. Macke, J. Notholt, J Quaas, et al. (2017). "Understanding causes and effects of rapid warming in the Arctic." In: *Eos* 98. DOI: 10.1029/2017EO064803.

Wendisch, M., A. Macke, A. Ehrlich, C. Lüpkes, M. Mech, D. Chechin, K. Dethloff, C. Barientos, H. Bozem, M. Brückner, et al. (2018). "The Arctic Cloud Puzzle: Using ACLOUD/PASCAL Multi-Platform Observations to Unravel the Role of Clouds and Aerosol Particles in Arctic Amplification." In: *Bulletin of the American Meteorological Society* 100.5, pp. 841–871. DOI: 10.1175/BAMS-D-18-0072.1.

Woods, C. and R. Caballero (2016). "The role of moist intrusions in winter Arctic warming and sea ice decline." In: *Journal of Climate* 29.12, pp. 4473–4485. DOI: 10.1175/JCLI-D-15-0773.1.

Woods, C., R. Caballero, and G. Svensson (2013). "Large-scale circulation associated with moisture intrusions into the Arctic during winter." In: *Geophysical Research Letters* 40.17, pp. 4717–4721. DOI: 10.1002/grl.50912.

Wu, B., J. Wang, and J. E. Walsh (2006). "Dipole Anomaly in the Winter Arctic Atmosphere and Its Association with Sea Ice Motion." In: *Journal of Climate* 19.2, pp. 210–225. DOI: 10.1175/JCLI3619.1.

Yang, X.-Y., J. C. Fyfe, and G. M. Flato (2010). "The role of poleward energy transport in Arctic temperature evolution." In: *Geophysical Research Letters* 37.14. DOI: 10.1029/2010GL043934.

Yeo, H., S.-J. Park, B.-M. Kim, M. Shiobara, S.-W. Kim, H. Kwon, J.-H. Kim, J.-H. Jeong, S. S. Park, and T. Choi (2018). "The observed relationship of cloud to surface longwave radiation and air temperature at Ny-Ålesund, Svalbard." In: *Tellus B: Chemical and Physical Meteorology* 70.1, pp. 1–10. DOI: 10.1080/16000889.2018.1450589.

Yue, S., P. Pilon, B. Phinney, and G. Cavadias (2002). "The influence of autocorrelation on the ability to detect trend in hydrological series." In: *Hydrological processes* 16.9, pp. 1807–1829. DOI: 10.1002/hyp.1095.

Zhang, Y., Z. Gao, D. Li, Y. Li, N. Zhang, X. Zhao, and J. Chen (2014). "On the computation of planetary boundary-layer height using the bulk Richardson number method." In: *Geoscientific Model Development* 7.6, pp. 2599–2611. DOI: 10.5194/gmd-7-2599-2014.

Zhuravskiy, D., B. Ivanov, and A. Pavlov (2012). "Ice conditions at Gronfjorden Bay, Svalbard, from 1974 to 2008." In: *Polar Geography* 35.2, pp. 169–176. DOI: 10.1080/1088937X.2012.662535.

von Storch, H. and F. Zwiers (2001). *Statistical Analysis in Climate Research*. Cambridge University Press. ISBN: 9780521012300.

ACKNOWLEDGMENTS

I wish to express my gratitude to everyone who has contributet to this thesis. Most importantly, thanks to Prof. Dr. Klaus Dethloff and Dr. Marion Maturilli for offering me the opportunity to work on this interesting topic, and for their continuous, dedicated supervision and help. Thanks to all my colleagues from the Atmo section for their kind welcome, and for all the small and big advices and situations in the everyday work that let the three years pass so fast. I am grateful to have been offered the opportunity to conduct field work in Ny-Ålesund and experience this unique place, with its unique people. I wish to thank my reviewers, Prof. Dr. Klaus Dethloff, Prof. Dr. Manfred Wendisch and Dr. habil. Tymon Zieliński for taking the time to examine this manuscript, and additionally Prof. Dr. Manfred Wendisch for supervising this work. A special thank goes to Dr. Nicholas Hughes and Dr. Penelope Wagner for providing the sea ice data set, and for valuable discussions. I am thankful to Dr. Sebastian Gerland, Dr. Stephen Hudson, Dr. Lana Cohen, Dr. Robert Graham for the fruitful discussions in Tromsø, which greatly improved the shape of this study. Thank goes to Dr. Henrik Gruythe for assisting with the FLEXTRA trajectories. Last but not least, thank goes to my parents and friends, who always supported my efforts and were there for me when I needed them.

I gratefully acknowledge the funding by the Deutsche Forschungsgemeinschaft (DFG, German Research Foundation)– Projektnummer 268020496 – TRR 172, within the Transregional Collaborative Research Center "ArctiC Amplification: Climate Relevant Atmospheric and SurfaCe Processes, and Feedback Mechanisms (AC)^3"

DECLARATION

I hereby declare that I have conducted and written this thesis on my own, without contributions from other parties and with no other material than referenced. Graphics, quotes or ideas from other resources, that are directly or indirectly included in this thesis, are unequivocally referenced to the original work. I moreover declare that this thesis has never been submitted for examination in this or in any other form.

Potsdam, July 2019

Sandro Dahlke